



UNIVERSITÁ DEGLI STUDI DI MILANO &  
UNIVERSITÁ CATTOLICA DEL SACRO CUORE

DIPARTIMENTO DI MATEMATICA E FISICA

CORSO DI DOTTORATO DI RICERCA IN  
FISICA, ASTROFISICA E FISICA APPLICATA

Ciclo XXVII

**Exploring detection limits and response time  
scales of chemiresistor gas sensors based on  
carbon nanotube and hybrid layers.**

Settore scientifico disciplinare FIS/03

**Tesi di Dottorato di:**  
Federica Rigoni

**Coordinatore:** Prof. Marco Bersanelli

**Tutore:** Prof. Luigi Sangaletti

Anno Accademico 2013-2014

To my family and my friends

*“And today we begin to deal with those things that are present in greatest quantities on earth and that everyday surround us: the gases.”*

*(M. Sancrotti’s class)*



# Contents

<b>Introduction</b>	<b>7</b>
<b>1 Properties of carbon nanotubes and gas sensing application</b>	<b>11</b>
1.1 Structural and electronic properties . . . . .	12
1.1.1 Interaction with gases . . . . .	19
1.2 Synthesis of carbon nanotubes . . . . .	23
1.3 Gas sensors based on SWCNTs . . . . .	25
<b>2 Experimental techniques</b>	<b>29</b>
2.1 Gas sensing measurements . . . . .	29
2.1.1 General samples preparation . . . . .	29
2.1.2 Data acquisition and gas sensing set-up . . . . .	30
2.2 Characterization techniques . . . . .	37
<b>3 Enhancing the response to ammonia gas</b>	<b>41</b>
3.1 Sample preparation and characterization . . . . .	42
3.1.1 Drop-casting and sonication vs dielectrophoresis method . . . . .	42
3.1.2 Layer characterization . . . . .	42
3.1.3 Sonication effects . . . . .	44
3.2 Results and discussion . . . . .	47
3.2.1 Response enhancement . . . . .	47
3.2.2 Detection Limit (DL) . . . . .	52
3.2.3 Response time scales . . . . .	58
3.2.4 Convolution and signal shaping . . . . .	60

3.3	Conclusions . . . . .	63
<b>4</b>	<b>Effects of the functionalization with metal oxide nanoparticles</b>	<b>65</b>
4.1	SWCNT and hybrid layers on plastic substrates . . . . .	66
4.1.1	Sample preparation and functionalization . . . . .	66
4.1.2	Layer characterization . . . . .	67
4.2	Modeling of sensing: space-charge layers at nano-scale semiconductor interfaces . . . . .	73
4.2.1	Classification of space-charge layers for n-type and p-type semiconductors . . . . .	73
4.2.2	Nano-heterojunction . . . . .	77
4.3	Results and discussion . . . . .	78
4.3.1	Response to ammonia in air and in gas testing chamber . . . . .	78
4.3.2	Response to humidity . . . . .	86
4.3.3	Response to nitrogen dioxide . . . . .	87
4.3.4	Sensing mechanism . . . . .	91
4.4	Conclusions . . . . .	98
<b>5</b>	<b>Hybrid nanoarchitectures</b>	<b>99</b>
5.1	C nanostructured on aligned ZnO nanorods . . . . .	99
5.1.1	Catalyst-free CVD . . . . .	100
5.1.2	Fe catalyst-assisted CVD . . . . .	105
5.1.3	Gas sensitivity . . . . .	108
5.2	Tubular Sn-filled carbon nanostructures on ITO . . . . .	112
5.2.1	Sample preparation and characterization . . . . .	112
5.2.2	Gas sensitivity and response time . . . . .	114
5.2.3	Response curve and Detection Limit . . . . .	118
5.3	Conclusions . . . . .	119
	<b>Appendices</b>	<b>121</b>
	<b>A SWCNT-based NH<sub>3</sub> sensor in chemFET configuration</b>	<b>123</b>
	<b>B Adsorption isotherms</b>	<b>127</b>
	<b>C Conversion of R.H. into ppm of water</b>	<b>131</b>

**CONTENTS** **5**

---

<b>Bibliography</b>	<b>132</b>
<b>List of publications &amp; presentations</b>	<b>145</b>
<b>Acknowledgements</b>	<b>149</b>
<b>Curriculum Vitae</b>	<b>151</b>



# Introduction

Crucial features in gas sensors for environmental monitoring are the gas sensitivity in the low ppb (parts per billion) range and the ability to discriminate variations of a certain polluting gas from other interfering gases. Monitoring of ammonia concentrations is mandatory to reduce the hazard for human health and vegetation determined by the widespread use of ammonia and its derivatives as agricultural nitrogen fertilizers, which is known to cause severe environmental problems [1–4]. In particular, a growing body of investigations [5–8] is highlighting the relevant role played by ammonia as a precursor of secondary fine particulate (PM10 and PM2.5), which represents a serious threat to human health. Ammonia, besides being a toxic molecule, could hence be used as a local marker of secondary fine particulate formation, allowing indirect control of particulate emission sources. In spite of this urgency, the detection of ammonia concentrations in urban areas with chemiresistor gas sensors (CGSs) has been so far widely overlooked, since the average levels are usually low, i.e. in the 20-30 ppb range (as shown in Fig. 1 and recently discussed by Chiesa *et al.* [9]) while the CGSs are usually tested by exposure to ammonia in the ppm (parts per million) range.

In the last two decades several scientists proposed a new carbon based technology, against the usual silicon based one, and the allotropes of carbon, i.e. carbon nanotubes, single atomic layers of graphite (graphene), fullerene molecules and diamond, as new electronic materials with unique properties.

Carbon nanotubes (CNTs), since their discovery attributed to Iijima [10] more than 20 years ago, are well known and studied systems for many applications by now. Of course, gas sensing is one of these applications. With respect to commercial electrochemical sensors for environmental monitoring (mostly based

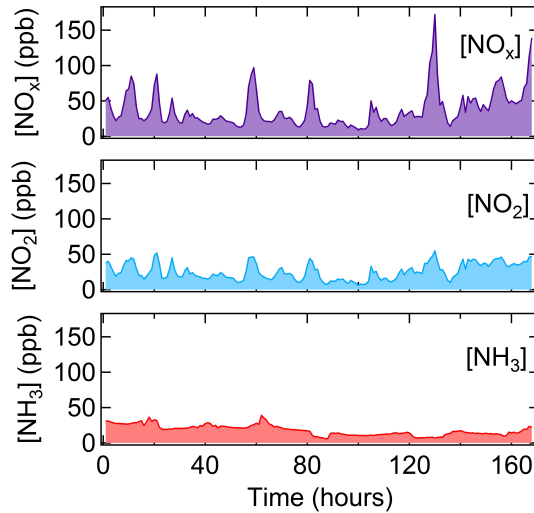


**Figure 1:** Polluting gases ( $\text{NO}_x$ ,  $\text{NO}_2$  and  $\text{NH}_3$ ) concentrations over one week in an urban area (City of Milan, during March 2008). Data source: ARPA LOMBARDIA (monitoring station of Via Pascal, Milan). Public data (with the exception of  $[\text{NH}_3]$ ) available on the website: [www.arpalombardia.it](http://www.arpalombardia.it). Figure adapted from [9].

on metal oxide materials), CNTs show a higher physical and chemical stability, better transport of charge to the electrodes and a wide range of possible architectures and operational features, among which the operation at room temperature, that make them unique materials for gas detection. So far, many CNT-based architectures have been proposed [11, 11, 12, 12–23], following a systematic investigation in testing chambers. However, little attention has been paid to the capability of these sensors to measure sub-ppm  $[\text{NH}_3]$  in air. Although sensitivity in the ppt (parts per trillion) range of pristine CNTs to ammonia has been demonstrated in inert Ar atmosphere under UV irradiation [24], the use of inert gas represents a limitation for realistic  $[\text{NH}_3]$  environmental monitoring, where chemiresistor gas sensors (CGSs) should provide a sensitivity at the ppb level under real atmospheric conditions. To overcome this limitation, most of the study of this thesis have been carried out in the lab environment, which is much closer to the final destination of the CNTs sensors. The control over selectivity

and interfering gases effects is also mandatory in gas detection. Among interfering gases,  $\text{NO}_2$  and  $\text{H}_2\text{O}$  are the most important when monitoring  $[\text{NH}_3]$  in the environment. In particular, the presence of high concentrations of humidity may dramatically alter the working conditions of gas sensors.

The main goal of this thesis is to increase the sensitivity to  $[\text{NH}_3]$  and to improve the detection limit (DL), exploring sample preparation strategies of low-cost single walled carbon nanotubes (SWCNT)-based gas sensors operating at room temperature, considering also the response to other interfering gases. The search for a sensitivity improvement also allowed us to explore the time-scale of the sensors response and recovery. This, in turn, revealed the capability of our SWCNT-based devices to track quick signal fluctuations otherwise missed by commercially available gas sensors based on metal oxides. Furthermore, effects of metal oxide nanoparticles functionalization and gas response of hybrid layers have been also investigated. The choice of SWCNTs rather than multi-walled carbon nanotubes (MWCNTs) is motivated by the need to reduce the complexity of gas-nanostructure interactions as much as possible, and focus only on the device sensitivity, avoiding multiple wall effects in the interaction of polluting gas with CNTs.

The outline of the thesis is as follow:

- in chapter 1 an overview of the physical properties of SWCNTs and their application as gas sensors is reported;
- in chapter 2 a brief description of the experimental techniques employed to the electrical measurements, the general sample preparation and characterization, is given;
- strategies explored to enhance ammonia sensitivity and response time-scales analysis of SWCNT-based gas sensors on ceramic ( $\text{Al}_2\text{O}_3$ ) substrates are described in chapter 3;
- in chapter 4 the effects of functionalization with metal oxide nanoparticles of SWCNT layers, deposited on plastic substrates, on the selective response to other gases, i.e.  $\text{NO}_2$  and water vapor, are discussed;
- finally, in chapter 5 we report the gas sensing response of hybrid material of nanostructured carbon grown on ZnO nanorods or ITO substrates.





# Chapter 1

## Properties of carbon nanotubes and gas sensing application

The discovery of carbon nanotubes (CNTs) is often attributed to S. Iijima who started to work on the growth mechanism of buckyballs  $C_{60}$  using arc-discharge method and accidentally noticed *helical microtubules of graphitic carbon* in High-resolution TEM (Transmission Electron Microscopy) images, reported in the famous letter in *Nature* of 1991 [10]. Actually, the first images of multi-wall carbon nanotubes was recorded in 1952 by L.V. Radushkevich and V.M. Lukyanovich, while in 1976 that of a single-wall carbon nanotube by M. Endo and coworkers [25, 26]. However, the exceptional electronic properties of CNT were not known yet, so that these hollow carbon cylinders are left in half-light. The *rediscovery* by Iijima and the theoretical studies by the late 1980s of several condensed-matter groups reporting the fascinating electronic properties, especially for the single-wall CNTs, give rise to a rebirth in carbon science and technology. In this chapter, an overview of the characteristic structural and electronic properties of CNTs is given, also considering interaction with gases, then the typical methods of synthesis are summarized and gas sensing application is presented.

## 1.1 Structural and electronic properties

Carbon nanotubes are composed by single or multiple graphene sheets rolled-up to form hollow cylinders, consequently they are called single-wall carbon nanotubes (SWCNTs) or multi-wall carbon nanotubes (MWCNTs). SWCNTs, main object of this thesis, have mean diameter of 1-3 nm and length of the order of  $\mu\text{m}$ . MWCNTs have a similar length, but larger diameter, of the order of hundreds nm. Thanks to this characteristic dimensions, carbon nanotubes are considered quasi-1D crystals. As in graphene sheet, the C atoms are in  $\text{sp}^2$  hybridization, with bond length of  $1.34 \text{ \AA}$  and bond angle of  $120^\circ$ , arranged in an hexagonal structure. Fig. 1.1 shows the graphene honey-comb lattice, with the base vectors  $\mathbf{a}_1$  and  $\mathbf{a}_2$  that form an angle of  $60^\circ$  and have module  $a_1 = a_2 = a_0 = 2.461 \text{ \AA}$ . The graphene sheet is rolled-up to form the CNT so that the *chiral vector*  $\mathbf{c} = n_1\mathbf{a}_1 + n_2\mathbf{a}_2$  is the circumference of the tube. The pair of integers  $(n_1, n_2)$ , called chiral indexes, uniquely defines a certain tube. Many properties, as band structure of carbon nanotubes, depend on the chirality. The direction of the chiral vector is given by the *chiral angle*  $\theta$  between  $\mathbf{a}_1$  and  $\mathbf{c}$

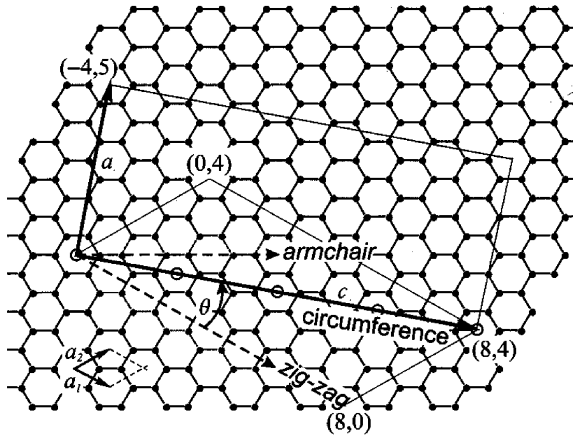


**Figure 1.1:** Honey-comb lattice of graphene with lattice the vectors  $\mathbf{a}_1$  and  $\mathbf{a}_2$  and the chiral vector  $\mathbf{c} = 8 \mathbf{a}_1 + 4\mathbf{a}_2$  of the corresponding nanotube (8, 4). The translational period  $\mathbf{a}$  and  $\mathbf{c}$  form a rectangle which is the unit cell of the tube. The chiral vector for the armchair and zig-zag tubes are also shown. [27].

Nanotubes with  $(n, 0)$  and  $\theta = 0^\circ$  are called *zig-zag tubes*, while the tubes with  $(n, n)$  and  $\theta = 30^\circ$  are called *armchair tubes*, according to how the C atoms are arranged on the circumference. In general, if  $n_1 \neq n_2$  the nanotube present chiral properties, while zig-zag and armchair are achiral.

The graphene lattice geometry and the chiral vector determine many parameters such as the diameter, the unit cell, the numbers of carbon atoms and the shape and dimension of the Brillouin zone [27]. The diameter is related to the length of the chiral vector  $\mathbf{c}$  by the formula:

$$d = \frac{c}{\pi} = \frac{a_0}{\pi} \sqrt{N}, \quad (1.1)$$

where  $N = n_1^2 + n_1 n_2 + n_2^2$ . The smallest lattice vector  $\mathbf{a}$  perpendicular to  $\mathbf{c}$  defines the translational period  $a$  along the tube axis and, with the diameter  $d$ , it defines the unit cell of the nanotube (the cylindrical surface of height  $a$  and circumference  $c$ ) which strongly depends on the chirality (Fig. 1.2). The

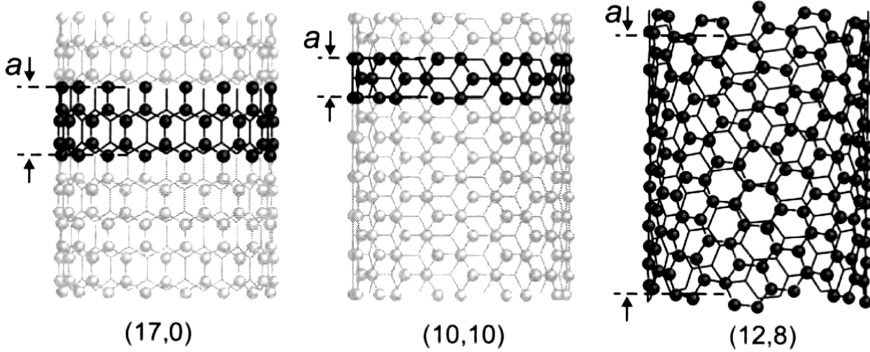


**Figure 1.2:** Structure of zig-zag  $(17, 0)$ , armchair  $(10, 10)$  and chiral  $(12, 8)$  carbon nanotubes. The unit cell has been highlighted [27].

number of C atoms  $n_C$  in the unit cell can be calculated from the area of the cylindrical surface of the tube  $S_t = a \cdot c$  and the area of the hexagonal cell of graphene  $S_g$ . If  $q$  is the number of hexagons lying on the unit cell, given by the ratio  $q = S_t/S_g$ , the number of C atoms is

$$n_c = 2q = \frac{4(n_1^2 + n_1 n_2 + n_2^2)}{nR} \quad (1.2)$$

because there are 2 atoms in the hexagonal unit cell. The very interesting physical and chemical properties of CNTs are mainly due to their structure, e.g. from a mechanical point of view, the C-C bond gives stiffness and strength to CNTs, while in terms of electronic properties, CNTs can be both metals and semiconductors, based on the diameter of the tube and the chirality [27,28]. The structural parameters are summarized in Table 1.1. Starting from the chiral in-

type	tube	diameter d	chiral angle $\Theta$
A	(n, n)	$\sqrt{3} n a_0 / \pi$	$30^\circ$
Z	(n, 0)	$n a_0 / \pi$	$0^\circ$
C	( $n_1, n_2$ )	$\sqrt{n_1^2 + n_1 n_2 + n_2^2} a_0 / \pi$	$\arccos \frac{n_1 + n_2 / 2}{\sqrt{n_1^2 + n_1 n_2 + n_2^2}}$

**Table 1.1:** Some structure parameters of (A) armchair, (Z) zig-zag and (C) chiral carbon nanotubes [27].

dexes pair ( $n_1, n_2$ ), a simple rule in order to determine the character (metallic or semiconducting) of CNTs has been shown by Hamada *et al.* [29] and Saito *et al.* [30]. It says that if  $n_1 - n_2 = 3m$  (where m is an integer or zero) the tube is metallic, otherwise it is semiconducting.

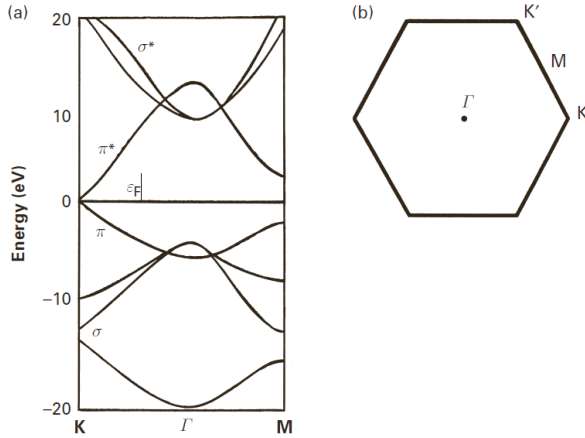


**Figure 1.3:** (a) Band structure (the Fermi energy is placed at 0 eV) and (b) sketch of the Brillouin zone for graphene [28].

Regarding the electronic properties of carbon nanotubes, we can start considering the graphene electronic properties, e.g. the band structure reported in Fig. 1.3. In first approximation, C atoms of CNTs have the same chemical bonds that exist among the graphene atoms. Along the cylinder wall the  $\sigma$   $sp^2$  bonds form the hexagonal network while  $\pi$  bonds, from  $p_z$  carbon orbital, point perpendicular to the nanotube surface. Of course, the curvature of the tube has to be taken into account in order to calculate the electronic band structure of CNTs. A lot of works in literature can be found on the calculation of the band structure of SWCNTs, mainly starting from ab-initio calculation and density functional theory (DFT), e.g. Ref. [31]. Once the band structure of the

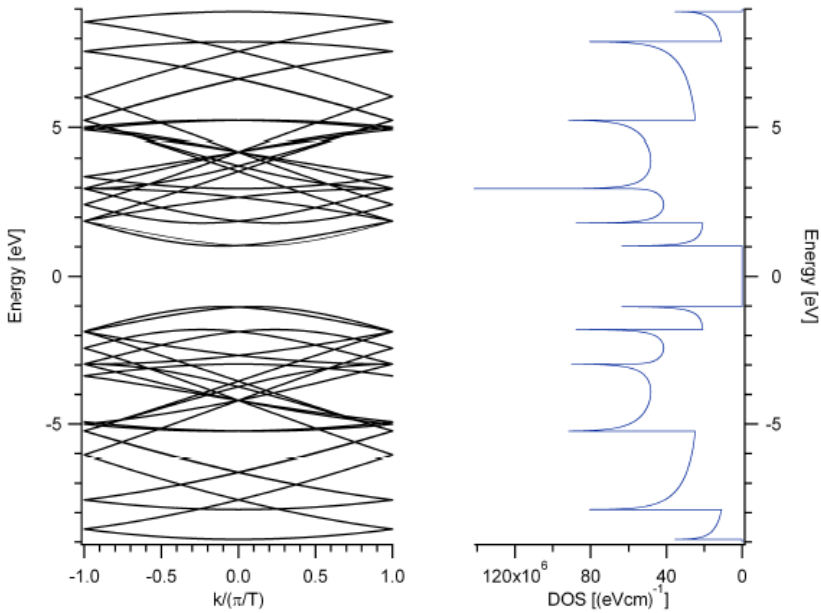


**Figure 1.4:** Example of band structure and corresponding density of states for a carbon nanotube (4, 2) [32].

SWCNT is known, the electronic density of states (DOS) for  $i$  one dimensional

electronic bands of the nanotube is given by

$$DOS = \frac{2}{q|k_z|} \sum_i \int \delta(k_z - k_i) \left| \frac{\partial E_i(k_\perp, k_z)}{\partial k_z} \right|^{-1} dk_z \quad (1.3)$$

where  $k_i$  are the roots of equation  $E - E_i(k_\perp, k_z) = 0$  and  $q|k_z|$  is the length of the 1D Brillouin zone. The quantity  $\left| \frac{\partial E_i(k_\perp, k_z)}{\partial k_z} \right|^{-1}$  diverges for stationary points of dispersion relation  $E(k)$  giving rise to the Van-Hove singularities, typical of 1D systems (Fig. 1.4). In Fig. 1.5 a schematic illustration of the DOS of

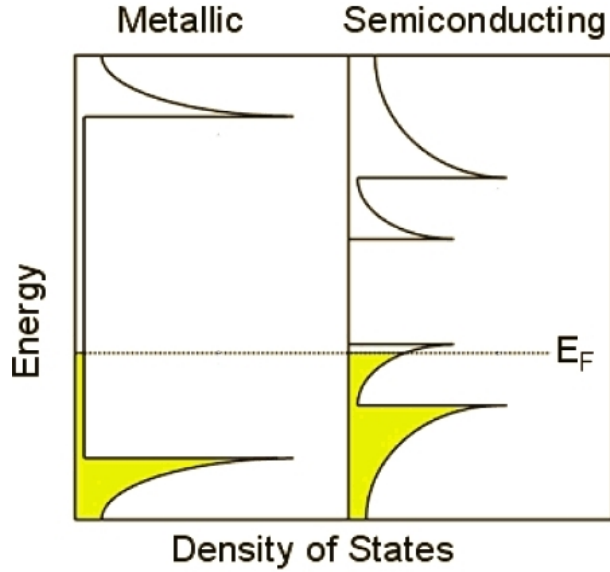


**Figure 1.5:** A schematic illustration of the density of states (DOS) of metallic and semiconducting SWCNTs. The shadow (yellow) indicates the occupied state [33].

metallic and semiconducting SWCNTs are shown. By combining scanning tunnelling microscopy (STM) and spectroscopy (STS) it is possible to correlate the electronic properties of SWCNTs with their structure [34–36], confirming theoretical predictions on the metallic or semiconducting character of SWCNTs [29]. In scanning tunnelling spectroscopy, the tip is positioned at an appropriate point on the sample and the tunnelling current ( $I$ ) is measured as a function of the bias voltage ( $V$ ) between the tip and the sample. According to a simple but

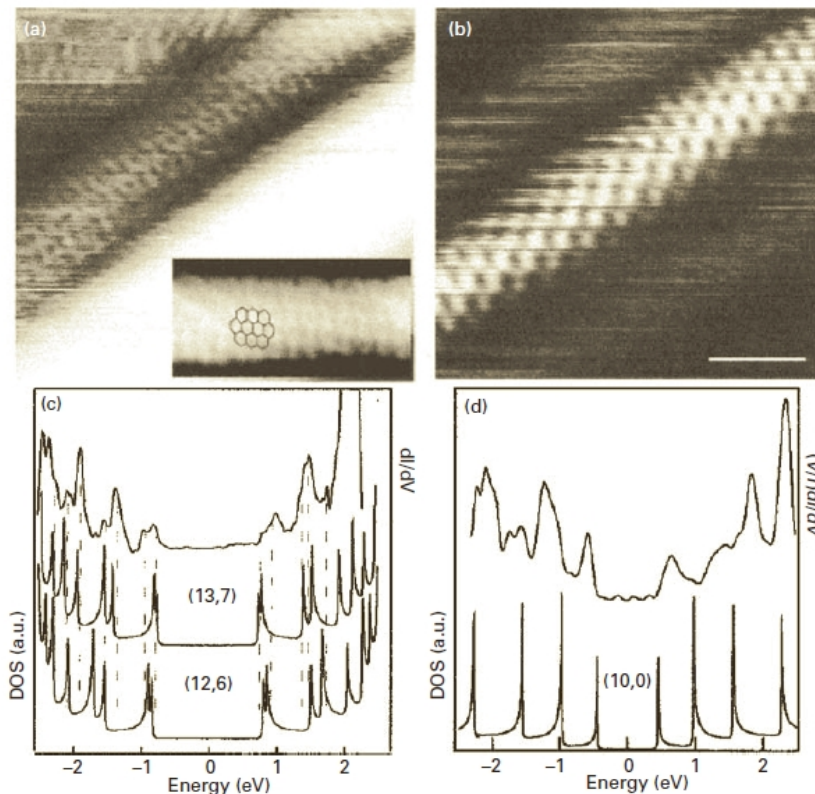


**Figure 1.6:** STM images and STS spectra of SWNTs, from Ref. [34]. (a) An atomic resolution image of a (13, 7) tube, (b) an image of a (10, 0) tube, (c) a comparison of the DOS obtained from experiment (upper curve) and tight-binding calculation for the (13, 7) SWCNT (second curve from top); the calculated DOS for a (12, 6) tube is included for comparison, (d) a comparison of the DOS obtained from experiment (upper curve) and calculation for the (10, 0) SWCNT [34].

realistic model, the derivative of the I-V curve gives an approximation to the density of electronic states (DOS), confirming theoretical prediction. In particular, M. Ouyang and co-workers [36] confirmed a further aspect foreseen by theoretical calculation, that for some metallic tubes, curvature can have the effect of opening a gap at the Fermi level, effectively destroying the metallic

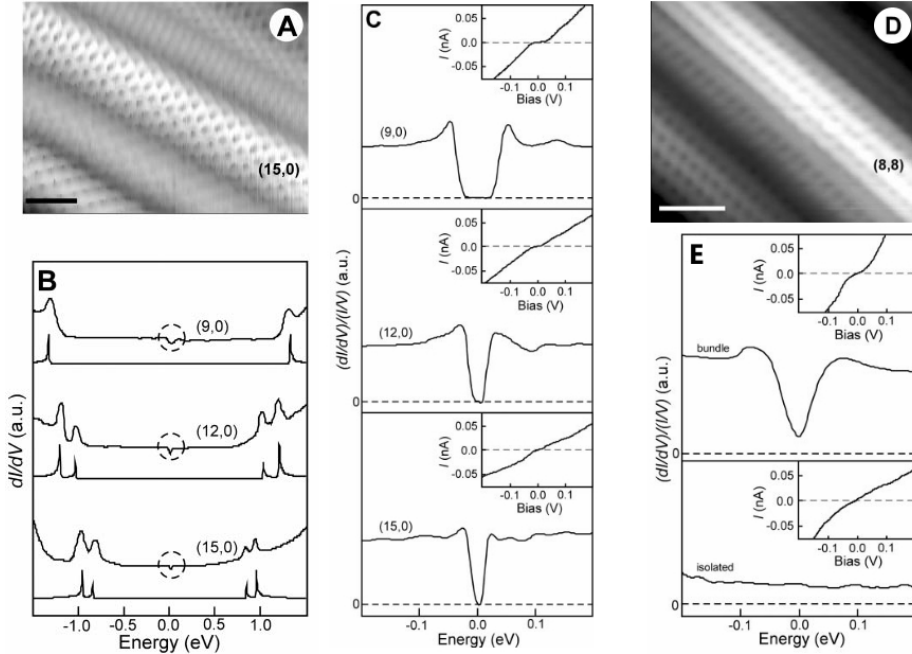


**Figure 1.7:** Figure adapted from Ref. [36]. (A-C) atomic structure and spectroscopy of “metallic” zig-zag SWCNTs. (A) Typical atomically resolved STM image of a (15, 0) SWCNT (scale bar = 1 nm). (B) Tunneling conductance data,  $dI/dV$ , for different zig-zag SWCNTs, with corresponding calculated DOS shown below each experimental curve. (C) Typical high-resolution normalized conductance  $(dI/dV)/(I/V)$  curves and measured I-V curves (insets) for (9, 0), (12, 0), and (15, 0) tubes, respectively. (D-E) Atomic structure and spectroscopy of armchair SWCNTs. (D) STM image of an (8, 8) armchair SWCNT. (E) High-resolution  $(dI/dV)/(I/V)$  and measured I-V (inset) data for bundles and isolated (8, 8) SWCNTs. [36].

character [36]. In Fig. 1.7 some of the gaps observed in metallic zigzag tubes are shown. For isolated armchair nanotubes (n, n), no gap was seen, confirming their theoretical metallic character. However, for armchair tubes in bundles, a small suppression in the density of states, called pseudogap, was found.

Although STM and STS are the most powerful techniques for correlating the structure of SWCNTs with their electronic characteristics, also Raman spectroscopy is a very useful technique in this area [37–40]. Both the G-band and the radial breathing feature can be used to distinguish between metallic and



semiconducting nanotubes. In SWCNTs the G-band is composed of two components, one peaked around  $1590\text{ cm}^{-1}$  ( $G^+$ ) and the other peaked at about  $1570\text{ cm}^{-1}$  ( $G^-$ ). The Dresselhaus group and others have shown that the line-shape of the  $G^-$  feature is highly sensitive to whether the SWCNT is metallic or semiconducting [38, 39]. The same group showed that the radial breathing mode can be used to obtain values of  $E_{ii}$ , the electronic transition energies, for individual tubes. This was achieved through a careful analysis of the laser energy dependence of the Stokes and anti-Stokes Raman spectra of nanotubes [40]. Regarding the transport properties of SWCNTs, we consider the transport behaviour of metallic nanotubes first. The transport behaviour of metallic nanotubes is essentially that of a quantum wire, so that conduction occurs through well separated, discrete electron states [28]. Thus, the resistance does not increase smoothly as the length of the wire is increased, but is the same independent of length, assuming no scattering. An important aspect of quantum wire behaviour is that transport along the tubes has a ballistic nature. Transport in semiconducting SWCNTs is more complicated, and appears to be diffusive rather than ballistic [41]. However, experiments have found evidence for extremely high mobilities in semiconducting SWCNTs [42].

### 1.1.1 Interaction with gases

The interaction between gas molecules and carbon nanotubes has been studied by experimental [43–47] and theoretical works using ab-initio calculations and density functional theory (DFT) [48–50]. In fact,  $\pi$  electrons distribution around the CNT make it electrochemically active, therefore when oxidizing or reducing gas molecules, e.g.  $\text{NO}_2$  or  $\text{NH}_3$ , are adsorbed onto carbon nanotubes surface, the charge transfer change the electronic properties like the band structure, the DOS, the electrical conductivity of CNTs. One of the first works based on DFT was performed by Zhao *et al.* who study the interaction between molecule like  $\text{NO}_2$ ,  $\text{O}_2$ ,  $\text{H}_2\text{O}$ ,  $\text{NH}_3$ ,  $\text{CH}_4$ ,  $\text{CO}_2$ ,  $\text{H}_2$ ,  $\text{N}_2$ , Ar and SWCNTs with different chirality (the obtained results are in Table 1.2). Gas molecule adsorption on the SWCNT surface may induce a significant variation of the electronic properties due to the charge transfer. In Fig. 1.8 the electronic DOS of  $\text{NH}_3$  adsorbed, pure and  $\text{NO}_2$  adsorbed on (10, 0) carbon nanotube (respectively in top, mid and bottom panel) are shown. The  $\text{NH}_3$  effect is weaker with

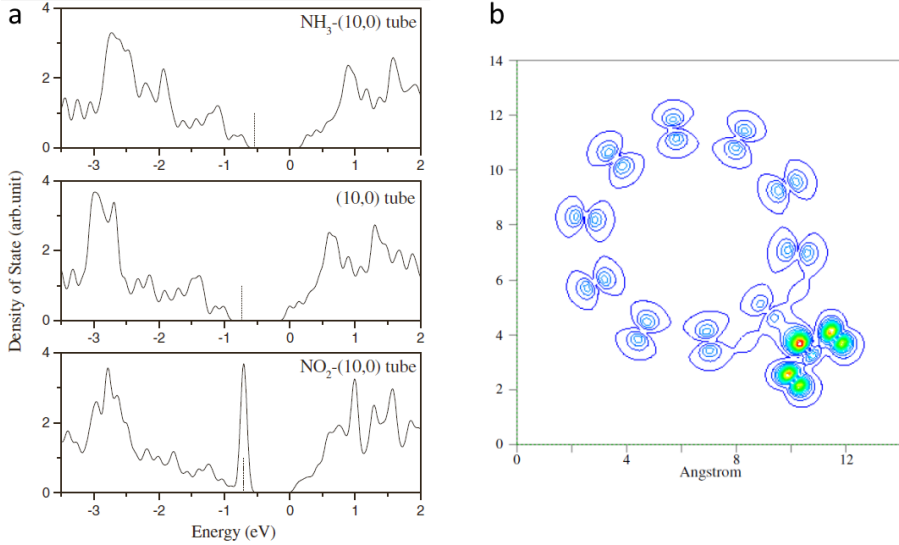


**Figure 1.8:** (a) Electronic DOS of NH<sub>3</sub> adsorbed (top panel), pure (mid panel), NO<sub>2</sub> adsorbed (bottom panel) on (10, 0) carbon nanotube. Dashed lines denote the Fermi level. Modification of the DOS is more pronounced in NO<sub>2</sub> than NH<sub>3</sub>. (b) Contour plot of electron density (slice passing through SWCNT and NO<sub>2</sub> molecule) [48].

respect to NO<sub>2</sub> interaction which shift the Fermi level into the valence band. This theoretical results are in accordance with some experimental findings that reported a significant increment of the electrical conductivity upon exposure of NO<sub>2</sub> [43]. It has been shown by Collins *et al.* that also the presence of oxygen induce significant effects on the conductivity and the DOS of CNTs In general, the presence of O<sub>2</sub> make carbon nanotubes p-type semiconductors [44]. In Table 1.2 the overall results obtained by Zhao *et al.*, i.e. the equilibrium distance  $d$  between the molecule and the tube, the adsorption energy  $E_a$  defined as  $E_a(d) = E_{tot}(tube + molecule) - E_{tot}(tube) - E_{tot}(molecule)$ , and charge transfer  $Q$  which denotes the total Mulliken charge number on the molecules (positive  $Q$  means charge transfer from the molecule to the tube) are reported. For molecules like H<sub>2</sub>O, NH<sub>3</sub>, CO<sub>2</sub>, which are donors, i.e. they inject electrons on the nanotube surface, the charge transfer is low (0.01-0.035 electron per molecule) and the adsorption energy is weak ( $\leq 0.2$  eV), while for NO<sub>2</sub> and O<sub>2</sub>,

	NO <sub>2</sub>	O <sub>2</sub>	H <sub>2</sub> O	NH <sub>3</sub>	CH <sub>4</sub>	CO <sub>2</sub>	H <sub>2</sub>	N <sub>2</sub>	Ar
(10, 0) SWNT									
$d$ (Å)	1.93	2.32	2.69	2.99	3.17	3.20	2.81	3.23	3.32
$E_a$ (meV)	797	509	143	149	190	97	113	164	57
$Q$ (e)	-0.061	-0.128	0.035	0.031	0.027	0.016	0.014	0.008	0.01
Site	T	B	T	T	C	C	C	C	C
(5, 5) SWNT									
$d$ (Å)	2.16	2.46	2.68	2.99	3.33	3.54	3.19	3.23	3.58
$E_a$ (meV)	427	306	128	162	122	109	84	123	82
$Q$ (e)	-0.071	-0.142	0.033	0.033	0.022	0.014	0.016	0.011	0.011
Site	T	B	T	T	C	C	C	C	C
(17, 0) SWNT									
$d$ (Å)	2.07	2.50	2.69	3.00	3.19	3.23	2.55	3.13	3.34
$E_a$ (meV)	687	487	127	133	72	89	49	157	82
$Q$ (e)	-0.089	-0.096	0.033	0.027	0.025	0.015	0.012	0.006	0.01
Site	T	B	T	T	C	C	C	C	C

**Table 1.2:** Equilibrium tube-molecule distance ( $d$ ), adsorption energy ( $E_a$ ) and charge transfer ( $Q$ ) of various molecules on (10, 0), (17, 0) and (5, 5) individual SWCNTs. Adsorption sites: T (top of an carbon atom), B (top of the centre of the C-C bond), C (top of the centre of carbon hexagon) [48].

acceptors which induce higher charge transfer (0.06-0.14 electron per molecule), the adsorption energies are also greater ( $\geq 0.4$  eV).

In order to exemplify the interaction between gas molecules and bundle of SWCNTs, in Fig. 1.9 we report the case of H<sub>2</sub> molecule adsorbed on (10, 10) SWCNTs

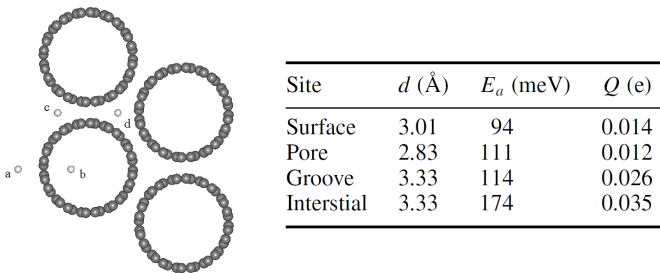


**Figure 1.9:** Illustration of possible adsorption sites for the H<sub>2</sub> molecule in the (10, 10) SWCNTs bundle. (a) Surface; (b) pore; (c) groove; (d) interstitial. In the table on the right, the equilibrium tube-molecule distance ( $d$ ), adsorption energy ( $E_a$ ) and charge transfer ( $Q$ ) on the different adsorption sites are reported [48].

bundle considered by Zhao *et al.* [48]. As we can observe from the table on the right of Fig. 1.9, the adsorption energy and charge transfer in the interstitial and groove sites are greater with respect to that on the surface sites. This can be explained thinking on the greater number of carbon nanotubes that interact with the molecule. But it is important to highlight that the possibility to be adsorbed in interstitial sites is reduced for large molecules.

We finally report the experimental results of Goldoni *et al.* using X-ray photoemission spectroscopy (XPS) in order to study the interaction between SWCNTs and gas molecules like  $SO_2$ ,  $NH_3$ ,  $O_2$  or  $NO_2$ . The authors show that the reaction with oxygen is not due to carbon nanotube interaction, but to the presence of residual contaminants of the purification process (especially the species containing Na) [47]. Once these contaminants are completely removed, SWCNTs appear not sensitive to  $O_2$ ,  $CO$ ,  $H_2O$  e  $N_2$ , while a strong sensitivity to  $NO_2$ ,  $SO_2$ , and  $NH_3$  is still observed. In Fig. 1.10 XPS C 1s spectra of the SWCNT clean sample, i.e. without contaminants, during gas exposure of  $SO_2$ ,  $NH_3$  and  $NO_2$  are shown.

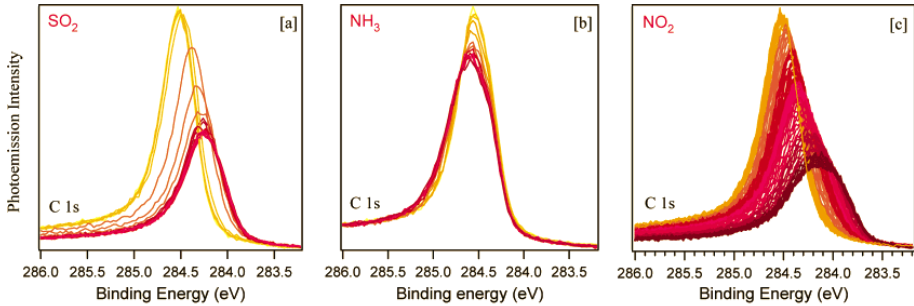


**Figure 1.10:** C 1s spectra of the clean SWCNT bucky-paper measured while exposing the sample at 150 K to  $SO_2$  (a),  $NH_3$  (b), and  $NO_2$  (c) at partial pressures of about  $10^{-8}$  mbar [47].

The shift of C 1s peak during gas exposure is toward lower binding energies in the case of  $SO_2$  and  $NO_2$  (Fig. 1.10 a and c), while during  $NH_3$  exposure (Fig. 1.10 b) the shift is smaller and toward higher binding energies. If these binding energy shifts are ascribed to shifts of the nanotube chemical potential, the  $NO_2$  and  $SO_2$  molecules bound to SWCNTs act as charge acceptors, while the  $NH_3$  molecules act as charge donors, in full agreement with the experimental

observations reported by Kong *et al.* [43] and theoretical results [48].

## 1.2 Synthesis of carbon nanotubes

Carbon nanotubes are synthesized by three main popular techniques: Chemical Vapor Deposition (CVD), arc-discharge and laser ablation. None of these techniques produce pure nanotubes, so that purification processes are needed to obtain CNTs of high purity [28]. The Chemical Vapor Deposition (CVD)

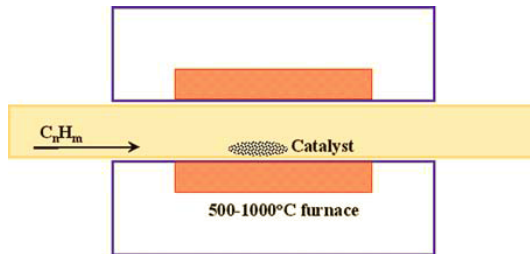


**Figure 1.11:** Typical CVD experimental set-up [51].

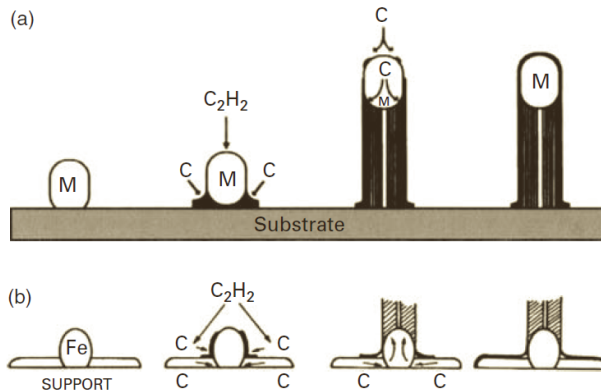


**Figure 1.12:** An illustration of the tip growth mechanism (upper diagram) and the base growth mechanism (lower diagram) of nanotube growth. M (or Fe) represents the metal (or iron) catalyst nanoparticle [28].

growth process is the more suitable technique for the large mass production of high purity carbon nanotubes. The typical CVD set-up is reported in Fig 1.11: a catalytic material (typically metal nanoparticles, as Fe, Ni, Co or others) is heated at high temperature ( $\sim 500\text{-}1000^\circ\text{C}$ ) and exposed to a flux of carbon-containing gas such as methane, ethylene, acetylene, carbon monoxide, etc. The formation mechanism could be tip and base growth, as proposed by Baker *et al.* [ref], and illustrated in Fig 1.12. During the CVD process the hydrocarbon molecules dissociate and the C atoms are deposited on the metal nanoparticles leading to the formation of tubular structures characterized by  $sp^2$  bonds. It is possible to obtain both multi-wall carbon nanotubes (MWCNTs) or single-wall carbon nanotubes (SWCNTs) by CVD method, but in general the temperatures used for synthesizing SWCNTs are higher than those used for MWCNTs, because SWCNTs have smaller diameters and then higher tension energy. Typical temperatures are  $550\text{-}750^\circ\text{C}$  for MWCNTs [32] and  $800\text{-}1200^\circ\text{C}$  for SWCNTs [28]. Arc-discharge method, traditionally used to produce buckyballs, consists in an electric arc (current of ionized gas) of carbon atoms, generated between two graphite rods at high temperatures by applying a very high electric field. The set-up (Fig. 1.13, left panel) is composed of a sealed chamber, where two graphite electrodes are separated by a distance of the order of millimeters with a voltage of 20-30 V.

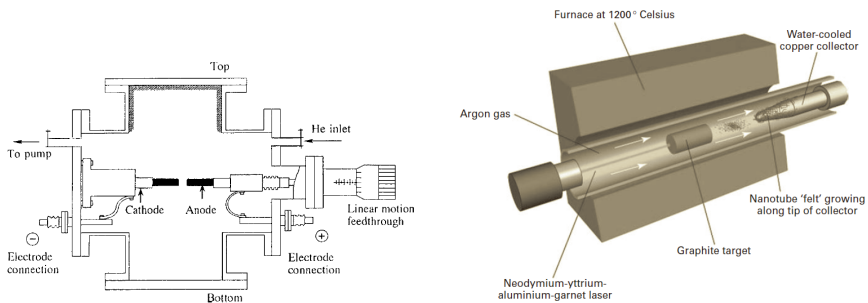


**Figure 1.13:** Schematic illustration of arc-evaporation (left panel) and laser-vaporization apparatus (right panel) for the production of carbon nanotubes [28].

The laser ablation method consists in the synthesis of CNTs by the removal of matter from the surface of a graphite target through laser pulses. The graphite

target is generally placed in a reactor heated at high temperature and the effect of the laser is to vaporize the surface (Fig. 1.13, right panel). Catalytic metals (Fe, Co, Ni are the most popular) are often added to the target in order to improve the yield. After the vaporization induced by the laser, the carbon vapor condenses on a water-cooled surface of the reactor to produce nanotubes. The laser ablation method typically produces mostly single-wall nanotubes with a relatively narrow diameter, in bundles [52].

### 1.3 Gas sensors based on SWCNTs

SWCNTs are appealing systems to be used as gas sensors at least for two reasons: the huge surface to volume ratio and their one-dimensional nature that makes them very sensitive to very small external perturbations [53]. Furthermore, gas sensors based on SWCNTs are able to operate at room temperature. As referred to Section 1.1, gas molecules adsorbed on the carbon nanotube surface could act as dopants (donors or acceptors), they could shift the Fermi level or change the band structure of SWCNT. Such a change may be easily detected, once the nanotubes are inserted within an electronic device. The several different types of electrochemical sensors based on SWCNTs electrical properties (e.g. resistance [17, 43, 54–56], capacitance [57] or frequency [58] variation, ionization chamber with CNTs [59]) can be grouped in: sensors based on impedance, piezoelectric transducer-based sensors and solid state miniaturized sensors [60]. The chemFET (chemical Field Effect Transistor) and the chemiresistor belong to the solid state miniaturized sensors category. In Fig. 1.14 the CNT-based device

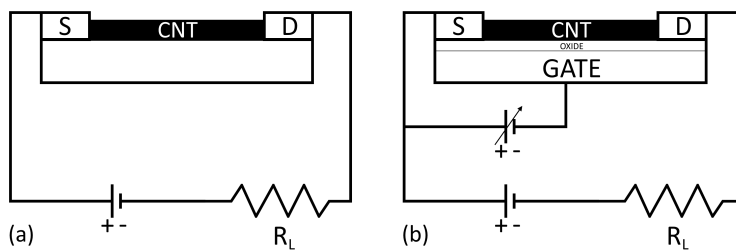


**Figure 1.14:** CNT device and electronic circuit scheme in the chemiresistor (a) and chemFET (b) configuration.

and the electronic circuit scheme in the chemiresistor and chem-FET configuration are shown.

In the chemiresistor configuration, the CNTs create a bridge between two electrodes (to which a certain potential is applied), allowing the current flow. When a reactive gas molecule is adsorbed on the nanotube surface, the charge transfer alters the electrical resistance of the CNTs.

The chemFET configuration is similar to the chemiresistor configuration, except for the fact that the current flowing through the CNTs between source (S) and drain (D) electrodes is modulated by a third electrode, the gate (G), separated from the other two by a thin layer of insulating material (typically  $\text{SiO}_2$ ). This metal/CNT semiconductor/metal system has the characteristics of a p-type transistor [43]. An example of response to  $\text{NO}_2$  and  $\text{NH}_3$  exposure of a CNT-based chemFET is shown in Fig. 1.15, taken from one of the first work on the gas sensing properties of CNTs.

In Table 1.3 a summary of pristine CNT chemiresistors and ChemFETs sensing

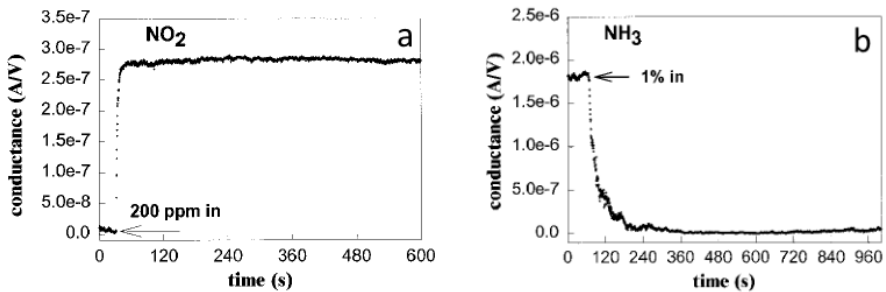


**Figure 1.15:** Electrical response of a semiconducting SWCNT to gas molecules in a chem-FET configuration, but at fixed gate voltage (Figure adapted from [43]). (a) Conductance (under  $V_{gate} = +4$  V, in an initial insulating state) versus time in a 200 ppm  $\text{NO}_2$  flow. (b) Conductance ( $V_g = 0$  V, in an initial conducting state) versus time recorded with the same SWCNT sample in a flow of Ar containing 1%  $\text{NH}_3$  [43]. These conductance variations to oxidizing (i.e.  $\text{NO}_2$ ) or reducing (i.e.  $\text{NH}_3$ ) molecules indicate the p-type character of the SWCNT response.

performance is shown [12]. The chemFET configuration tends to be more sensitive to gas because of the possibility to modulate the conductance of CNTs via the gate voltage. However it requires more sophisticated electronics and much higher costs [17]. Chemiresistors have been chosen for the gas sensing



CNT type	Sensor configuration	Targeted analytes	Detection limit	Response time (s)	Reversibility
Single SWNT	ChemFET	NO <sub>2</sub> , NH <sub>3</sub>	2 ppm (NO <sub>2</sub> ) 0.1% (NH <sub>3</sub> )	<600	Irreversible
SWNTs	ChemFET	Alcoholic vapors (methanol, ethanol, 1-propanol, 2-propanol, and tert-butanol.)	N/S	5–150	Reversible (–20 V gate bias potential)
SWNTs	Chemiresistor	O <sub>2</sub>	N/S	N/S	Reversible
SWNTs	ChemFET	DMMP	<1 ppb	1000	Reversible (3 V gate bias)
MWNTs	Chemiresistor	NO <sub>2</sub>	10 ppb	N/S	Reversible (165 °C)
SWNTs	Chemiresistor	NO <sub>2</sub> , Nitrotoluene	44 ppb (NO <sub>2</sub> ), 262 ppb (Nitrotoluene)	600	Reversible (UV)
MWNTs	Chemiresistor	NH <sub>3</sub>	10 ppm	~100	Reversible
SWNTs	Chemiresistor	SOCl <sub>2</sub> , DMMP	100 ppm	10	Irreversible
SWNTs	Chemiresistor	O <sub>3</sub>	6 ppb	<600	Reversible
MWNTs	Chemiresistor	NO <sub>2</sub>	5–10 ppb	~600 (165 °C)	Reversible (165 °C)
SWNTs	Chemiresistor	methanol, acetone	N/S	~100	N/S
SWNTs	Chemiresistor	H <sub>2</sub> O	N/S	10–100	Reversible
Carboxylated SWNT	Chemiresistor	CO	1 ppm	~100	Reversible

**Table 1.3:** Summary of selected sensing performance of pristine CNT chemiresistors and chemFETs (N/S=Not-stated) [12].

measurements, because they are simpler to produce and to manage. For this type of sensors interdigitated electrodes (IDE) are often used in order to have more sensitive area and to increase the number of contacts between the electrodes and the CNTs. The main techniques to deposit CNTs are: direct CVD on the substrate (discussed in Section 1.2); deposition of a solution in which the CNTs are dispersed, e.g. by drop-casting method or ink-jet printing. Finally, in order to align CNTs between the electrodes, a method called dielectrophoresis (DEP), which consists on applying an AC electric field between the electrodes during the deposition process, has been used by Suheiro *et al.* [56] to build a MWCNT-based ammonia gas sensor.



# Chapter 2

## Experimental techniques

In this chapter the general samples preparation, the set-up for chemiresistor gas sensing measurements and the techniques applied to characterize the sensitive layers are described.

### 2.1 Gas sensing measurements

#### 2.1.1 General samples preparation

Here the general procedure for the preparation of SWCNT-based samples, tested as gas sensors and discussed in chapter 3 and 4, is reported. Whereas the hybrid architectures preparation is described in more detail in a specific sections of chapter 5. CNT thin layers have been deposited by drop-casting a solution containing water, NaOH and SLS (Sodium Lauryl Sulphate) in which SWCNT (CarboLex Inc.) are dispersed, on either ceramic or plastic substrates. Alumina plates ( $10 \times 15 \text{ mm}^2$ ) with Pt interdigitated finger electrodes have been selected as ceramic substrates (Electronics Design Center, Case Western Reserve University, Cleveland, Ohio), while on plastic substrates samples (SWCNT on printable transparency foils) two stripes of Ag paste have been deposited at the opposite sides of the films, as electrical contacts. The choice of the substrates was dictated by the idea that the  $\text{Al}_2\text{O}_3$  plates appear to be more mechanically robust and potentially stable over a long time outdoor operation, while the

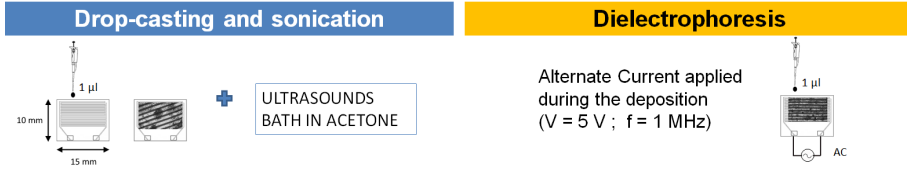


**Figure 2.1:** Sketch of the procedures to prepare thin SWCNT layers on ceramic substrate ( $10 \times 15 \text{ mm}^2$   $\text{Al}_2\text{O}_3$  plates with Pt interdigitated finger electrodes): drop-casting followed by sonication in acetone ultrasounds bath (left panel) and dielectrophoresis method (right panel).

use of cheap flexible plastic substrates discloses possible production for ink-jet printing process, or application in flexible integrated circuits [61,62]. In Fig. 2.1 the procedures to prepare thin SWCNT layers on ceramic substrate, i.e. drop-casting followed by sonication in acetone ultrasounds bath and dielectrophoresis method, are shown. In the first method, after the deposition by drop-casting of the SWCNT solution using a micropipette, sonication of the device was carried out in acetone (three times for 15 minutes, testing the gas sensing response after each sonication). The second method, i.e. dielectrophoresis assisted deposition, following the indications of Suehiro *et al.* [56], consists in applying a voltage of 5 V between the Pt interdigitated electrodes while an ac current at 1 MHz was flowing, during the deposition by drop-casting of the solution containing SWCNTs. The gas sensing response of this kind of samples is discussed in chapter 3. Also in the case of SWCNT on plastic substrates (considered in chapter 4), the sensing layer deposition was carried out by drop-casting method, starting from the solution in which SWCNT are dispersed. The preparation of functionalized samples has been carried out by adding nanoparticles of metal oxides to the SWCNT solution before the deposition process.

### 2.1.2 Data acquisition and gas sensing set-up

In Fig. 2.2 a general sketch of the SWCNT-based sample used as chemiresistor gas sensor is shown. The sensitive element is composed by bundles of SWCNTs that change their conductivity in presence of certain gases, e.g.  $\text{NH}_3$ ,  $\text{NO}_2$ . In the case of samples prepared on ceramic substrate the electrical contacts are Pt interdigitated electrodes, while the samples on plastic substrates

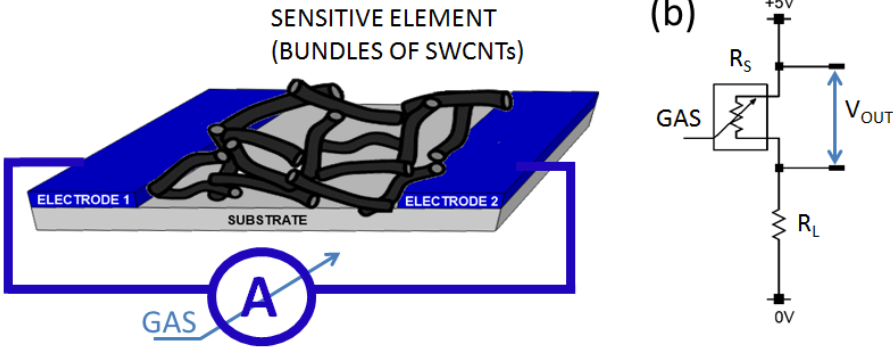


**Figure 2.2:** (a) Sketch of the SWCNT-based sample used as chemiresistor gas sensor: the sensitive element is composed by bundles of SWCNTs that change their conductivity in presence of certain gases, e.g.  $\text{NH}_3$ ,  $\text{NO}_2$ . (b) Scheme of the circuit for the electrical measurements: a constant voltage  $V_C=5\text{V}$  is applied across the sensor in series with a load resistor. By monitoring the voltage  $V_{out}$  across the sample, the sensor resistance is measured.

have two stripes of Ag paste as electrodes. The sensor conductance (or resistance) is detected by the electronic circuit to which the device is connected. The basic electronic circuit for chemiresistor gas sensing measurements (Fig. 2.2 b) consists in a load resistor ( $R_L$ ) in series with the sample resistance ( $R_S$ ), at which a constant voltage ( $V_C = 5 \text{ V}$ ) is applied. By monitoring the voltage  $V_{OUT}$  across the sample, the  $R_S$  is measured. In fact, by using the Ohm's law, the current flowing through the sample is

$$I = \frac{V_C - V_{OUT}}{R_L} \quad (2.1)$$

and from this value we obtain the sample resistance  $R_S = V_{OUT}/I$ , i.e. by using the following equation:

$$R_S = \frac{V_{OUT} \cdot R_L}{V_C - V_{OUT}} \quad (2.2)$$

where  $V_{OUT}$  is the voltage drop measured upon gas exposure across the sample resistance,  $R_L$  is the load resistor value and  $V_C$  is the fixed voltage (5 V, in our measurements). In order to detect the presence of gases, the resistance variation of the sensor ( $\Delta R = R_S - R_0$ ) upon gas exposure was measured, where  $R_0$  is the baseline resistance value, i.e. the resistance value measured just before each

exposure to the polluting gas. An example of resistance variation during gas exposure is sketched in Fig. 2.3 a. By measuring the sensor response  $\Delta R/R_0$  for several gas exposures at different concentrations, it is possible to draw the response curve (Fig. 2.3 b).

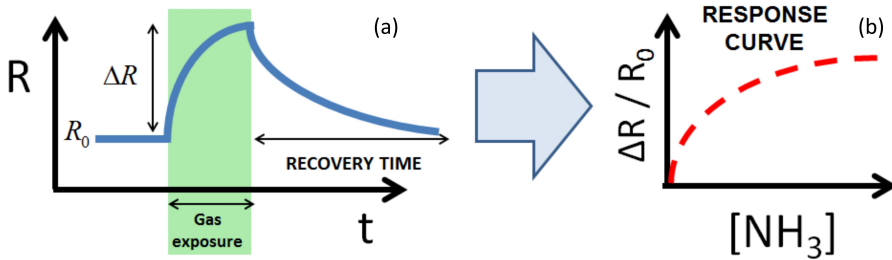


**Figure 2.3:** (a) Sketch of resistance  $R$  vs time  $t$  during gas exposure. After a sequence of gas exposures at different concentrations, it is possible to draw the response curve (b), i.e. sensor relative response  $\Delta R/R_0$  vs gas concentration. Figure adapted from [63].

All sensors, including humidity and temperature sensors, were mounted on a specifically designed circuit board (Fig. 2.4) connected to a personal computer through a National Instrument shielded I/O connector block for 68-pin (NI SCB-68) and PCIe-6251 data acquisition board. The sensors signal has been acquired by a home-made software, written in LabVIEW environment (block diagram of the software is shown in Fig. 2.5).

Gas exposure have been carried out either in a gas testing chamber or in the laboratory air. During measurements in lab air, the board with sensors has been left outside the gas testing chamber (Fig. 2.6) and the response to ammonia has been tested by exposing the sensors to a point-like source of liquid ammonia (less than 50 ml in a small container) placed at different distances (10 to 120 cm) from the sensors. The gas concentration for the exposures in lab air was measured with a calibrated, commercially available, chemiresistor gas sensor (Figaro, Mod. TGS 2602, Fig 2.7). The reliability of this sensor calibration curve was cross-checked by measurements in the testing chamber with the calibrated mass flow controllers (MFCs) and target gas. These kind of measurements were carried out either in the dark or under ambient light, giving rise to the same response. The testing chamber was selected mainly for the

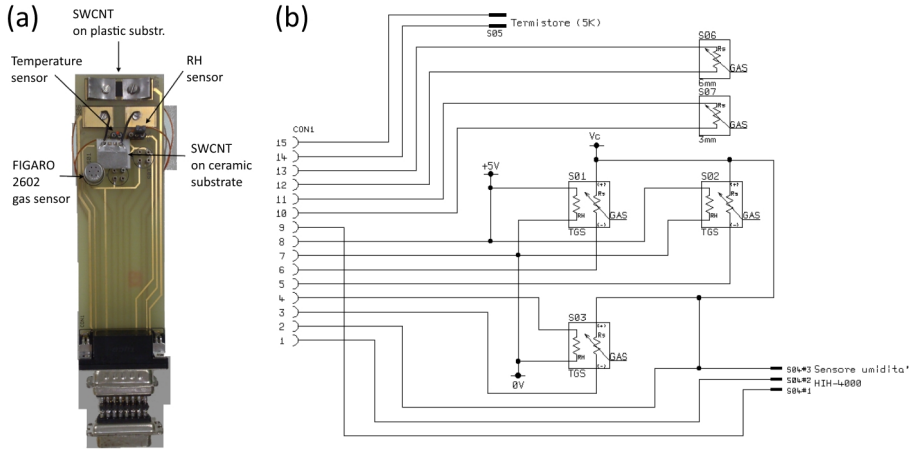


**Figure 2.4:** (a) Board specifically designed for the location of relative humidity (R.H.), temperature, TGS Figaro2602 sensor and CNT-based ammonia gas sensors. (b) General scheme of the electronic acquisition system.

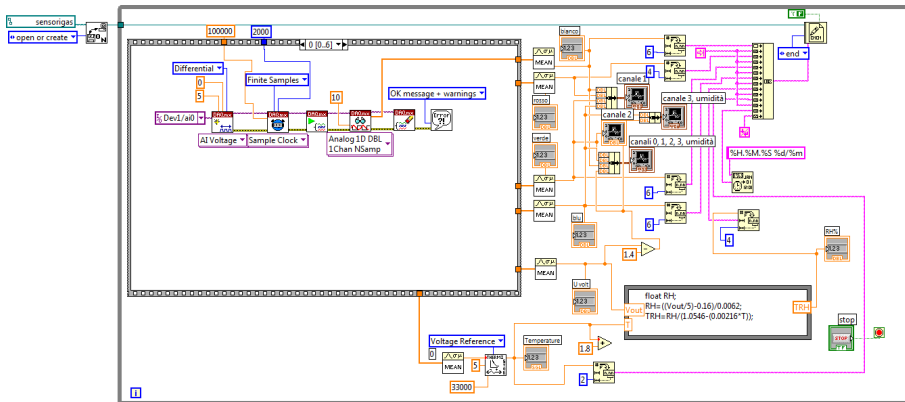


**Figure 2.5:** Block diagram of the home-made software, written in LabVIEW environment, to acquire the 6 different input signal channels (4 channels dedicated to gas sensors signals, 1 channel for relative humidity and 1 channel for temperature measurement.) In particular, the screen shot shown the channel related to a CNT-based sensor: the  $V_{out}$  was measured in differential acquisition across the sample in a range of 0 - 0.1 V.

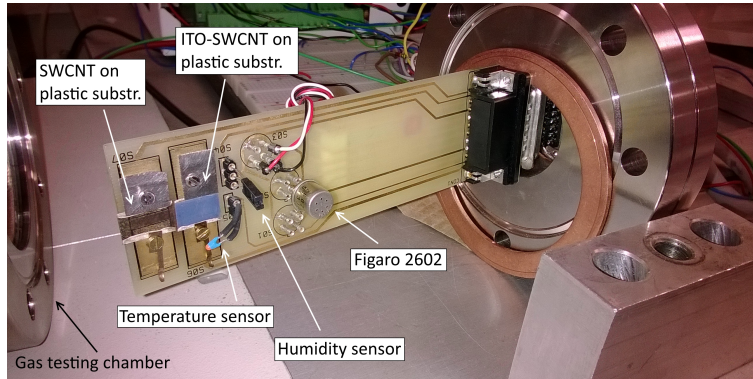


**Figure 2.6:** The measurements outside the testing chamber have been carried out in the laboratory air by exposing the sensors to a point-like source of liquid ammonia, placed at different distances from the board with sensors.

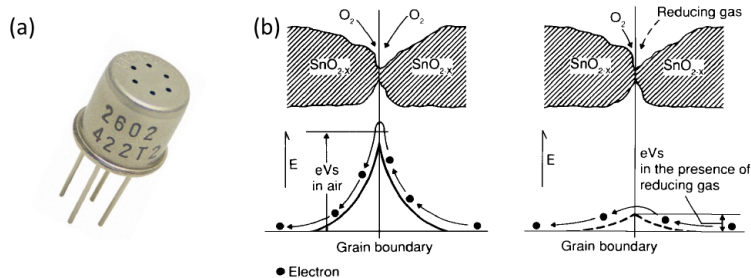


**Figure 2.7:** (a) Picture of the reference chemiresistor gas sensor (Figaro, Mod. TGS 2602) during the measurements in lab air. (b) Model of inter-grain potential barrier in oxygen atmosphere and in the presence of a reducing gas for the Figaro 2602 gas sensor [64].

sensor calibration, and for measurements upon  $\text{NO}_2$  exposure, while exposures to acetone, ethanol, water vapor and most of the  $[\text{NH}_3]$  measurements were carried out in the laboratory atmosphere, which provides an environment closer to the final destination of the sensors, although signal fluctuations can be larger with respect to the measurements carried out in the sealed, testing chamber (a discussion about this fluctuations is given in chapter 3).

In Fig. 2.8, a picture and a scheme of the gas sensing set-up with the testing



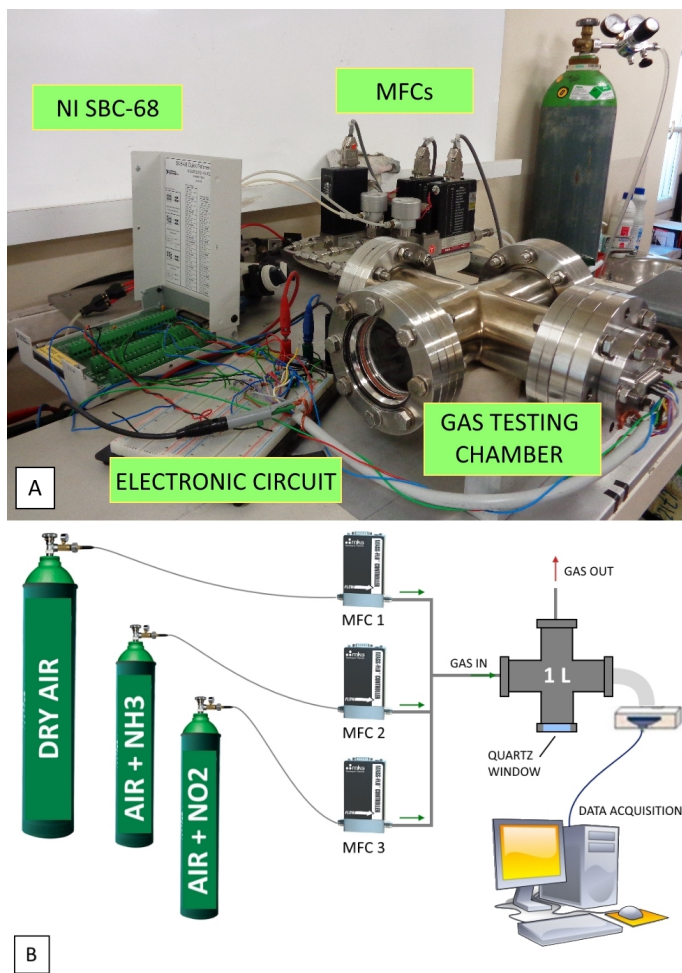


**Figure 2.8:** (a) Picture of the experimental set-up for gas sensing measurements. (b) Scheme of the gas sensing experimental set-up equipped by three mass flow controllers (MFCs), a gas testing chamber ( $V = 1$  l) and a PC for data acquisition. The certified cylinders contain  $47.1 \pm 1.2$  ppm  $\text{NH}_3$  or  $10.00 \pm 0.78$  ppm  $\text{NO}_2$ , both diluted in dry air. The range of fluxes are 0 - 500 sccm for MFC 1 connected to dry air cylinder, and 0 - 10 sccm for MFC 2 and MFC 3, connected to cylinders with  $\text{NH}_3$  and  $\text{NO}_2$ , respectively.

chamber are shown. The gas mixing system and gas testing chamber were built in-house. The chamber is composed by two cross stainless steel cylinders (the total volume of the chamber is 1 l) and it is provided with a quartz window which allows measurements under illumination, e.g. UV light. The system is equipped with three gas cylinders containing dry air (oxygen 21%, nitrogen 79%),  $47.1 \pm 1.2$  ppm  $\text{NH}_3$  or  $10.00 \pm 0.78$  ppm  $\text{NO}_2$  diluted in dry air (certified by S.I.A.D. S.p.A.), and three mass-flow controllers (MFCs). Two low-flow MFCs (max flow = 10 sccm) for controlling the analytes flow rate from the gas cylinders containing  $\text{NH}_3$  or  $\text{NO}_2$  diluted in dry air, and a high-flow MFC (max flow = 500 sccm) employed for further dilution in dry air and for the refresh of the chamber, during which signal recovery is recorded. In a typical gas testing chamber measure, the total flow is 50 sccm or, for further analyte dilution, 500 sccm. Finally, for UV curing after  $\text{NO}_2$  exposures (discussed in chapter 4), a UV led (ENFIS UNO Air Cooled Light Engine [65]) with an excitation wavelength at 350 nm and a power of 80 mW, placed in front of the quartz optical window has been used.

## 2.2 Characterization techniques

The samples were characterized by micro-Raman and X-ray photoemission spectroscopies, as well as by scanning electron microscopy (SEM) and atomic force microscopy (AFM).

Micro-Raman data were collected on the CGS device with a Renishaw-Invia system (Fig. 2.9), equipped with a 633 nm laser source. A 1800 lines/mm grating was used and the laser light was focussed onto the sample with a 50 $\times$  objective.



**Figure 2.9:** Renishaw-Invia system equipped with a 633 nm laser source utilized for micro-Raman spectroscopy.

XPS data were collected with a VG-Scienta spectrometer and a twin anode X-ray source. The Al  $k_{\alpha}$  line at  $h\nu = 1486.6$  eV was used to excite the sample. The analyser was operated in transmission mode with a pass energy of 200 eV, yielding an overall resolution of 1.2 eV. For the XPS analysis, samples were prepared by drop casting 1  $\mu\text{l}$  of CNT solution on a reference silicon wafer, previously cleaned in an ultrasonic bath. For the measurements on the extra samples prepared on glass substrates, in order to test the sonication effects, the

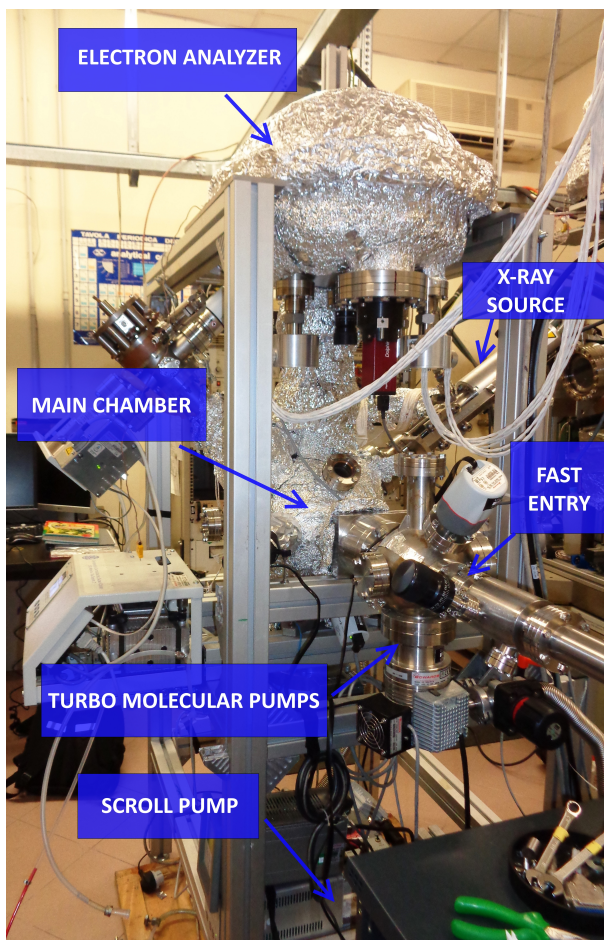


**Figure 2.10:** Set-up for X-ray Photoemission Spectroscopy, equipped with a VG-Scienta spectrometer and a twin anode X-ray source with Al  $k_{\alpha}$  line at  $h\nu = 1486.6$  eV and Mg  $k_{\alpha}$  line at  $h\nu = 1253.6$  eV.

Mg  $k_{\alpha}$  line at  $h\nu = 1253.6$  eV was used to excite the sample.

The surface morphology of each sample was characterized by Scanning Electron Microscope (SEM) and Atomic Force Microscope (AFM). SEM measurements were performed using a Zeiss SupraTM 40 working in a base pressure of

$4 \times 10^{-10}$  mbar.

AFM measurements were performed using a Solver P47-Pro NT-MDT equipment. Topographical images were acquired in semicontact mode using rectangu-

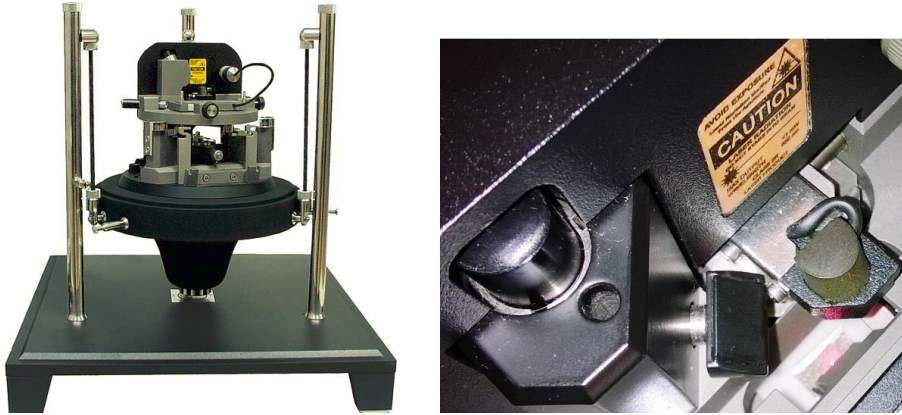


**Figure 2.11:** Atomic Force Microscope Solver P47-Pro NT-MDT used to acquired topographical images, current images and local I-V curve.

lar silicon cantilevers (HA\_NC ETALON NT-MDT series, tip curvature radius 10 nm, resonant frequency  $140 \pm 10$  kHz). Image analysis has been performed using Nova software.

Current images and local I-V curves were also acquired using a Solver P47-Pro SPM NT-MDT, in contact mode using rectangular silicon cantilevers (CSG01/10 NT-MDT series, single crystal silicon, n-type,  $0.01-0.025 \Omega\text{cm}$ , tip curvature radius 10 nm). For these type of measurements a bias voltage was set between the tip and the sample.



## Chapter 3

# Enhancing the response to ammonia gas

In this chapter, we present single-wall carbon nanotube (SWCNT) chemiresistor gas sensors (CGS) operating at room temperature, displaying an enhanced response to  $\text{NH}_3$ . High sensitivity is required to detect concentrations of polluting gases in the low-ppb range, for a realistic monitoring of the air quality in an urban environment. This limit has been so far virtually neglected, as most of the testing of new ammonia gas sensor devices based on CNTs is carried out above the ppm limit. In addition to a careful preparation of the SWCNT layers on ceramic substrates, through sonication and dielectrophoresis methods that improved the quality of the CNT bundle layers, the low-ppb limit is also attained by revealing and properly tracking a fast dynamics channel in the desorption process of the polluting gas molecules. Ammonia concentrations in air as low as 20 ppb have been measured, and a detection limit of 3 ppb is demonstrated, which is in the full range of the average  $\text{NH}_3$  concentration in an urban environment and well below the sensitivities so far reported for pristine, non-functionalized SWCNTs operating at room temperature.

### 3.1 Sample preparation and characterization

#### 3.1.1 Drop-casting and sonication vs dielectrophoresis method

CNT-based chemical resistors were prepared by drop casting  $4 \mu\text{l}$  of a SWCNT dispersion in a solution containing water, sodium hydroxide and sodium lauryl sulphate (CarboLex Inc.) onto a ceramic substrate with interdigitated Pt electrodes. Alumina plates ( $10 \times 15 \text{ mm}^2$ ) with Pt interdigitated finger electrodes were selected (Electronics Design Center, Case Western Reserve University, Cleveland, Ohio) for electrical measurements. A thin film of CNTs is required to allow charges, injected from ammonia when the molecules adsorb on the nanotubes, to reach the Pt electrodes of the substrate, and not be dispersed in the bundles of nanotubes. In order to enhance the sensitivity to ammonia gas, two strategies (which led to comparable results) have been applied. The first method is based on drop-casting and sonication. Indeed, to obtain a thin film of CNTs, after the drop-casting deposition, sonication of the device was carried out in acetone for an overall time of 45 minutes (the device was sonicated three times for 15 minutes). The second method, i.e. dielectrophoresis assisted deposition, started with drop casting  $4 \mu\text{l}$  of SWCNT dilution on the alumina substrate. During the solvent evaporation a constant voltage of 5 V (with a bias offset of 2 V) was applied between the interdigitated electrodes while an ac current at 1 MHz was flowing, following the indications of Suehiro et al [56].

#### 3.1.2 Layer characterization

The structural properties of the CNTs have been characterized by Raman spectroscopy. The Raman spectrum (3.1) shows the typical peaks of SWCNT [67]: the radial breathing modes (RBM, inset of Fig. 3.1) at  $170 \text{ cm}^{-1}$ , the G-band (with the  $G^-$  and  $G^+$  contributions, at  $1570 \text{ cm}^{-1}$  and  $1590 \text{ cm}^{-1}$  respectively) and the D-band at  $1320 \text{ cm}^{-1}$ . From the frequency of the RBM, we can estimate the diameter of the nanotube using the equation  $\omega_{RBM} = A/d_t + B$ , where  $d_t$  is the tube diameter and A and B are experimental parameters. For bundles of SWCNTs typical parameters are  $A = 234 \text{ cm}^{-1}$  and  $B = 10 \text{ cm}^{-1}$  [68]. Using these values in the equation reported above, with  $\omega_{RBM} \approx 170 \text{ cm}^{-1}$ , we ob-



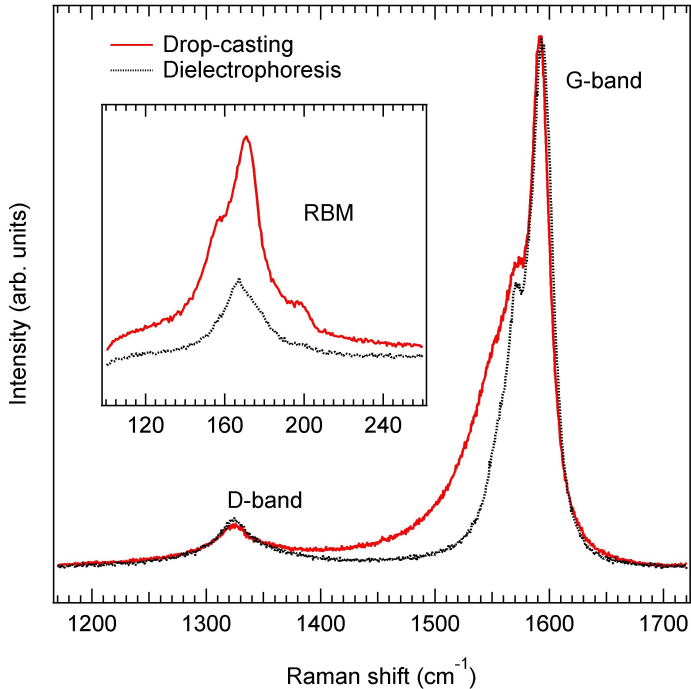


**Figure 3.1:** Raman spectra of SWCNTs deposited on alumina substrates by dropcasting (red solid line) and dielectrophoresis (gray dashed line) [66]. Inset: spectral weight in the radial breathing modes (RBM) region.

tain  $d_t \approx 1.5$  nm. The difference in the shape of the G-band reflects a more metallic character of drop-cast SWCNT and a more semiconducting character of SWCNT of the sample prepared by the dielectrophoresis method. This result is in accordance with other studies [69].

The XPS-based elemental analysis of the CNT layer was carried out on a thin film prepared depositing by drop-casting  $1 \mu\text{l}$  of SWCNT solution on a silicon wafer, previously cleaned in an ultrasonic bath. After the solvent evaporation, the XPS analysis was carried out. As expected, the results of XPS (Fig. 3.2) indicate the presence of Na and, to a minor extent, S ascribed to sodium hydroxide and sodium lauryl sulphate in the CNT dispersion. No traces of other contam-

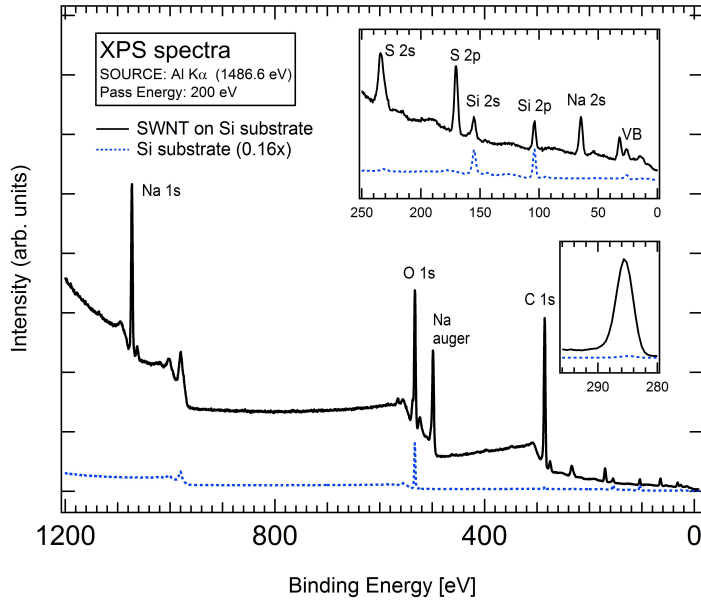


**Figure 3.2:** XPS spectrum of SWCNTs (solid line), dispersed in a solution of water, sodium hydroxide and sodium lauryl sulphate and deposited (1 l) by drop-casting on a silicon substrate. The XPS spectrum of the Si substrate is also reported (dashed line).

inants have been detected within the elemental sensitivity of the XPS probe (about 0.5%). To complete the sample characterization, we wish to mention that, in addition to ammonia, the CGSs were also tested against  $\text{NO}_2$ , acetone and ethyl alcohol exposures. Among these,  $\text{NO}_2$  is a typical interfering gas in the environment, to which the present sensors have been found to be sensitive, with the expected resistivity decrease upon exposure. On the other hand, no sensible response has been recorded to acetone and ethyl alcohol exposures.

### 3.1.3 Sonication effects

After the deposition by drop casting of the solution containing SWCNTs on alumina substrates, the sample was sonicated in ultrasound acetone bath for 45 minutes. Images from scanning electron microscope (SEM) show the

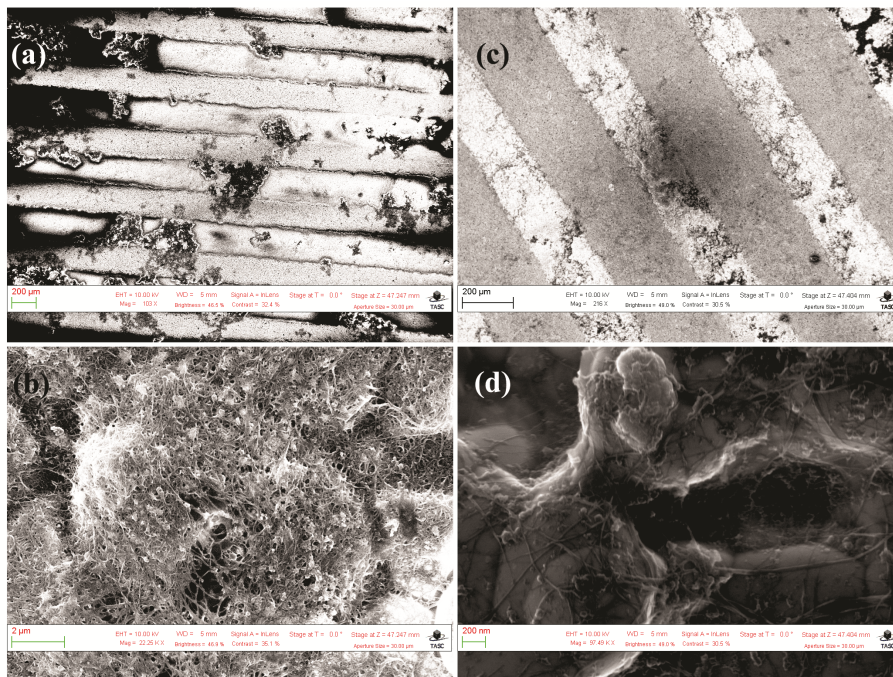


**Figure 3.3:** SEM images of SWCNTs on alumina substrate before (a, b) and after 45 minutes of sonication in ultrasound acetone bath.

morphology of the surface: bundles of SWCNTs are wrapped together between and on the electrodes. In Fig. 3.3, SEM images before and after the sonication treatment are reported. Before the sonication (Figures 3.3 a and b), bundles of SWCNTs that create agglomerates of tenths micrometer length are detectable. After 45 minutes of sonication in acetone, the big amount of amassed SWCNT bundles is sensibly reduced and the surface of the sample appears as shown in Figures 3.3 (c) and (d). In particular, Fig. 3.3 (d) shows the presence of isolated bundles of SWCNT with diameters of 20 nm and length of the order of the micrometer, on the alumina substrate.

In Fig. 3.4 the I-V curves of SWCNT-based chemiresistor gas sensor after 30 and 45 minutes sonication are shown. The trend is linear in the range of voltage explored (0-1.8 V) and the sonication clearly affects the device resistance (inverse

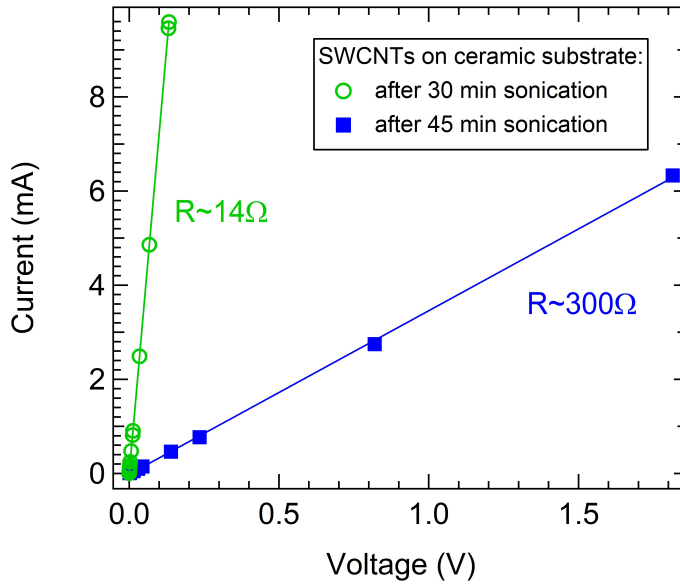


**Figure 3.4:** I-V curve of SWCNT-based chemiresistor gas sensor after 30 minutes (empty green circles) and 45 minutes (filled blue squares) sonication. The linear fit to obtain the resistance value is also shown.

of the slope of the linear fit). The resistance increase is consistent with the lower presence of conducting CNTs on the surface.

In order to analyze the sonication effect on the elemental composition of the sensor surface, we prepared samples with 1  $\mu\text{l}$  of SWCNT solution (deposited by drop-casting on glass substrate with ITO electrodes) and then submitted one of them to sonication process. In Fig. 3.5 XPS spectra of the sample before and after 45 minutes of sonication in acetone ultrasound bath are reported. After 45 minutes of sonication in acetone ultrasound bath, no more traces of S (from the SLS surfactant) are on the surface, however Na (from sodium hydroxide in the solution) is still present. Si peaks, which come from the substrate, are more intense after the sonication process due to the lower covering of glass substrate by CNT film.

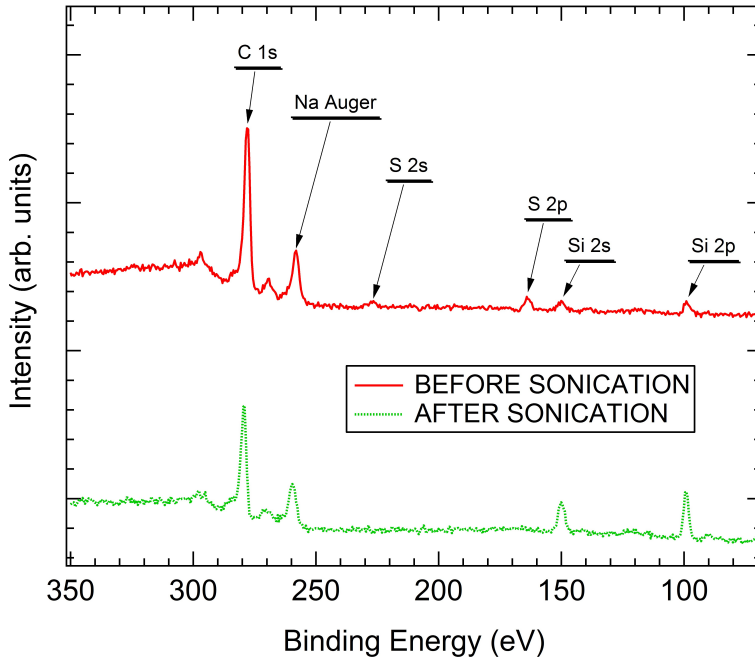


**Figure 3.5:** XPS survey spectra of SWCNTs deposited on glass substrate with ITO electrodes before (red solid curve) and after 45 minutes of sonication in acetone bath (green dotted curve). XPS source: Mg  $K\alpha$ , Pass Energy=100 eV.

## 3.2 Results and discussion

### 3.2.1 Response enhancement

As mention in Section 3.1.1, we explored several strategies in order to enhance the sensitivity of pristine SWCNTs to ammonia gas. They consist in a careful preparation of the sample, starting from a solution of pure water, NaOH, SDS, in which SWCNTs (CarboLex Inc.) are dispersed and depositing it on ceramic substrates with interdigitated Pt electrodes, following two different methods: drop-casting and sonication, dielectrophoresis method. Fig. 3.6 shows the response enhancement of the CNT upon ammonia exposure for sample prepared following the sonication method. After each sonication, the sensor

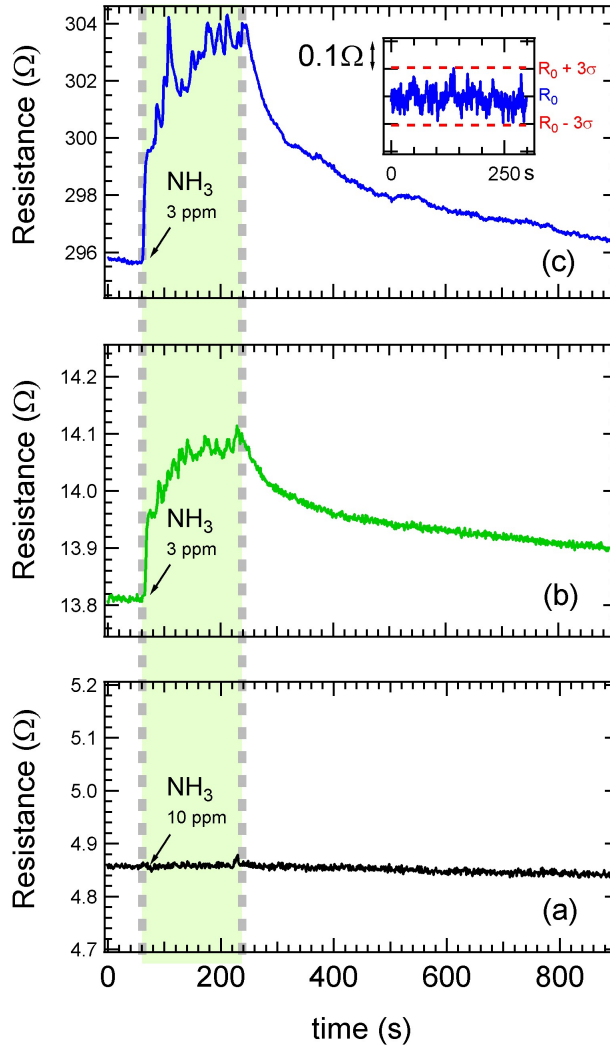


**Figure 3.6:** Response to ammonia gas of the SWCNT-based sensor after different steps of the sonication process: sample not sonicated (a), after 30 min (b), and 45 min (c) sonication in an ultrasound bath.

response to ammonia was tested in the laboratory air and the results are shown in Fig. 3.6 for the film before sonication, and after an overall sonication time of 30 and 45 minutes. The sample not sonicated (Fig. 3.6 a) does not respond to ammonia, despite the high concentration (10 ppm of  $\text{NH}_3$ ). A response to 3 ppm ammonia is detected for the sonicated layers (Fig. 3.6 b and c). Each response is characterized by a steep increase in a short time (risetime) and, when the gas exposure is stopped, by a slower decrease. In order to reproduce realistic working conditions, these measurements have not been carried out in a sealed testing chamber, and therefore signal fluctuations are observed. These fluctuations are different from the noise related to electronics. When the sensors are exposed to ammonia in the testing chamber these fluctuations disappear, and a smoother behavior is detected, as will be discussed later (Fig. 3.10). Instrumental noise fluctuations can indeed be conveniently detected as fluctuations of the baseline signal before any exposure to ammonia (see, e.g., inset of Fig. 3.6). The signal-to-noise ratio (SNR) is defined as  $\Delta R/\sigma$ , where  $\Delta R$  is the maximum resistivity change (measured at the end of the exposure cycle) with respect to  $R_0$ , and  $\sigma$  is the standard deviation of the signal before exposure to ammonia. After 30 min sonication  $\text{SNR} = 91$ , while after the total sonication time (45 min)  $\text{SNR} = 237$ . The sonication also increases the sample resistivity from  $4.86 \Omega$  (before sonication) to  $13.8 \Omega$  (first sonication) and  $296 \Omega$  (second sonication). In the latter case there is a good response to an ammonia exposure of about 3 ppm, with a responsiveness  $\Delta R/R_0 = 3\%$  ( $\Delta R = R_s - R_0$ ). The second method we considered to prepare a thin CNT layer is dielectrophoresis, as described in Section 3.1.1.

Sample	$[\text{NH}_3]$ (ppm)	R ( $\Omega$ )	$\Delta R/R_0$ ( $\times 10^{-3}$ )
DC-S-30	3.0	1.4	22
DC-S-45	3.0	295.6	28
DEP	3.0	363.9	31
DC-S-30	1.5	13.9	16
DC-S-45	1.5	289.3	19
DEP	1.5	360.1	18

**Table 3.1:** Response of three different CNT-based chemiresistors to the exposure to 3.0 and 1.5 ppm ammonia in air. DC-S-30(45): drop cast and sonicated for 30 minutes (45 minutes), DEP: deposited by dielectrophoresis.

In Fig. 3.7 the resistance of two test samples, prepared with the same amount ( $1 \mu\text{l}$ ) of solution containing SWCNTs, is shown. One sample was produced by dielectrophoresis (Fig. 3.7 a) and one by drop casting (Fig. 3.7 b). The values of

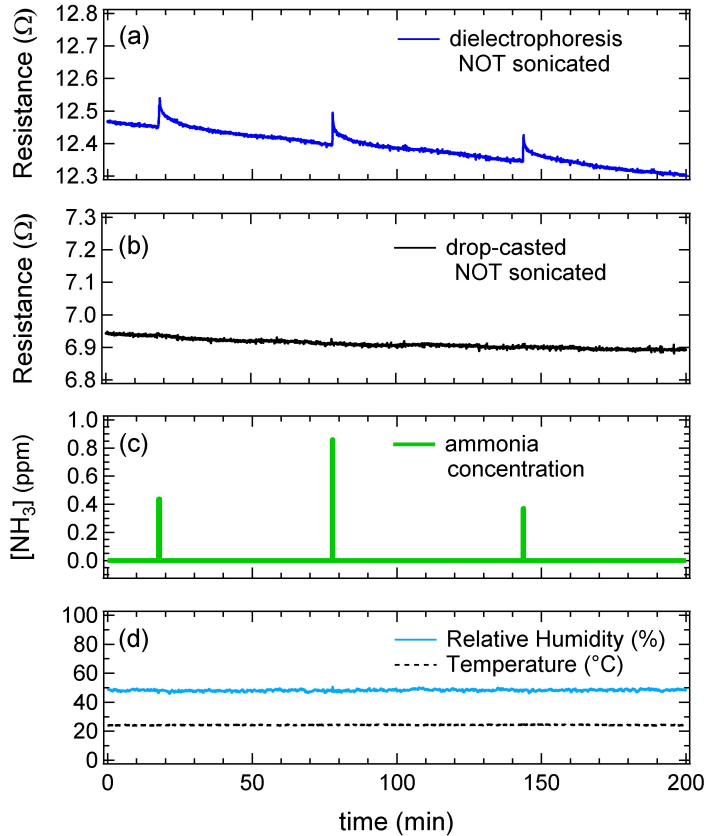


**Figure 3.7:** Response to sub-ppm ammonia concentrations of two samples, one produced by dielectrophoresis (a) and one by drop casting (b). Ammonia concentration (c), relative humidity (%), and temperature ( $^{\circ}\text{C}$ ) during the exposures (d).

ammonia concentrations (Fig. 3.7 c), the relative humidity (RH) and the temperature (Fig. 3.7 d) are also shown. The sample prepared by dielectrophoresis shows a sensible resistance variation when exposed to  $\text{NH}_3$ , while the sample



prepared by drop-casting and not sonicated does not respond to ammonia gas, as observed in the case of an exposure of 10 ppm (Fig. 3.6 a). In order to compare the response of this kind of sample with that prepared by drop-casting and sonication, another sample has been prepared by dielectrophoresis method, which has  $R \approx 360 \Omega$  (almost the same resistance of the drop-casted and sonicated sample). In Table 3.1, the device responses to 3 ppm and 1.5 ppm  $[\text{NH}_3]$  for the sample prepared by dielectrophoresis (DEP) and that prepared by drop-casting and sonication (DC-S) are compared. These results show that the device response is similar in the two cases. Regarding the morphology, SEM images (Fig. 3.8 a and 3.8b) indicate that the CNTs are more uniformly distributed

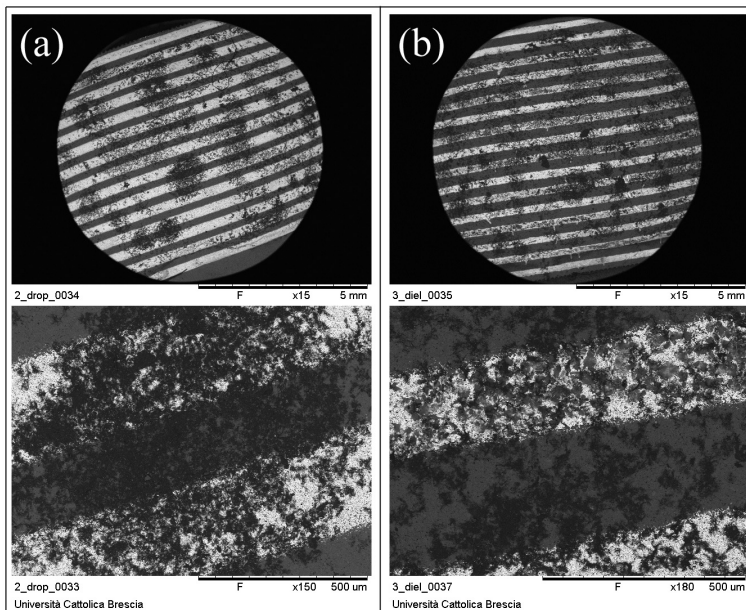


**Figure 3.8:** Top panel: SEM images of the samples prepared by drop casting (a) and by dielectrophoresis (b). Bottom panels: magnified views of selected areas. The bright stripes are the uncovered  $\text{Al}_2\text{O}_3$  regions, and the dark stripes are the Pt electrode fingers.

in the sample prepared by dielectrophoresis. These results are consistent with those presented in other studies, which report that the dielectrophoresis method allows SWCNTs to be more ordered (aligned) and to show a better sensitivity

with respect to disordered SWCNTs, ascribing this fact to the enhancement of the surface area accessible to the ammonia molecules [70], [71]. The dielectrophoresis method allows us to obtain a sample sensitive to ammonia, without resorting to the less reproducible sonication process. However, the  $R_0$  value is similar for both samples and the sensitivities of the two samples to the same analyte concentration are comparable. Both methods have the final goal of making the CNT bundle distribution more uniform. In the case of sonication, fragments of bundles loosely attached to the substrate are likely to detach, leaving on the sample only the fragments with a firm contact and therefore allowing better draining of the injected carriers through the electrodes. This can explain the lack of response observed in the sample prepared by drop-casting and not sonicated where the great amount of agglomerated bundles (Fig. 3.3 b) hinder the injected charge to easily reach electrical metal contacts. The dielectrophoresis method has shown to yield more uniformly distributed bundles (Fig. 3.8), avoiding the formation of too large, loosely bound, aggregates during the deposition stage.

### 3.2.2 Detection Limit (DL)

So far, in literature ppt sensitivity towards  $\text{NH}_3$  has been demonstrated in an inert atmosphere under UV irradiation [24]. As for the sub-ppm detection limit, a detection of 50 ppb ammonia diluted in Ar has been reported for CNTs functionalized with polyaniline [72], while a DL = 200 ppb for ammonia in dry air was achieved with Pt-decorated CNTs operating at 200°C [73]. The present study was carried out in the lab environment, i.e. not inside a testing chamber, which is much closer to the final destination of the CNTs sensors. In Fig. 3.9 (a) and 3.9 (c), sequences of ammonia exposures of the SWCNT-based CGS are reported. During the exposures to ammonia, the relative humidity (R.H.) and the temperature were also monitored for both series (data reported in Fig. 3.9 (b) and (d), respectively). On the basis of the data collected upon exposure to ammonia at different concentrations, such as those presented in Fig. 3.9, the response curve has been drawn in Fig. 3.9 (right panel), where the response  $\Delta R/R_0$  is plotted vs. ammonia concentration. We resorted to use the data for the drop-cast samples as a larger data set was available for these devices. Several points fall below the 1 ppm threshold, i.e. the calibration range of the

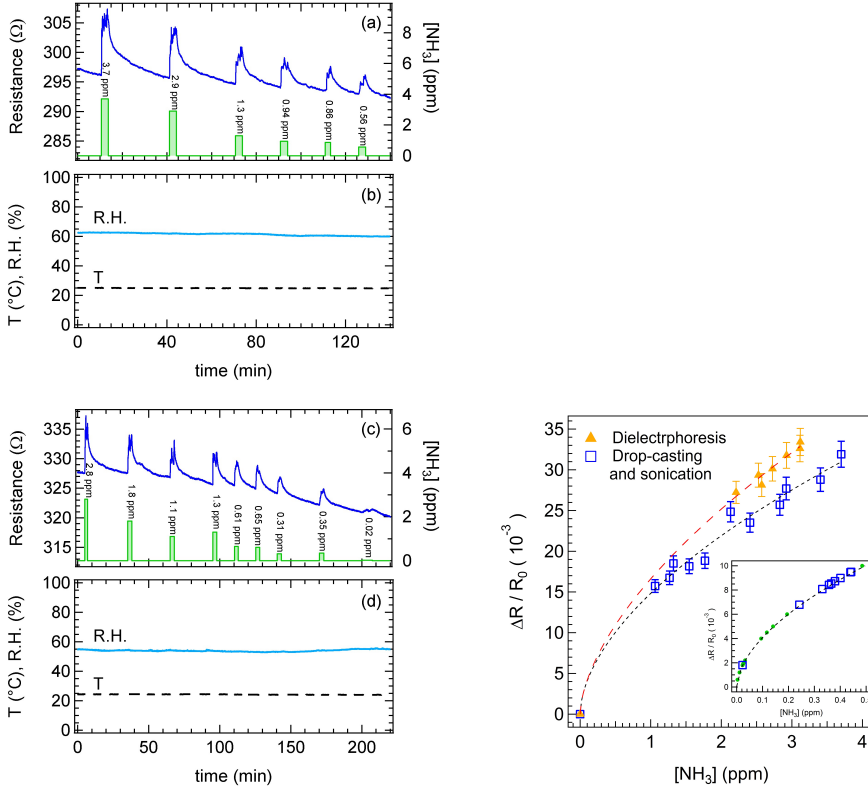


**Figure 3.9:** LEFT PANELS: (a and c) two series of responses collected by the SWCNT drop-casted and sonicated sensor to different ammonia concentrations  $[\text{NH}_3]$ . (b and d) Relative humidity and temperature during the exposures. RIGHT PANEL: response curve for the SWCNT drop-casted and sonicated (blue empty squares) and dielectrophoresis (yellow filled triangles) sensors. Inset: set of measurements in the sub-ppm range for the SWCNT drop-casted and sonicated sensor (blue empty squares are sub-ppb measurements, the green dots are fluctuation jumps).

Figaro 2602 CGS. In order to obtain the concentration values for these sub-ppm measures (19 values in the sub-ppm range), a fit of the data above 1 ppm (11 points above 1 ppm), plus the (0, 0) point, has been carried out by using a power function ( $y = A x^p$ ), following Ref. [74] and considering Freundlich adsorption

isotherm (see Appendix B). The fit parameters are:  $A = (15 \pm 1) \times 10^{-3}$  and  $p = 0.56 \pm 0.05$ . Therefore the equation relating the ammonia concentration to the sensor response is:  $\Delta R/R_0 = 0.015([\text{NH}_3])^{0.56}$ , where  $[\text{NH}_3]$  is expressed in ppm units. With this fit, we can evaluate the concentration of the points below the ppm level (inset of Fig. 3.9, right panel), down to the lowest exposure limit of 20 ppb (last ammonia exposure in Fig. 3.9 c) and other small resistance variations.

By considering the noise value and the response curve fit parameters we can obtain the detection limit (DL) that we define as the lowest analyte concentration value detectable, corresponding to a  $5\sigma$  noise fluctuation, a more restrictive condition than that proposed in Ref. [24], where a  $3\sigma$  noise level was considered. Indeed, according to the equation:  $(5\sigma/R_0) = 0.015(\text{DL})^{0.56}$ , by assuming a typical fluctuation  $\sigma = 0.035 \Omega$  (inset of Fig. 3.6) and an average resistance  $R_0 = 300 \Omega$ , the detection limit is 3 ppb. A similar approach was also applied to the sample prepared by dielectrophoresis, though to a smaller data set with respect to the DC samples. The following parameters were obtained:  $A = (17 \pm 1) \times 10^{-3}$  and  $p = 0.60 \pm 0.07$ . The data of fit parameters,  $\sigma$  and  $R_0$  values of the two samples are compared in Table 3.2. For both samples a detection limit of 3 ppb is achieved. Having verified that the sensor responds to

Sample	$R_0$ ( $\Omega$ )	$\sigma$ ( $\Omega$ )	$A$ ( $\times 10^{-3}$ )	$p$	DL (ppb)
DC-S	300	0.035	$15 \pm 1$	$0.56 \pm 0.05$	3
DEP	360	0.035	$17 \pm 1$	$0.60 \pm 0.07$	3

**Table 3.2:** Baseline resistance ( $R_0$ ), noise level, fitting parameters  $A$  and  $p$  of the response curve and detection limits (DL) of the samples prepared by drop-casting and dielectrophoresis.

very low concentrations of ammonia (red crosses in the inset of Fig. 3.9, right panel), we can interpret the small fluctuations of the signal during the gas exposure as responses to very tiny changes in concentration. Additional points in the sub-ppm range have accordingly been added to the inset of Fig. 3.9, right panel (green dots). As already observed in Fig. 3.6, sharp signal fluctuations are detectable on top of the response curves. These fluctuations can be noticed also in the data shown in Fig. 3.9 (a) and (c) and ascribed to turbulences in the environment around the sensor. By comparing the sensor response to ammonia gas in the testing chamber and in laboratory air, we observed that the fluctu-

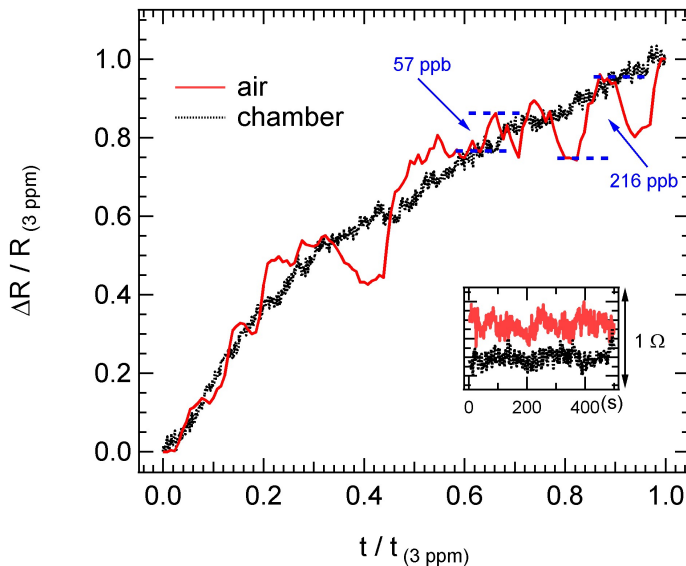


**Figure 3.10:** CNT response to 3 ppm ammonia in air and in the testing chamber. Inset: noise level before ammonia exposure.

ations during the exposure disappear when the measurement is carried out in a sealed testing gas chamber (Fig. 3.10 and Fig. 3.11). In Fig. 3.10 the signal changes upon exposure to 3 ppm ammonia in a sealed chamber and in air are compared. For both measurements, the time scale has been normalized to the time ( $t_{3ppm}$ ) when the 3 ppm  $[\text{NH}_3]$  was reached, as the sealed chamber (about 1 liter volume) required a much longer time to reach the 3 ppm concentration value. In Fig. 3.11 a comparison of sensor response to 8 ppm ammonia gas in air lab and in gas testing chamber for a SWCNT-based sensor on plastic substrate is shown (the response of this kind of samples on plastic substrate is discussed in chapter 4). In principle one can not exclude that the signal variation on top of the curve during gas exposure are due to relative humidity effects (R.H.  $\approx$  40-60% during measures in air, while in the testing chamber R.H.  $\approx$  10%), but other test measurements (not shown here) performed in the testing chamber at different R.H. values do not show these fluctuations. Therefore, if the measurements

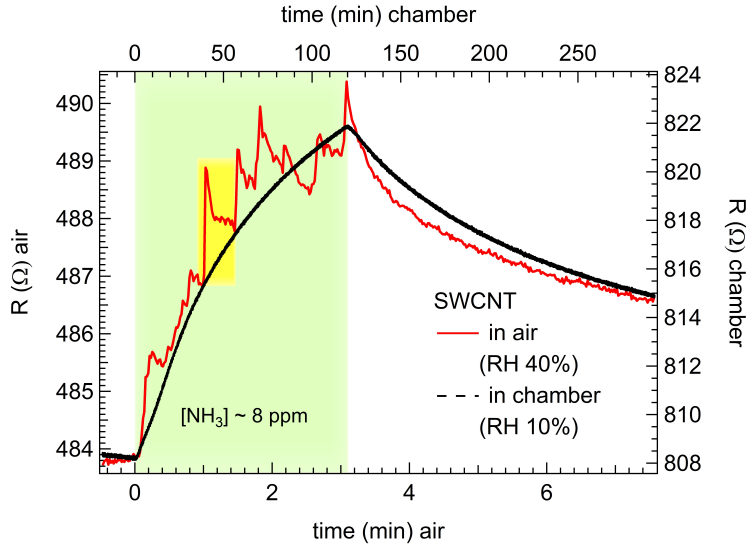


**Figure 3.11:** Comparison of sensor response to ammonia gas ( $[\text{NH}_3] \approx 8 \text{ ppm}$ ) in air lab and in gas testing chamber for a SWCNT-based sensor on plastic substrate [75].

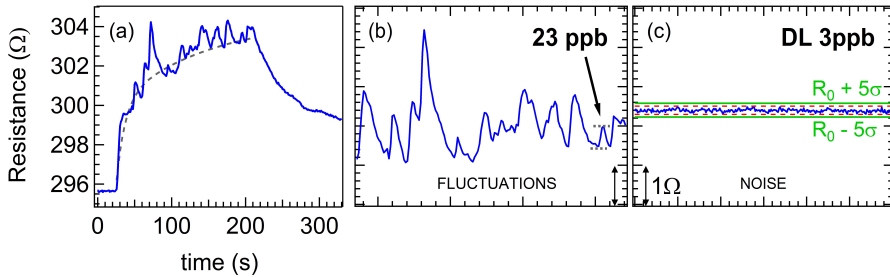


**Figure 3.12:** Example of response of SWCNT based gas sensor (a) and fluctuations over the top of the curve (b), compared with noise (c).

are carried out in air, turbulences of the local environment can produce on the top of the leading curve during gas exposure resistance fluctuations much larger than the electrical noise (Fig. 3.12). The typical resistivity variations  $\Delta R$  for the

fluctuations of the CNT signal correspond to concentrations in the 15-150 ppb range, matching the lowest value here detected upon ammonia exposure (20 ppb, last point of Fig. 3.9 c). As an example, in Fig. 3.10 and in Fig. 3.12 (b) the ammonia concentration values (57 ppb, 216 ppb and 23 ppb) related to signal fluctuations are also indicated.

We believe that these fluctuations correspond to tiny  $[\text{NH}_3]$  variations not only because they are larger than the noise signal (as shown in Fig. 3.12), but also because we recorded the same fluctuation shapes (Fig. 3.13) in the signal of two different samples both based on SWCNTs (one prepared as described in 3.2.1

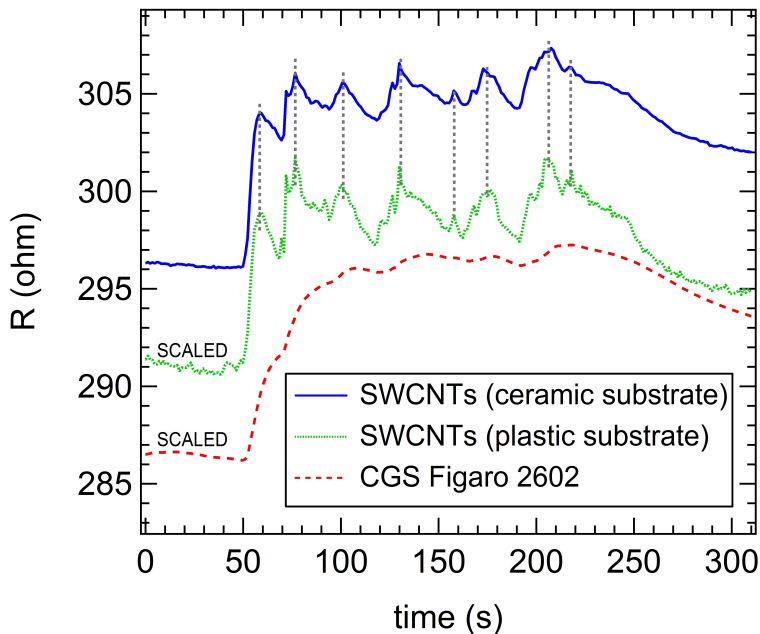


**Figure 3.13:** Response to an overall ammonia concentration of 3.7 ppm in air of SWCNTs prepared by drop casting and sonication on ceramic substrate (blue solid line), SWCNTs on plastic substrates (green dotted line) and commercial CGS Figaro 2602 (red dashed line) based on metal oxide  $\text{SnO}_2$ . “Same shape fluctuations” are observed on top of the curve signal of gas sensors based on SWCNTs, ascribed to very tiny change in the  $\text{NH}_3$  concentration. The measure was done at room temperature ( $T = 25^\circ\text{C}$ ) and the R.H. = 65%.

with drop casting and sonication on ceramic substrate with Pt interdigitated electrodes, and the other on prepared by drop casting the solution containing SWCNTs on plastic substrate with two Ag paste stripes as electrodes, as we discuss in next chapter).

### 3.2.3 Response time scales

Further evidence that the signal fluctuations can be regarded as a distinctive behaviour of the response of ultrathin CNT layers to gas adsorption is provided in Fig. 3.14 (left panel) where the responses of the CNT and of the commercial metal oxide CGS Figaro2602 sensor upon exposure to 3.7 and 2.9 ppm of ammonia are compared. In the right panel of Fig. 3.14, the comparison is shown again to highlight the difference also in the rise time, where the SWCNT-based gas sensor exhibit a faster response time. Fitting the signal during the rise time, i.e. from the beginning of the response until the end of the gas exposure, the Figaro2602 rise time signal is better fit by a single exponential (with a decay time  $\tau \approx 60.2 \pm 1.8$  s), while the SWCNT signal is best fit by a double exponential curve (with decay times  $\tau_1 \approx 3 \pm 1$  s and  $\tau_2 \approx 55 \pm 7$  s). The Figaro2602, used as reference sensor during the measurements, shows a much smoother behaviour in the regions where the CNT response displays fluctuations. In order to prove that the response fluctuations are an intrinsic feature of CNTs, the CNT response curve  $R_{CNT}(t)$  has been convoluted with a function  $F(t) = t \exp(-t/\tau_F)$ , which introduces an additional channel, with a  $\tau_F$  decay time, to the metal oxide response. As can be observed in Fig. 3.14 (dashed line), the convoluted spectrum  $R_{CNT}(t) \otimes F(t)$  reproduces the behavior of the metal oxide gas sensor quite well. This shows that the metal oxide response introduces a component that increases the overall decay time with respect to CNTs. This component is absent in CNTs and makes sharp concentration fluctuations well resolved and detectable. We ascribe the effect introduced through the  $F(t)$  to the different charge carrier path to the electrodes in the two cases. While for CNTs the charge transfer to the electrodes is allowed by the thin CNT layer, suitably treated using either sonication or dielectrophoresis methods, in the metal oxide sensor the inter-grain charge transfer before reaching the electrodes may alter the response time, introducing capacitive effects at the grain border. The signal fluctuations observed in the CNT response to ammonia exposure are



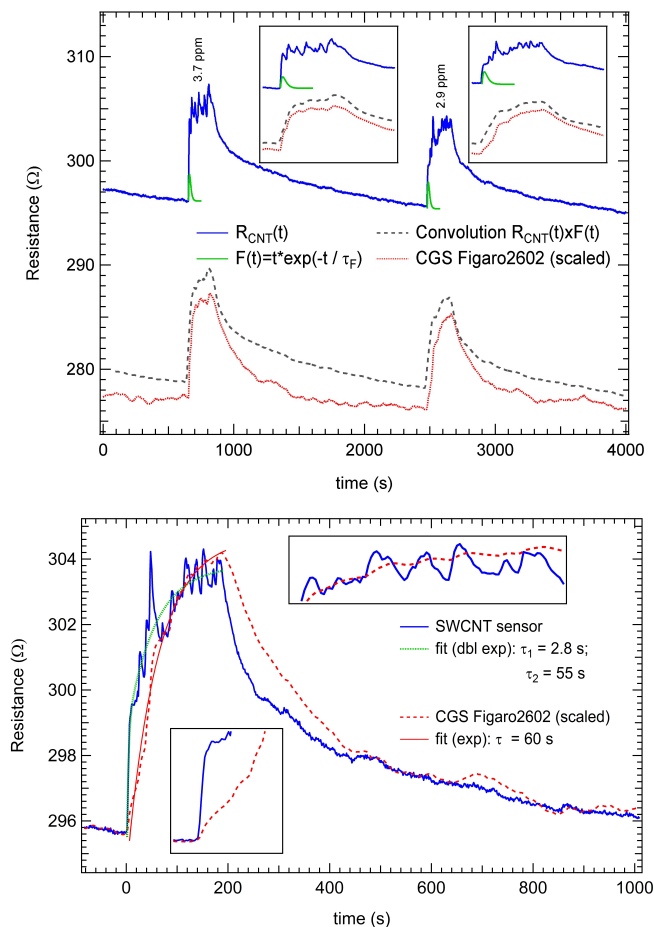


**Figure 3.14:** Comparison of response to ammonia gas of SWCNT and commercial metal oxide CGS Figaro2602. LEFT PANEL: resistance of the SWCNT based sensor (blue line); decay function  $F(t) = t \exp(-t/\tau_F)$ ;  $\tau_F = 7$  s (green); convolution of the signal of the SWCNT with  $F(t)$  (grey dashed line); resistance of the Figaro2602 sensor (red line). RIGHT PANEL: resistance of the SWCNT based sensor (blue line) and Figaro2602 sensor (red dashed line); fit of the signal during the rise time of the two sensors (green dashed line for SWCNT and solid red line for Figaro2602).

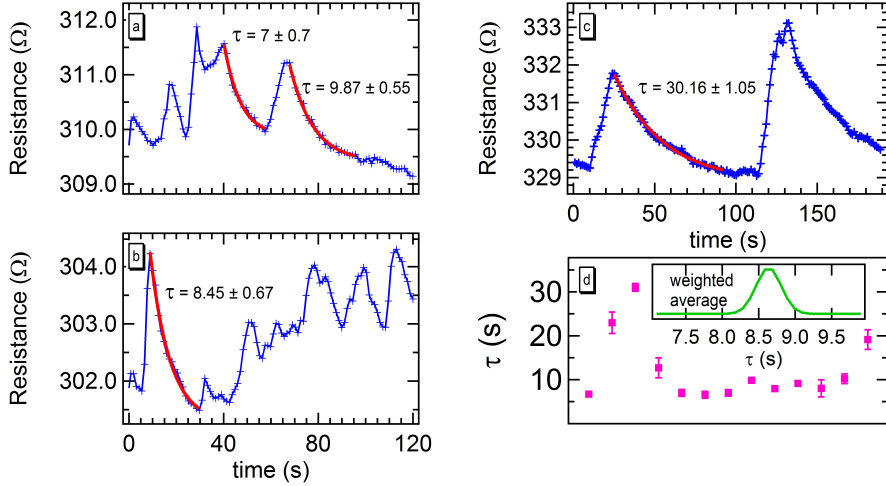


**Figure 3.15:** (a,b,c) Examples of fitting with exponential curve to obtain the decay time of signal fluctuations on top of the curve during gas exposure. (d) Decay time values and weighted average (inset).

ascribed to a fast recovery time allowing for the detection of small concentrations in the ppb range. These signal fluctuations on top of the curve during gas exposure also have their own characteristic time for signal rise and decay. By picking up several of these fluctuations we have estimated the average decay time by exponential fitting (some of these fittings is shown in Fig. 3.15) which resulted to be  $\tau_1 = 8.55 \pm 0.17$  seconds.

### 3.2.4 Convolution and signal shaping

The information related to the fast decay time of the small fluctuations, allowed us to model the response of the SWCNT sensor. In first approximation, we can model the constant analyte exposure as a rectangular function ( $C_{NH_3}(t)$ , green dashed line in Fig. 3.16) equal to the ammonia concentration value for the time of exposure, and otherwise equal to zero. The SWCNT response is modeled with a multi-exponential function (as common to find in literature [76, 77]) as

$$CNT(t) = CNT_f(t) + CNT_s(t) \quad (3.1)$$

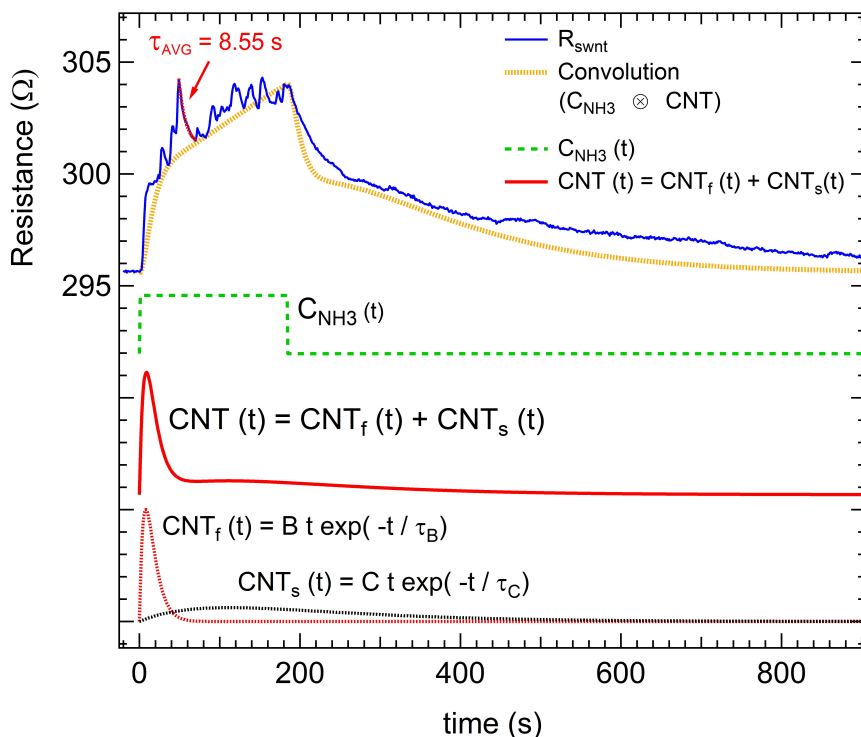


**Figure 3.16:** Modeling of the CNT sensor response, seen as the convolution of a rectangular function  $C_{NH_3}(t)$ , which describe the constant analyte concentration, and an exponential-like function  $CNT(t)$ , sum of two parts: the first part  $CNT_f(t)$  accounts for a quick decay of the signal, while the second part  $CNT_s(t)$  is added to account for much slower decay processes (see Eq. 3.2 and 3.3). The parameter values are:  $B = 17$ ,  $C = 0.15$ ,  $\tau_B = 8.55$  s,  $\tau_C = 112$  s.

where

$$CNT_f(t) = B \cdot t \cdot e^{(-t/\tau_B)} \quad (3.2)$$

and

$$CNT_s(t) = C \cdot t \cdot e^{(-t/\tau_C)} \quad (3.3)$$

$CNT_f(t)$  accounts for a fast decay of the signal ( $\tau_B$ , set to 8.55 s as the average decay time we found from the analysis of signal fluctuations), while the second

part,  $CNT_s(t)$ , is added to account for much slower decay processes, and aims to model the slow recovery of the signal after gas exposure at room temperature. Through a convolution of this function with the rectangular function  $C_{NH_3}(t)$ , the overall features of the CNT response have been reproduced, as shown in Fig. 3.16, where the thick yellow line is the result of the convolution  $C_{NH_3}(t) \otimes CNT(t)$ . The convolution of two signals is formally written as

$$\int C_{NH_3}(\tau) \cdot CNT(t - \tau) d\tau \quad (3.4)$$

and it takes into account a delay time between the gas concentration signal and the response of the sensor. This curve well approximates the rising of the signal over the exposure time and the slow decay to recover the initial resistance  $R_0$ . Deviations with respect to the initial  $R_0$  value can be ascribed to slow desorption processes, which are related either to chemisorptions or trapping of the molecules within the CNT bundles. Indeed, the presence of an apparently irreversible behavior in the response of the CNT to gas exposure has been discussed in detail by Lee and Strano [78]. Based on the present results as well as on the discussion proposed in the literature, we rationalize our findings as follows. Upon exposure to a polluting gas (here ammonia) the leading edge of the signal is provided by a convolution of a fast-response with the concentration profile. The fast response time is extracted from the signal fluctuations that are detected on top of a monotonically rising signal. An additional slow-response contribution is also present and detectable during the signal attenuation. The difference between the fast and the slow signal could be ascribed to different paths of the injected charge from the CNT surface to the electrodes, the fast signal being related to the CNT contacting the electrodes, and the slow signal to transport in bundled CNTs before reaching the electrode. A signature of irreversible interactions, on the time scale of the present measurements, is finally ascribed to the partial recovery of the overall signal on a typical time scale of  $10^3$  s.

In order to support our analysis on response time-scale and convolution fit of the signal, we consider the response to a very short “pulse” of  $NH_3$  diluted in  $N_2$  (nominally  $[NH_3] = 1.2$  ppm). This signal is well fit by a convolution, as we did for the response reported in Fig. 3.16, of a rectangular function  $C_{NH_3}$  (which represents the short ammonia “pulse”, with duration of 4 seconds, equal to the ammonia concentration, i.e. 1.2 ppm, during the time of exposure and zero otherwise) and by a double-exponential like function (Eq. 3.1-3.3) using

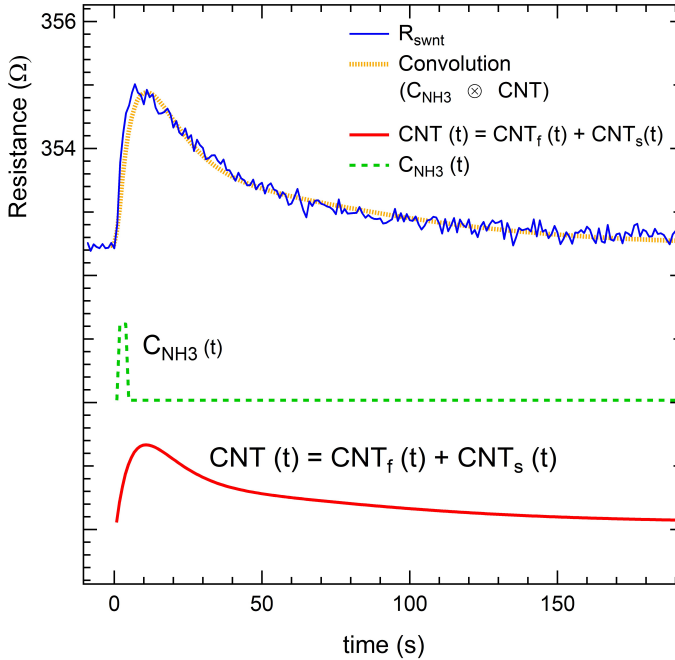


**Figure 3.17:** Response to a 4 s short “pulse” of ammonia gas exposure in  $N_2$  inert atmosphere ( $[NH_3] = 1.2$  ppm). The response is modeled by the convolution of a rectangular function  $C_{NH_3}(t)$ , which describe the constant analyte concentration, and an exponential-like function  $CNT(t) = CNT_f(t) + CNT_s(t)$ , following Eq. 3.2 and 3.3. The parameter values are:  $B = 3.2$ ,  $C = 0.3$ ,  $\tau_B = 8.55$  s,  $\tau_C = 38$  s.

the following parameters:  $B = 3.2$ ,  $C = 0.3$ ,  $\tau_B = 8.55$  s (fixed from the results of Fig. 3.15),  $\tau_C = 38$ s. The convolution is reported in Fig. 3.17.

### 3.3 Conclusions

The detection of low-ppb concentrations with films of SWCNTs at room temperature, obtained by dispersed nanotubes in aqueous solution with a surfactant, without any functionalization is a remarkable forward step in the exploration of detection limits of CNT-based sensors. To the best of our knowledge, the present

results represent the lowest ammonia concentration so far attained in air with pristine CNTs. This also shows that, starting from samples prepared according to the procedures described in this study, lower detection limits can be expected by further doping or functionalization of the CNTs. This result was obtained on SWCNT bundle layers carefully prepared and selected by dielectrophoresis-assisted deposition or by sonication of layers deposited by drop casting. We ascribe the enhanced sensitivity to the removal of loose agglomerates with poor electrical contacts and to more efficient transport of carriers, transferred to the CNT bundles upon interaction with the reducing  $\text{NH}_3$  molecules, from the top-most SWCNTs to the underlying electrodes. These facts allowed us to track the fast dynamics processes, otherwise missed in conventional oxide-based nanostructured gas sensors, where the grain boundaries between nanoparticles are thought to introduce a capacitive component in the response that can average out the response to quick transients of the analyte concentration. In perspective, this result makes the CNT-based CGS quite interesting to produce low cost, high sensitivity, chemiresistor gas sensors for environmental monitoring of sub-ppm ammonia concentrations. Finally, by revealing a fast dynamics channel, so far virtually neglected, in the gas desorption process, we have been able to model the sensor response by a convolution of a rectangular function which describe the constant analyte concentration, and an exponential-like function which is related to the real response of the gas sensor.

## Chapter 4

# Effects of the functionalization with metal oxide nanoparticles

In the last 60 years, a large body of studies on semiconducting metal oxide (SMOX) materials as gas sensors has been carried out, recently also at nano-scale dimensions. In the last years hybrid materials composed of nano-SMOX and SWCNTs have begun to attract interest of many researchers [79–85]. In fact, further possibilities to improve the SWCNT-based gas sensor performances are expected from SWCNT-oxide hybrid systems, in particular from the blend of CNT with nanoparticle metal oxides such as  $\text{TiO}_2$ ,  $\text{SnO}_2$ ,  $\text{WO}_3$ , indium-tin oxide (ITO). In this chapter we present low-cost gas sensors based on SWCNT layers prepared on plastic substrates and operating at room temperature, displaying a high sensitivity to  $[\text{NH}_3]$ . The use of cheap flexible plastic substrates discloses possible production for ink-jet printing process, or application in flexible integrated circuits. Once combined with the low noise, the high sensitivity allowed us to reach an ammonia detection limit of 13 ppb, which matches the requirements for ammonia monitoring in the environment. Furthermore, a blend of SWCNT bundle layers with metal oxide nanoparticles, e.g. indium-tin oxide (ITO) or titanium dioxide  $\text{TiO}_2$  nanoparticles, resulted in an increased sensi-

tivity with respect to pristine CNT. Finally, the response of the ITO-SWCNT sensor to water vapor and nitrogen dioxide provides a way to tailor the sensor selectivity with respect to two of most relevant interfering gases expected in outdoor environmental monitoring. We propose a gas sensing model to explain this peculiar response.

## 4.1 SWCNT and hybrid layers on plastic substrates

### 4.1.1 Sample preparation and functionalization

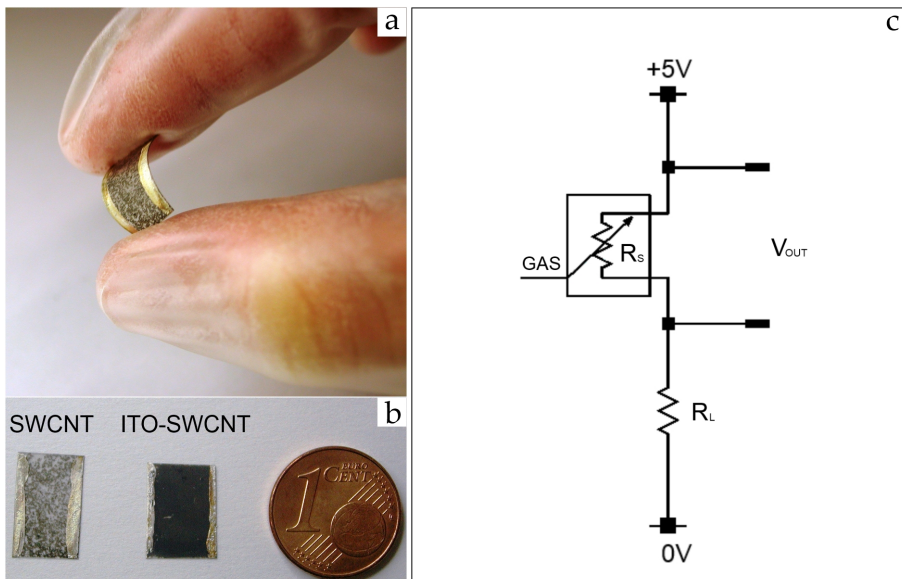


**Figure 4.1:** (a and b) Chemiresistor gas sensors (CGS) based on single-wall carbon nanotubes onto a flexible plastic substrate. (c) Scheme of the circuit for the electrical measurements: a constant voltage  $V_C = 5$  V is applied across the CGS, connected in series with a load resistor  $R_L = 33$  k $\Omega$ . By monitoring the voltage  $V_{out}$  across the sensor, its resistance is measured [86].

The samples on plastic substrates, which we analyze in this chapter, were



prepared at the micro-nano-carbon-lab of Elettra (TS) by A. Goldoni. Plastic substrates were chosen in view of possible device development with printable electronics methods [61,62]. The pristine sample (SWCNT) was prepared starting from a SWCNTs dispersed in a solution containing water, sodium hydroxide and sodium lauryl sulfate (CarboLex Inc.) and deposited by drop casting onto a plastic substrate. The functionalized sample (ITO-SWCNT) was prepared by adding 5% wt Indium Tin Oxide nanoparticles (average diameter  $< 50$  nm, purity grade 99.99%, IoLiTec GmbH) to the CNT dispersion prior to the deposition on the plastic substrate. The SWCNT + ITO nanoparticles mixture was sonicated for 1 h and then deposited on the flexible plastic substrate. In both cases, the sample is a rectangle with a sensitive area of about  $75 \text{ mm}^2$ . Two strips of Ag paste were deposited on the sides of the sample as contacts with the electronic circuit. Images of these two samples and of the electrical measurement circuit are shown in Fig. 4.1. A third sample ( $\text{TiO}_2$ -SWCNT) was prepared with SWCNT +  $\text{TiO}_2$  nanoparticles (average diameter  $< 100$  nm) following a similar procedure as in the case of ITO-SWCNT sample.

### 4.1.2 Layer characterization

The structural properties of the SWCNT layers have been characterized by Raman spectroscopy. The Raman spectra (Fig. 4.2 and Fig. 4.3) show the characteristic SWCNT peaks [30]: the G-band (with the  $G^-$  and  $G^+$  contributions, at  $1578 \text{ cm}^{-1}$  and  $1600 \text{ cm}^{-1}$  respectively), the D-band at  $1330 \text{ cm}^{-1}$  and the  $G_0$ -band at  $2640 \text{ cm}^{-1}$ . The radial breathing modes lines are found around  $180 \text{ cm}^{-1}$ , indicating the presence of SWCNTs. A precise assignment of multiple RBM frequencies is out of the scope of this thesis, but we can roughly estimate the diameter of the nanotubes, around  $1.4 \text{ nm}$  (using equation and parameters proposed for SWCNT bundle [68]). The Raman spectra for SWCNT and ITO-SWCNT samples taken at different points on the sample surface are quite homogeneous, while in the case of  $\text{TiO}_2$ -SWCNT sample the surface appears quite inhomogeneous (Fig. 4.3).

As expected, in addition to carbon from the CNT, the results of the XPS analysis indicate the presence of Na and, to a minor extent, S ascribed to surfactants (sodium hydroxide and sodium lauryl sulfate) in the CNT dispersion. Except for small traces of Si, no other contaminants have been detected within the el-

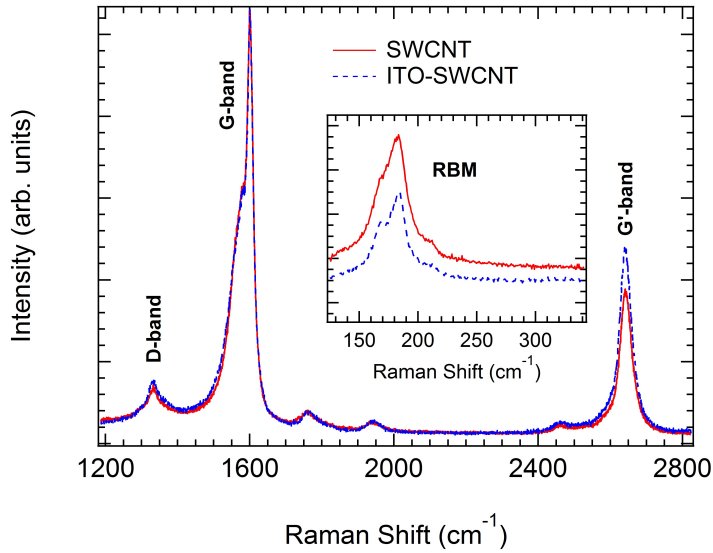


**Figure 4.2:** Raman spectra of the ITO-SWCNT blend (blue dashed line) and pristine SWCNTs (red solid line). The spectra have been normalized to the maximum of the G-band peak [86].

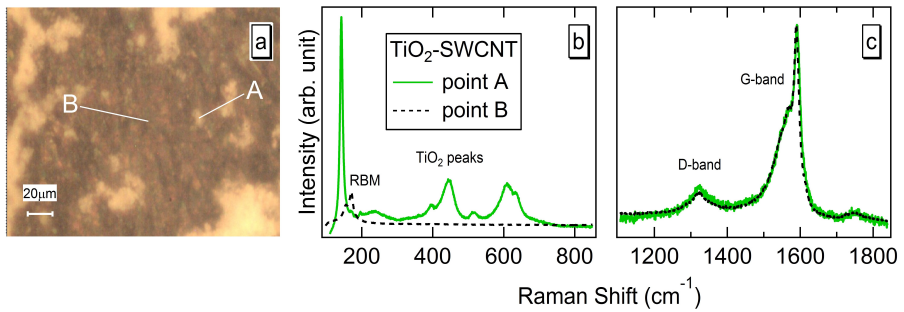


**Figure 4.3:** (a) Microscope 20× image of the  $\text{TiO}_2$ -SWCNT sample. (b) Low frequency region and (c) high frequency region Raman spectra of the  $\text{TiO}_2$ -SWCNT sample taken at two different points (A and B) shown in the microscope image.

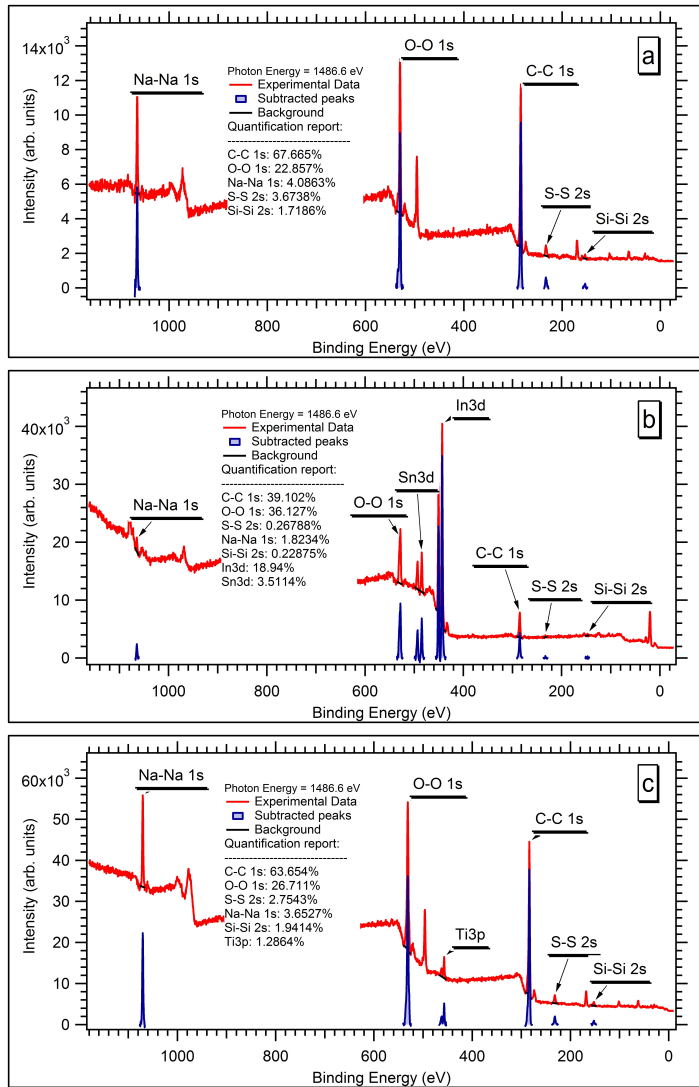


**Figure 4.4:** XPS spectra of (a) SWCNT, (b) ITO-SWCNT and (c) TiO<sub>2</sub>-SWCNT sample. The quantification analysis was carried out with the BRIXIAS package [87].

emental sensitivity of the XPS probe (about 0.5%). By taking the area under the XPS peaks, we can estimate the amount of each element on the sample's surface. The quantification analysis was carried out with the BRIXIAS package [87] and the results are shown in Fig. 4.4. The AFM images of the sample

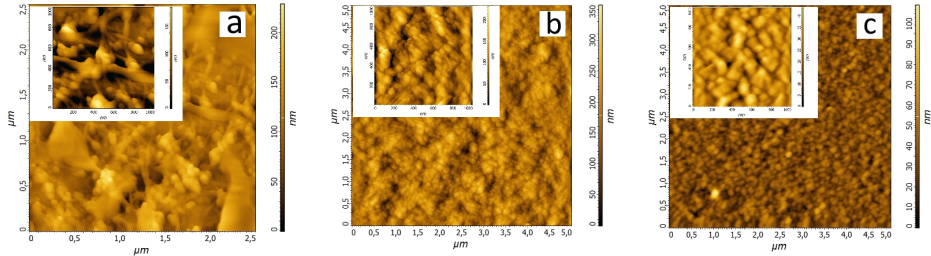


**Figure 4.5:** AFM images of (a) SWCNT, (b) ITO-SWCNT and (c) TiO<sub>2</sub>-SWCNT sample on plastic substrates.

surfaces are shown in Fig. 4.5, where scans over a  $2.5 \times 2.5 \mu\text{m}^2$  (SWCNT) or  $5 \times 5 \mu\text{m}^2$  (ITO-SWCNT, TiO<sub>2</sub>-SWCNT) areas are reported. The inset shows an enlarged view ( $1 \times 1 \mu\text{m}^2$ ) of the three samples surfaces. As can be observed, bundles of SWCNTs with diameter ranging from 30 nm to 70 nm are detectable for the pristine layer, while in those functionalized with the oxide nanoparticles

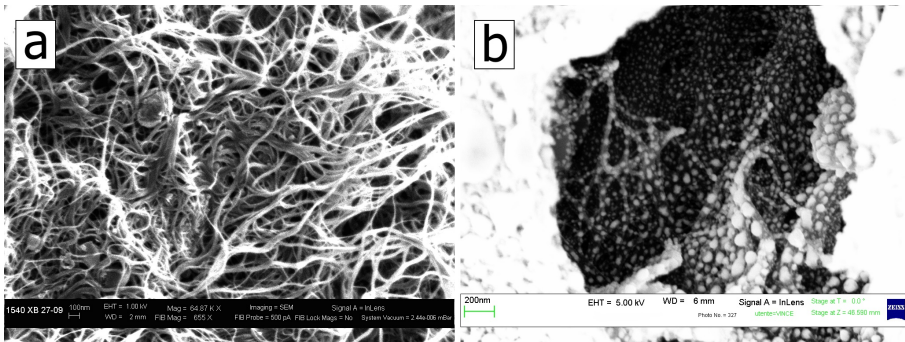


**Figure 4.6:** SEM images of (a) the pristine SWCNT and (b) functionalized ITO-SWCNT(b) samples on plastic substrates.

the bundled structure seems to disappear due to the filling of voids by the oxide

nanoparticles. SEM images confirm AFM images. In Fig. 4.6 (a) we observe several  $\mu\text{m}$  long SWCNT bundles with diameter from about 30 to 70 nm. In Fig. 4.6 (b) ITO nanoparticles with dimensions of 50 to 100 nm anchored to the SWCNT bundles can be detected.

In Fig. 4.7 the I-V curves of SWCNT-based chemiresistor gas sensors on plastic substrates are shown. The trend is linear in the range of voltage explored (from -1 V to 1 V) and from the inverse of the slope we obtain the resistance value for each sample. I-V curves shown in Fig. 4.7 has been taken on samples of the

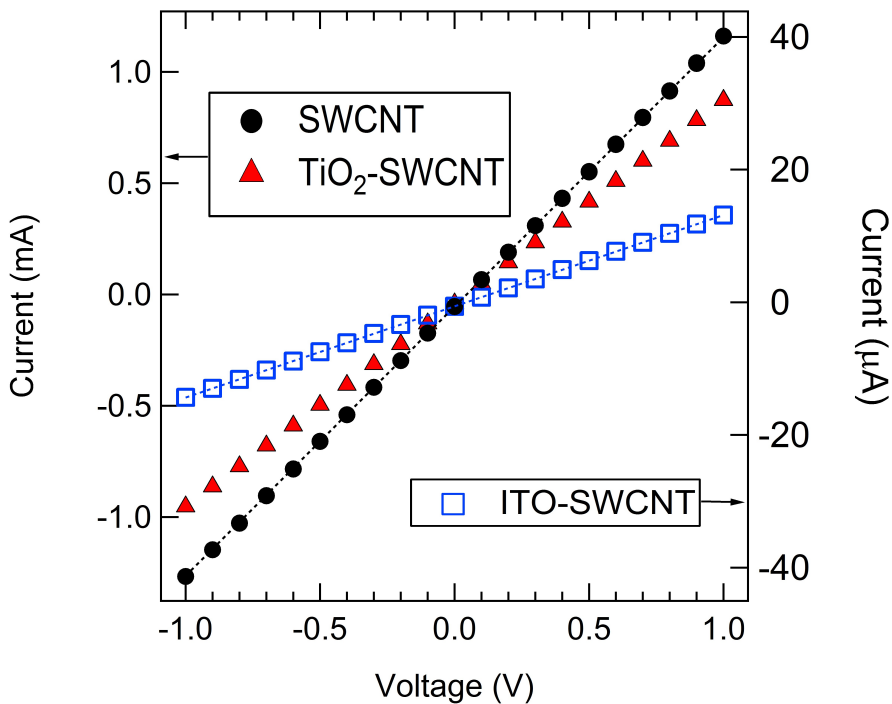


**Figure 4.7:** I-V curves of SWCNT-based chemiresistor gas sensors on plastic substrates: SWCNT (filled black circles) and functionalized TiO<sub>2</sub>-SWCNT (filled red triangles) and ITO-SWCNT (empty blue squares).

same type, but not exactly on the same samples of those tested as gas sensors

(Fig. 4.13), for this reason the resistance value is slightly different. We now report the characteristic I-V curve of SWCNT based sensor collected between the two Ag paste electrodes compared with the local I-V curve taken using the AFM tip and one of the Ag paste contact as electrodes (Fig. 4.8). As can be observed, despite the device presents an ohmic linear I-V curve, if the current is detected locally on the SWCNT bundles surface a semiconducting behaviour is detectable. This could be ascribed to the formation of a p-n junction between the p-type SWCNT bundle and the n-type silicon AFM tip.

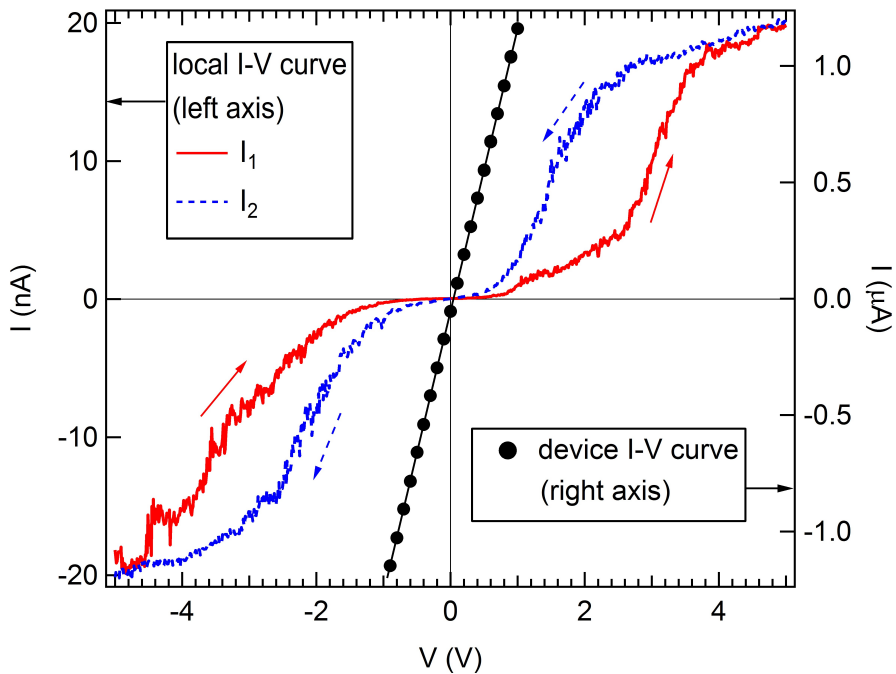


**Figure 4.8:** Local I-V curve (red solid and blue dashed line) acquired with AFM tip compared with the I-V curve collected between the two Ag paste electrodes of the SWCNT device (filled black circles).

## 4.2 Modeling of sensing: space-charge layers at nano-scale semiconductor interfaces

In this section we want to introduce and summarize a common understanding about gas sensing mechanism of semiconductors [88–90] and space-charge layers at semiconductor interfaces [91]. So far most of the work has been done on metal oxide semiconductors, since Heiland *et al.* [92] more than 60 years ago have shown that the conductivity of semiconducting metal oxides (SMOX) depends on the adsorption or desorption of gas molecules on their surface and Seiyama *et al.* proposed in 1962 the use of ZnO thin film layers as gas detectors [93]. Since that time gas sensors based on n-type and p-type SMOX has been studied by a great number of researchers but, although progresses have been made in this field, the gas sensing mechanism has not been fully understood. Works on gas sensing modeling are being carried out also by considering materials different from SMOX, e.g. carbon nanotubes, which also show a conductivity depending on the composition of the surrounding atmosphere (as we have already reported in previous chapters).

### 4.2.1 Classification of space-charge layers for n-type and p-type semiconductors

An adsorbed molecule on a semiconductor surface represents a perturbation to the local charge balance, so that electronic states at the surface are rearranged to screen this perturbation [91]. The spatial regions of redistributed screening charges are called space charge regions. Depending on the position of the Fermi level at the surface and on the type of molecules adsorbed (reducing-donors, or oxidizing-acceptors), an accumulation of surface charge can be created, which is screened by an opposite charge inside the semiconductor material. The charge of the surface states  $Q_{ss}$  (charge density per unit area) is compensated by an opposite charge inside the semiconductor, the space charge  $Q_{sc}$

$$Q_{ss} = -Q_{sc} \quad (4.1)$$

The condition of charge neutrality (4.1) determines the position of the Fermi level at the surface. Fig. 4.9 (taken from ref. [91]) shows schematic plots of (a) band schemes, (b) free carrier densities  $n$  and  $p$  and (c) local conductivity  $\sigma$

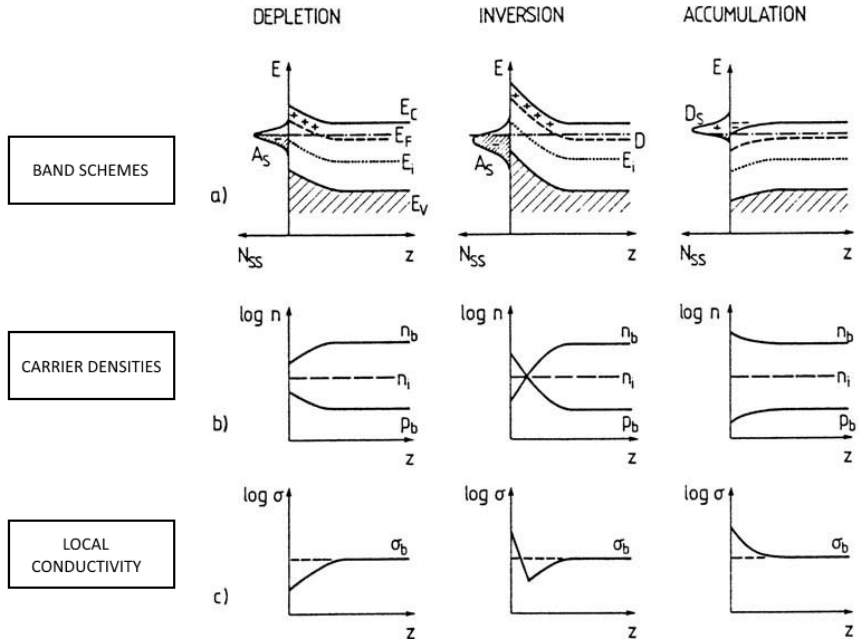


**Figure 4.9:** Illustrating the n-type semiconductor: schematic plots of band schemes (a), free carrier densities  $n$  and  $p$  on a logarithmic scale (b) and local conductivity  $\sigma$  (logarithmic scale) (c) for depletion, inversion and accumulation space charge layers.  $E_C$ ,  $E_V$  are the conduction and valence band edges,  $E_F$  the Fermi energy,  $E_i$  and  $n_i$  intrinsic energy and concentration, respectively.  $D$  denotes bulk donors,  $A_s$  and  $D_s$  surface acceptors and donors, respectively. The subscript  $b$  denotes bulk values. Figure taken from Ref. [91].

for depletion, inversion and accumulation space charge layers, in n-type semiconductors. The equilibrium requires that the charge  $Q_{ss}$  in surface states is compensated by a space charge  $Q_{sc}$  within a certain depth in the semiconductor. The distribution of space charge  $Q_{sc}$  is related, via Poisson's equation, to the curvature of the electronic bands, i.e., the potential in the space-charge layer. In an n-type semiconductor with bulk donors ( $D$ ), the band bending causes the depletion of the free conduction-band electrons which are pushed away from the surface (Fig. 4.9, left column). In this region, called *depletion layer*, there is a decrease in the density of free electrons (majority carriers) and an increase of the hole density (minority carriers) with respect to the bulk density  $n_b$  and



$p_b$ , respectively (Fig. 4.9b). As a consequence the local electrical conductivity  $\sigma(z)$  is decreased near the surface with respect to its bulk value  $\sigma_b$  (Fig. 4.9c). Stronger upwards band bending is possible if the densities  $N_{ss}$  of surface acceptor states ( $A_s$ ) is higher, inducing an inversion space charge layer (Fig. 4.9 a, middle column). The band bending is so strong that the intrinsic energy  $E_i$  crosses the Fermi energy  $E_F$ . The intrinsic level  $E_i$  is the ideal level of the Fermi energy of a semiconductor without doping and it is given by

$$E_i = \frac{1}{2}(E_C - E_V) - \frac{1}{2}kT \ln(N_{eff}^c/N_{eff}^v) \quad (4.2)$$

where  $N_{eff}^c$  and  $N_{eff}^v$  are the effective conduction- and valence-band densities of states.  $E_i$  is a convenient quantity to describe whether a semiconductor is intrinsic, p-type or n-type: if  $E_F = E_i$ , we have intrinsic behavior; if  $E_F < E_i$  the semiconductor is p-type with holes as the majority carriers; whereas if  $E_F > E_i$  n-type conductivity occurs. The type of conduction changes in an inversion layer, so that the n-type semiconductor ( $E_i < E_F$ ) becomes p-type near the surface ( $E_i > E_F$ ). Correspondingly the free-electron density  $n$  decreases to below the intrinsic value  $n_i$ , near the surface, whereas the hole concentration  $p$  exceeds the intrinsic value (Fig. 4.9 b). The conductivity  $\sigma$  has the lowest local value at the point where  $n$  and  $p$  cross on the intrinsic concentration level  $n_i$  and between this point and the very surface  $\sigma$  increases again due to the presence of an enhanced density of bulk minority carriers (inversion) (Fig. 4.9 c).

Accumulation space charge layers on n-type semiconductors, as depicted in Fig. 4.9 (right column), require the presence of donor-type surface states  $D_s$ . The positive charge density  $Q_{ss}$  must be compensated by an equal amount of negative space charge. Free electrons accumulate in the conduction band below the surface and the electronic space charge of the so-called accumulation layer is related to a downward band bending. In strong accumulation layers the conduction-band minimum might even cross the Fermi level and the semiconductor becomes degenerate in the spatial region of the accumulation layer [91]. In Fig. 4.9 b,c (right column), the qualitative dependence of the densities of majority carriers ( $n$ ) and minority carriers ( $p$ ) and of the local electrical conductivity  $\sigma$  is reported. On p-type semiconductors the situations depicted in Fig. 4.9 are reversed. Free holes in the valence band are the majority carriers in the bulk; an accumulation layer is therefore formed by a positively charged hole gas. The opposite charge  $Q_{ss}$  in surface states must be negative. Thus the

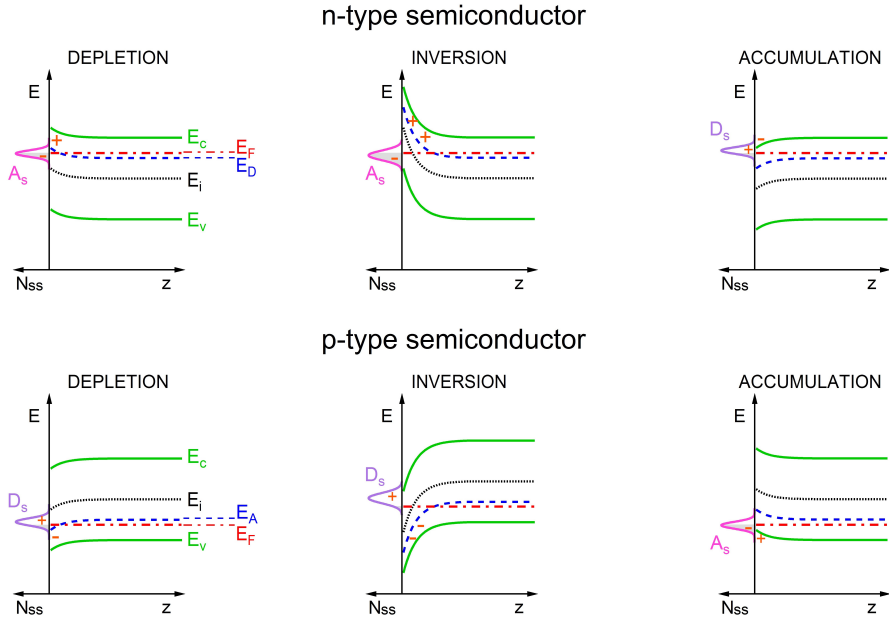


**Figure 4.10:** Band schemes for n-type and p-type semiconductors, for depletion, inversion and accumulation space charge layers.  $E_C$ ,  $E_V$  are the conduction and valence band edges,  $E_F$  the Fermi energy,  $E_i$  intrinsic energy,  $E_A$  and  $E_D$  denote bulk energy of acceptors and donors, respectively.  $A_s$  and  $D_s$  are surface acceptors and donors, respectively.

presence of a hole accumulation layer on a p-type semiconductor requires partially filled acceptor-type surface states and the bands are bent upwards near the surface.

The band schemes for both n-type and p-type semiconductors are shown in Fig. 4.10. In case of an acceptor molecule ( $A_s$ ), for example adsorbed molecular oxygen  $O_2$ , on the surface of a semiconductor material there is accumulation of negative surface charge  $Q_{ss}$  that induced positive space charge  $Q_{sc}$ , causing an upward band bending and a depletion region of electrons in n-type semiconductors, while in a p-type semiconductor the upward band bending creates an accumulation region of holes. If the densities of surface acceptors are very high (we can compare this situation to high values of oxidizing gas concentra-

tions), the upward band bending in n-type semiconductors is enhanced and an inversion layer is formed near the surface. When we have to deal with donor molecules ( $D_s$ ), e.g. reducing molecule like ammonia  $\text{NH}_3$ , adsorbed on the surface, the accumulation of positive  $Q_{ss}$ , induces negative  $Q_{sc}$ , corresponding in a downward band bending and accumulation of electrons near the surface in the case of n-type semiconductors, while in p-type semiconductors a depletion layer for holes is built up. Also in this case, if the densities of surface donors are very high (i.e. high concentrations of reducing gases), the downward band bending is stronger and an inversion layer, with consecutive change of the majority carriers from holes to electrons, is possible (the schemes of free carrier densities and conductivity  $\sigma$  are the same of those reported in Fig. 4.9 b,c, apart from changing electrons with holes, i.e. n with p).

The take home message of all this description of sensing modeling (at which we'll refer in next paragraphs) is that band bending induce depletion regions at the surface (depletion or accumulation layers, depending on the type of semiconductor and on the type of adsorbed molecule).

### 4.2.2 Nano-heterojunction

From the electronic band point of view, SWCNT bundle and ITO (or in general SMOX) nanoparticle create a *nano-heterojunction* (depicted in Fig. 4.11 a) and a depletion layer between the two material is built up (near  $z=0$  in Fig. 4.11 b). The energy gap of p-type material ranges from 0.05 eV for metallic SWCNTs to 0.5 eV for semiconducting SWCNTs [94], while metal oxides n-type nanoparticles display a higher band gap [84]. For instance, the  $E_g$  of ITO nanoparticles is about 3.4 - 4 eV [95]. In literature it is common to find that materials like  $\text{SnO}_2$ ,  $\text{TiO}_2$ , ITO (also in nanoparticle structure) display a n-type behaviour and they are used in gas sensing usually at high temperatures [96]; while SWCNTs in earth atmosphere, where the presence of oxygen play a crucial role in the hole doping [44], are considered p-type materials. In Fig. 4.11 a sketch of nano-heterojunction between p-type SWCNT and n-type SMOX nanoparticle and the corresponding electronic band diagram are shown.

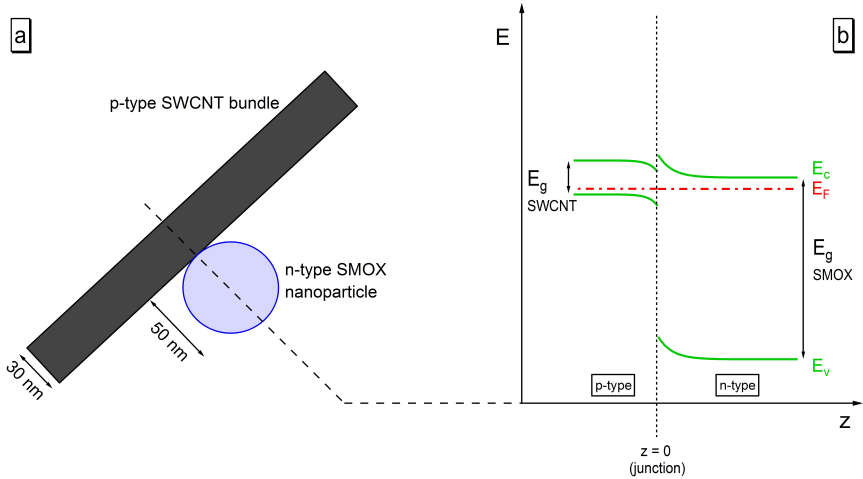


**Figure 4.11:** (a) Sketch of nano-heterojunction between p-type SWCNT and n-type SMOX nanoparticle. (b) Electronic band diagram of the junction.

## 4.3 Results and discussion

### 4.3.1 Response to ammonia in air and in gas testing chamber

In this section we start to consider and analyze the sensor response ( $\Delta R/R_0$ ) to gases. In order to compare the sensors response of SWCNT and ITO-SWCNT sample,  $R_s$  was evaluated in each case against  $R_0$ , i.e. the baseline resistance before exposure to gas, and the  $\Delta R/R_0 = R_s - R_0/R_0$  values are plotted versus  $\text{NH}_3$  concentrations to obtain the response curve. As expected  $\Delta R/R_0$  increases with  $[\text{NH}_3]$ , displaying a sub-linear regime. Following Ref. [74], for each sample the collected data set was fitted with a power law:  $\Delta R/R_0 = A \cdot [\text{NH}_3]^p$ . Let's consider the response to ammonia gas, in lab air conditions, of the sample prepared by SWCNTs layer and ITO-SWCNTs on plastic substrate (Fig. 4.13). The starting resistance  $R_0$  of the two samples is different, in accordance with the

fact that ITO nanoparticles and SWCNT bundles create a nano-heterojunction (as we have seen in previous section) and a depletion layer may be responsible to increase the resistance, from about  $500 \Omega$  (for SWCNT pristine layer) to  $130 \text{ k}\Omega$  (for ITO-SWCNT sample).

Let's now consider how a higher sample's resistance  $R_0$  may help to improve the sensor response  $\Delta R/R_0$ . We simplify the problem with the assumption of imaging the sensor as composed by several resistor in parallel (Fig. 4.12, left panel). The molecules will interact only with the  $i^{\text{th}}$  of these  $N$  resistors. If

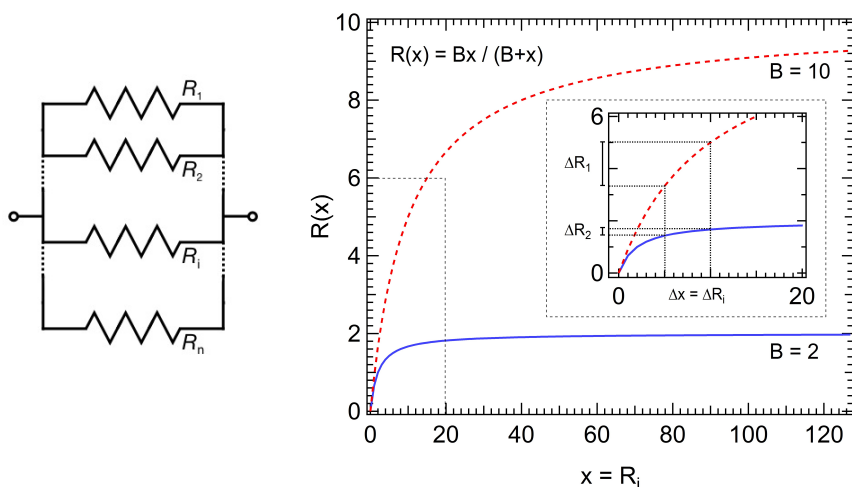


**Figure 4.12:** LEFT PANEL: sample resistance represented by  $N$  resistors in parallel, of which only  $R_i$  interacts with gas molecules; RIGHT PANEL: equivalent resistance  $R$  as function of the interacting resistance  $R_i=x$ .

the  $N$  resistors except the interacting one,  $R_i$ , give rise to an effective resistance  $R_N^{\text{eff}}$ , the total equivalent resistance  $R_{\text{eq}}$  is given by

$$\frac{1}{R_{\text{eq}}} = \frac{1}{R_N^{\text{eff}}} + \frac{1}{R_i} \quad (4.3)$$

that we can rewrite in terms of the variable during gas exposure  $x = R_i$  and the parameter  $B = R_N^{\text{eff}}$

$$R(x) = \frac{Bx}{B+x} \quad (4.4)$$

This function is plotted in Fig. 4.12 (right panel) for two different example values of  $B$  ( $B_1=10$ ,  $B_1=2$ ). Except for  $R_i$ ,  $B$  is almost the total resistance of the sample. If we consider  $B_1 > B_2$  (the resistance of sample 1 is greater than the resistance of sample 2), the same interaction ( $\Delta x = \Delta R_i$ ) of the gas molecules with  $R_i$  affects in different way the total resistance  $R(x)$ .

In Fig. 4.13 the response to 5 different ammonia exposures of the two sensors is reported. The time duration of each  $\text{NH}_3$  exposure was 3 min and the responses are characterized by a step increase of the resistance in a short time

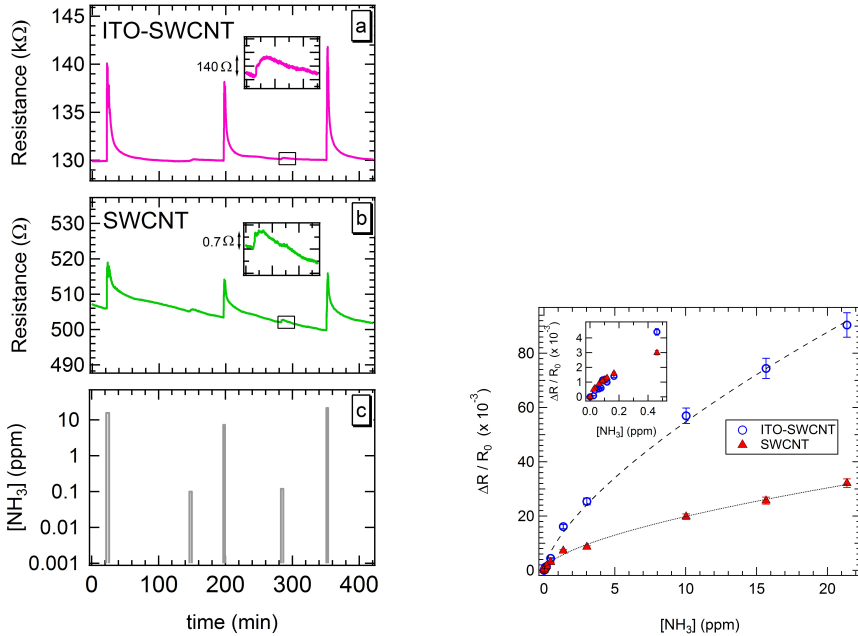


**Figure 4.13:** LEFT PANELS: example of responses to 5 different ammonia gas exposures of the SWCNTs functionalized with ITO nanoparticles (a) and of the pristine SWCNTs (b). The ammonia concentration values (3 exposures above and 2 below the ppm) are reported in log scale (c). The insets blow up the responses to the fourth exposures ( $[\text{NH}_3] = 120$  ppb). The relative humidity and the temperature during the measurements were  $\text{RH} = 46 \pm 1\%$ ,  $T = 25 \pm 1^\circ\text{C}$ . RIGHT BOTTOM PANEL: response curves for the SWCNT-based sensor onto plastic substrate: pristine SWCNTs (filled red triangles) and ITO-SWCNTs blend (empty blue circles) [86].

(rise time), and when the gas source is removed, by a slower decrease (recovery time). The measurements have been carried in the laboratory air and not in a sealed testing chamber, in order to reproduce the real environmental working conditions, in which the sensors will have to work. It is remarkable to observe that the response of ITO-SWCNT blend shows a faster recovery time with respect to the pristine SWCNT for ammonia exposures above 1 ppm. By fitting

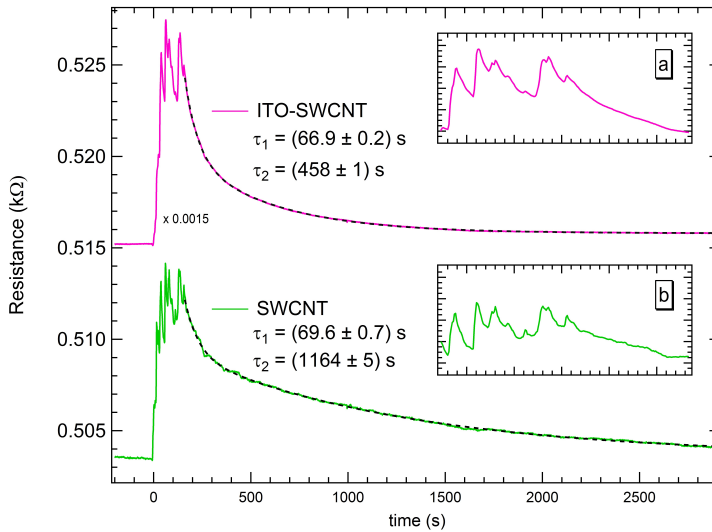


**Figure 4.14:** Example of ammonia gas response of SWCNT (green curve) and ITO-SWCNT (pink curve, scaled by a factor 0.0015). The curves have been fit during the recovery time by a double exponential function (dashed lines). In the insets, the fluctuations observed on top of the curve during gas exposure of ITO-SWCNT (a) and SWCNT sample (b) are shown.

with a double exponential function the central peak of Fig 4.13 (top panel) during the recovery time, we obtain the following decay times:  $\tau_1 = 66.9 \pm 0.2$  s and  $\tau_2 = 458.5 \pm 0.9$  s for ITO-SWCNT sample;  $\tau_1 = 69.6 \pm 0.7$  s and  $\tau_2 = 1164 \pm 5$  s for SWCNT sample. In Fig. 4.14 the fits (dashed lines) and the fluctuations observed on top of the curve during gas exposure are shown. A slowly decreasing background at the beginning of a set of measurements is occasionally observed, as in Fig. 4.13 b. This drift disappears when the sensor is operated for few hours and does not affect the sensor response reported in the present study.

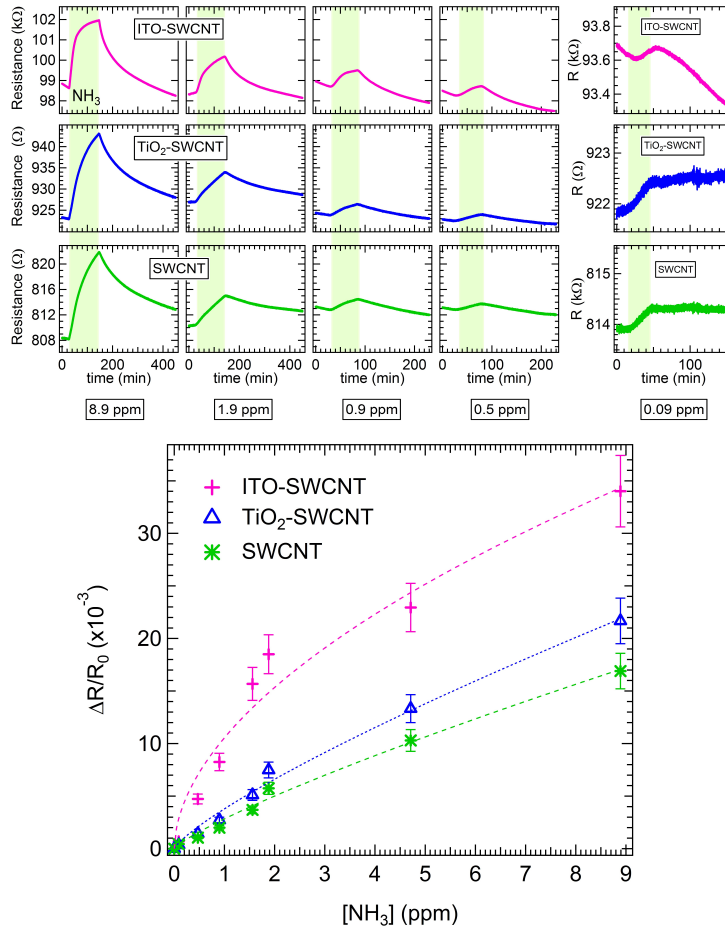


**Figure 4.15:** TOP PANEL: Data set collected in gas testing chamber from the three samples upon exposure to different ammonia concentrations ranging from 8.9 ppm down to 0.09 ppm. For each exposure the three sensors responses were collected simultaneously. BOTTOM PANEL: response curve. The relative humidity and the temperature during the measurements were RH=11±1%, T=26±1°C.

Fig. 4.15 shows the ITO-SWCNT, TiO<sub>2</sub>-SWCNT and SWCNT sensor response upon exposure to NH<sub>3</sub> at different concentrations. In this case the measures



have been carried out in a gas testing chamber (1 l volume) using  $\text{NH}_3$  diluted in dry air flowing in the chamber with a total flow of 50 sccm (except for the 0.09 ppm ammonia exposure, when a total flow of 500 sccm has been set). In all cases, the resistivity  $R_s$  of the three sensors, the relative humidity and temperature were recorded simultaneously by mounting all sensors on the same board. As can be observed all sensors display a sensitivity down to 90 ppb. During the measurement the temperature T and the relative humidity R.H. were at  $T=26\pm 1^\circ\text{C}$  and  $\text{R.H.}=11\pm 1\%$ , respectively. An enhanced response to ammonia is observed for the ITO-SWCNT sample, while the  $\text{TiO}_2$ -SWCNT seems to respond very similar to the SWCNT. This could be ascribed to a not-effective functionalization in the case of  $\text{TiO}_2$  nanoparticles. This fact is also supported by the value of the resistance ( $R_{\text{TiO}_2\text{-SWCNT}} \approx R_{\text{SWCNT}}$ ).

On the basis of a sequence of ammonia exposures, we obtain the response curve of the two sensors in air (Fig. 4.13, right bottom) and in gas testing chamber (Fig. 4.15, bottom panel). In Fig. 4.13 (right bottom panel), the data above 1 ppm were fitted with a power function (following the Freundlich equation and Ref. [74]) where the sensor response  $\Delta R/R_0$  is related to the ammonia concentration  $[\text{NH}_3]$  (ppm) by the equation

$$\frac{\Delta R}{R_0} = A \cdot [\text{NH}_3]^p \quad (4.5)$$

The fit parameters are reported in Table 4.1. The detection limit (DL) can

Sample	$R_0$ ( $\Omega$ )	$\sigma$ ( $\Omega$ )	A ( $10^{-3}$ )	p
SWCNT	500	0.034	$4.8 \pm 0.5$	$0.61 \pm 0.04$
ITO-SWCNT	130000	6	$11 \pm 0.3$	$0.68 \pm 0.01$

**Table 4.1:** Values (related to Fig. 4.13, right bottom panel) of standard deviation ( $\sigma$ ) from the baseline resistance ( $R_0$ ) and fit parameters, A and p, of the response curve (response in air), used to calculate the detection limit (DL). The relative humidity and the temperature during the measurements were  $\text{RH}=46\pm 1\%$ ,  $T=25\pm 1^\circ\text{C}$  [86].

be derived from the value of the instrumental noise fluctuations  $\sigma$ , i.e. the standard deviation of the baseline signal  $R_0$  before ammonia exposure, and the value of the fit parameters from the response curve. Eq.4.5 allows us to find the  $[\text{NH}_3]$  value corresponding to a resistance variation  $\Delta R = 5\sigma$ ; consistently this  $[\text{NH}_3]$  value can be defined as DL. Indeed, according to the equation:

$(5\sigma/R_0) = A (\text{DL})^p$ , the detection limit evaluated by fitting the data in a broad concentration range (i.e. up to 22 ppm) results to be 13 ppb for the pristine SWCNT-based chemiresistor gas sensor on plastic substrate. Here noise fluctuations were evaluated as  $\sigma = 0.034 \Omega$ . The ITO-SWCNT-based sensor is more sensitive than the pristine SWCNT-based one at high  $\text{NH}_3$  concentrations, i.e. above 200 ppb. However it should be remarked that the two sensors show a similar response in the 0-200 ppb range. Therefore, as the DL is meant to be the relevant parameter to characterize the response at low concentrations, we regard the DL measured for the undoped SWCNTs as the DL also for the functionalized CNTs. This value is consistent with that (3 ppb) reported for similar layers deposited on ceramic substrates equipped with interdigitated contacts (data reported in chapter 3 of this thesis and in Ref. [66]), rather than with relatively distant parallel stripes of silver paint of the present samples. As the signal-to-noise ratio ( $\text{SNR} = \sigma/R_0$ ) is quite similar, the DL difference with respect to the ceramic interdigitated sample can be ultimately ascribed to the A and p coefficients of Eq. 4.5. The factor A is the sensitivity ( $A = \Delta R/R_0$  when  $[\text{NH}_3] = 1 \text{ ppm}$ ) and the exponent p is expected to be  $p = 0.5$  in an ideal microstructure, but the effect of randomness increase p above this value [97]. Actually, we have  $A = 0.015$ ,  $p = 0.56$  for the SWCNT onto ceramic interdigitated substrate (chapter 3), against  $A = 0.0048$ ,  $p = 0.61$  for the SWCNT on plastic (Table 4.1). The decrease in the sensitivity parameter A can be attributed to the less efficient and more distant Ag paint contacts with respect to the interdigitated Pt electrodes capable of collecting a greater amount of transferred charge. Therefore, with methods typical of flexible electronics, the deposition of interdigitated finger electrodes on plastic substrates is expected to provide a way (i) to enhance the sensitivity factor A and to reduce the noise through high quality electrical contacts and (ii) to control thickness and density of the layers (and ultimately  $R_0$ ) by using dielectrophoresis as a method for the thin layer deposition. It is important to observe that while at low concentrations the sensors display a comparable response to  $\text{NH}_3$  exposure (inset of Fig.4.13, right bottom panel), above a threshold of about 200 ppb, the ITO-SWCNT blend shows a larger sensitivity than the pristine sample, because of the greater  $R_0$ , as discussed before (see Eq. 4.4 and Fig. ??). The behavior at very low concentrations, i.e.  $[\text{NH}_3] < 200 \text{ ppb}$ , could be ascribed to the ITO coverage of the SWCNT bundles that can be detrimental to response for low  $[\text{NH}_3]$ , as in

this regime it may hinder an efficient transport of the few injected charges to the SWCNT conduits. Differences between the two sensing materials have also been detected in the response to other polluting gases. Indeed, a preliminary survey (Fig.4.16) indicates that the ITO-SWCNT blend is less sensitive to acetone and ethanol, resulting in a selectivity increase towards these pollutants.

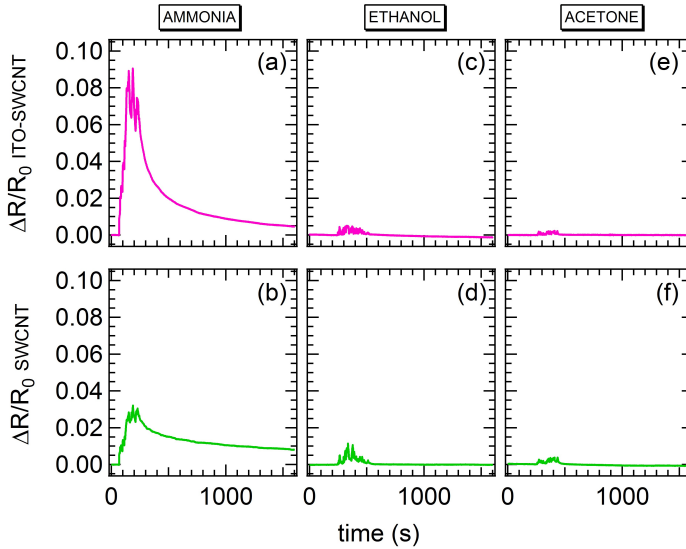


**Figure 4.16:** Responses to 20 ppm ammonia (a, b), 30 ppm ethanol vapor (c, d) and acetone (e, f) of ITO-SWCNT blend and SWCNT layer, respectively. The relative humidity during the measurements was  $43\pm 1\%$  and the temperature  $24\pm 1^\circ\text{C}$ .

Also in the case of measurements in gas testing chamber, the data of the response curve  $\Delta R/R_0$  versus  $[\text{NH}_3]$  was fitted with a power law and the results of the fitting are shown in Fig. 4.15 (bottom panel) as continuous lines, while the A and p parameter values are summarized in Table 4.2. As can be observed, the functionalization with oxide nanoparticles increases for each  $[\text{NH}_3]$  the  $\Delta R/R_0$  value, clearly showing that oxide functionalization can be regarded as a straightforward way to increase the sensor sensitivity to ammonia. The highest response is displayed by the ITO-SWCNT sensor, while the  $\text{TiO}_2$ -SWCNT sensor shows an intermediate behavior.

Sample	A ( $10^{-3}$ )	p
SWCNT	$2.8 \pm 0.2$	$0.82 \pm 0.04$
TiO <sub>2</sub> -SWCNT	$3.8 \pm 0.3$	$0.80 \pm 0.04$
ITO-SWCNT	$10.5 \pm 1.1$	$0.54 \pm 0.06$

**Table 4.2:** Values (related to Fig. 4.15, bottom panel) of standard deviation ( $\sigma$ ) from the baseline resistance ( $R_0$ ) and fit parameters, A and p, of the response curve (response in gas testing chamber), used to calculate the detection limit (DL). The relative humidity and the temperature during the measurements were RH= $11 \pm 1\%$ , T= $26 \pm 1^\circ\text{C}$ .

### 4.3.2 Response to humidity

One of the most important interfering gas in the ammonia environmental monitoring is water vapor (humidity). Theoretical studies, supported by experimental results, show that the H<sub>2</sub>O molecule has the same reducing effect of NH<sub>3</sub> in the interaction with carbon nanotubes, yielding a charge transfer to CNTs of 0.033 - 0.035 electrons per H<sub>2</sub>O molecule, against 0.027 - 0.031 elec-

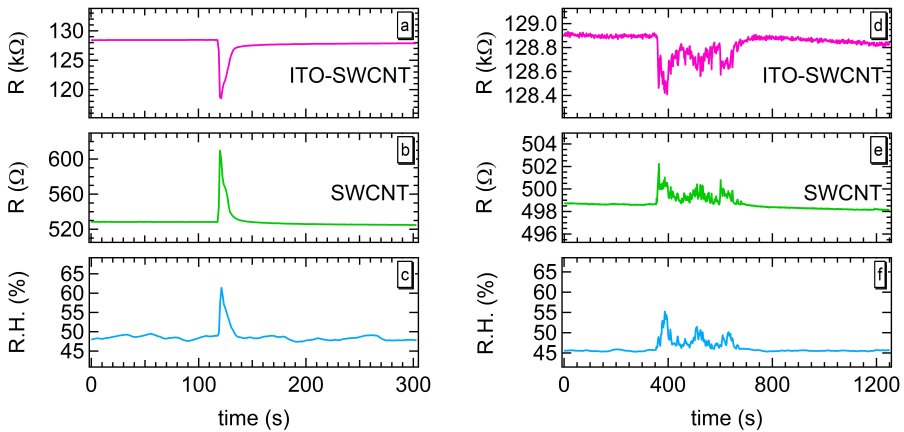


**Figure 4.17:** Response to humidity of the sample based on ITO-SWCNT (a,d) and pristine SWCNT on plastic substrate (b,e). Relative humidity (R.H.) concentration (c,f). Exposure to human breath (a-c), results in an R.H. increase from 50% to 60% (corresponding to 3250 ppm); while exposure to water vapor (d-f), yields an R.H. increase from 45% to 55% (about 3270 ppm). The temperature during the measurements was  $23 \pm 0.5^\circ\text{C}$ .

trons per  $\text{NH}_3$  molecule [48]. These charge transfer effects determine, for both gases, an increase in the resistance of the CNT based gas sensor [98,99], hindering the selective detection of the ammonia molecules. Usually an increase of sensitivity towards  $\text{H}_2\text{O}$  was observed upon functionalization of pristine CNT with different molecules [100]. With respect to these results, we observed a quite different response of the ITO-SWCNT sensor to humidity (Fig. 4.17). Two different humidity tests were carried out: exposure to human breath (Fig. 4.17, a-c panel) and exposure to a water source (Fig. 4.17, d-f panel). In both cases, the pristine SWCNT-based sensor shows an increase of the resistance with the relative humidity (R.H.), while in the sample based on ITO-SWCNT blend a decrease in the sensor resistance is observed. This opposite resistance variation discloses the possibility to discriminate the presence of water or ammonia in the atmosphere (we remind that in presence of low concentrations of ammonia both sensors show a positive variation of the resistance, as reported in Fig. 4.13) by operating with a sensing system equipped with both sensors. Conversion from R.H. (%) to ppm of water was carried out according to the formulas reported in Appendix C.

### 4.3.3 Response to nitrogen dioxide

The sensor behavior upon exposure to  $\text{NO}_2$  is shown in Fig. 4.18. Here the three sensors (ITO-SWCNT,  $\text{TiO}_2$ -SWCNT and SWCNT) were tested against 1 ppm and 0.5 ppm  $\text{NO}_2$  concentrations (the response  $\Delta R/R_0$  of the three sensors to 1 ppm  $\text{NO}_2$  is shown in Table 4.3). Also in this case the measurements were carried out in a gas testing chamber (1 l volume, 500 sccm total air flow) at room temperature ( $T = 26.5 \pm 1.8^\circ\text{C}$  and  $\text{RH} = 7.5 \pm 1.9\%$ ). For both concentrations all sensors display a resistivity change, but the recovery appears to be quite slow as compared to the ammonia case. This is not surprising as  $\text{NO}_2$  is known to react more strongly with CNT as compared to ammonia (see, e.g.

$[\text{NO}_2]$	$\Delta R/R_0$ ITO-SWCNT	$\Delta R/R_0$ $\text{TiO}_2$ -SWCNT	$\Delta R/R_0$ SWCNT
1 ppm	0.068	-0.052	-0.046

**Table 4.3:** Response of the three sensors to 1 ppm  $\text{NO}_2$ , defined as  $\Delta R/R_0$ , where  $\Delta R = R_s - R_0$  is the difference between the sample resistance in presence of gas ( $R_s$ ) and the resistance before gas exposure ( $R_0$ ).

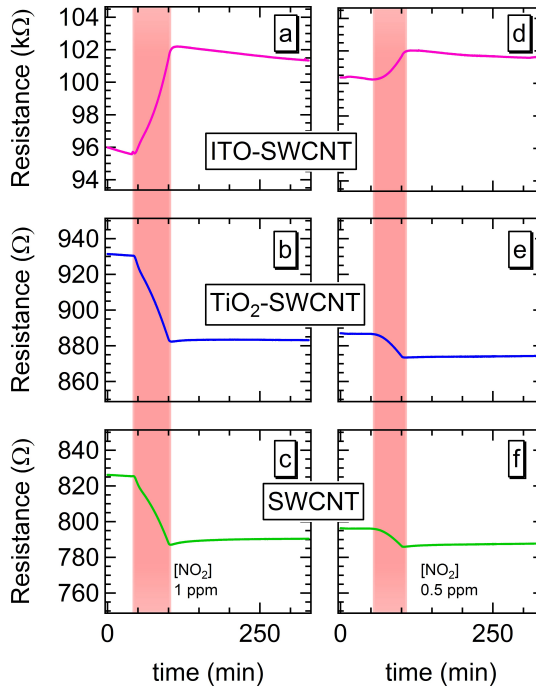


**Figure 4.18:** ITO-SWCNT (a, d), TiO<sub>2</sub>-SWCNT (b, e) and SWCNT (c, f) sensor responses during 1 ppm (a-c) and 0.5 ppm (d-f) NO<sub>2</sub> exposures.

Ref. [48] for a theoretical investigation of adsorption energies on several kind of CNTs). Furthermore, while the SWCNT and the TiO<sub>2</sub>-SWCNT samples display a p-type behavior upon exposure to the oxidizing NO<sub>2</sub> molecules, the ITO-SWCNT display an n-type behavior, with a resistivity increase during the exposure to NO<sub>2</sub>. This behavior can be used, by combining the response of the three sensors, to enhance the selectivity of these sensors during a simultaneous exposure to NH<sub>3</sub> and NO<sub>2</sub>. While  $R_s$  increases when the sensor bench is exposed to ammonia, a reduction of this increase could be detected by the SWCNT and TiO<sub>2</sub>-SWCNT samples when NO<sub>2</sub> is introduced in the chamber with ammonia, due to the opposite effects of these molecules on the sample resistance. This reduction could be erroneously interpreted as a reduction of ammonia concen-

tration, unless the ITO-SWCNT sensors display a resistivity increase, revealing the presence of  $\text{NO}_2$ . This combined measurement approach can be developed towards possible applications provided that the problem of the slow recovery upon  $\text{NO}_2$  exposure is solved.

### UV curing effects

One possible way to overcome the lack of a fast recovery is the use of UV irradiation (UV curing) to restore the original  $R_0$  values. An example of the UV effects on the sensor resistance is shown in Fig. 4.19, where the sensors

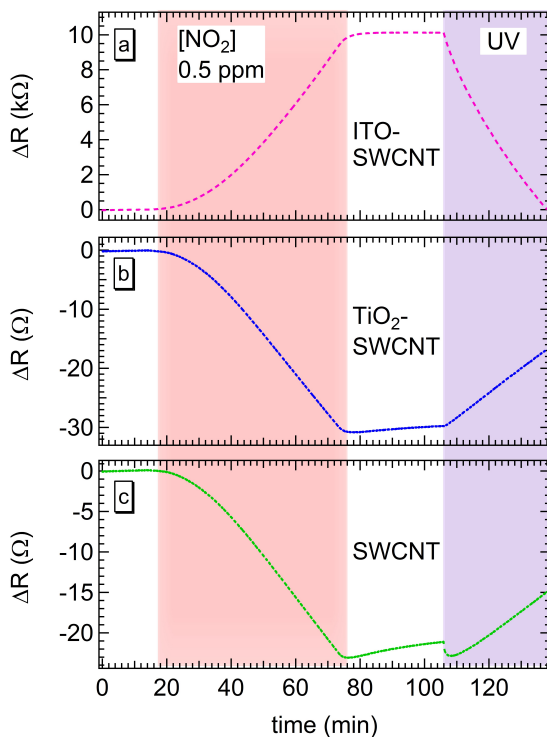


**Figure 4.19:** Effects of UV curing on the recovery after the exposure to 0.5 ppm  $\text{NO}_2$ . (a) ITO-SWCNT; (b)  $\text{TiO}_2$ -SWCNT; (c) SWCNT.

response to the same  $\text{NO}_2$  exposure is recorded, followed by UV irradiation. As can be observed,  $R_s$  is driven close to the initial value for the SWCNT and  $\text{TiO}_2$ -SWCNT sensors, and is virtually restored for the ITO-SWCNT sensor, demonstrating the possibility to drive the baseline resistance with UV irradiation to overcome poisoning effects due to strongly interacting molecules. To get further insight into the  $\text{NO}_2/\text{CNT}$  interaction in the presence of UV irradiation, a photoemission study was carried out on the pristine SWCNT layer. Photoemission spectroscopy is known to be a powerful tool to track the gas interaction with surfaces, and an example of a systematic investigation of several gas molecules on CNT is reported in Ref. [15].

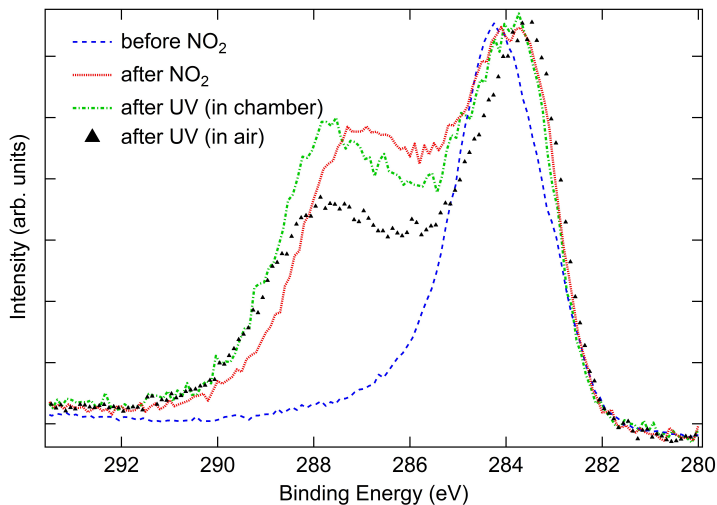


**Figure 4.20:** C 1s XPS core level measured on the pristine SWCNT layer before and after  $\text{NO}_2$  exposure and after UV curing (UV illumination in the vacuum chamber and in air).

The results of the XPS measurements are shown in Fig. 4.20, where the C 1s core level emission is reported for the pristine SWCNT layer, for the same layer exposed to 1 ppm  $\text{NO}_2$  before UV curing, and after UV curing in ultra-high vacuum and in air. As can be observed, differences among the spectra are relevant and involve both the energy of the main line and the overall lineshape. After exposure to  $\text{NO}_2$  the binding energy of the C 1s main line decreases, as expected



by the oxidizing effect of  $\text{NO}_2$  adsorbed on a p-type material. Furthermore a large satellite appears on the high binding energy side of the C 1s peak. This is ascribed to the interaction of CNT with oxygen. This peak is slightly reduced after UV irradiation in the analysis chamber and is further reduced after UV irradiation in ambient air. Therefore we can rationalize this behavior as follows. UV irradiation may induce the desorption of oxygen initially brought about by  $\text{NO}_2$  adsorption to a considerable extent, though the initial condition is not fully restored, in agreement with the resistance measurements on pristine SWCNT.

#### 4.3.4 Sensing mechanism

In order to explain the response to ammonia, water vapor and nitrogen dioxide gas, we propose the following models of sensing (i) based on SWCNTs density of states (DOS) and (ii) a gas sensing mechanism that considers depletion/accumulation regions due to p-n junction and adsorbed molecules effects (referring to Sect. 4.2).

##### SWCNTs DOS modeling

At the light of the present results we rationalize the response of our sensors to humidity and ammonia by considering the effect of gases interactions in the density of states (DOS) of SWCNTs. On the basis of the resistance change (increase or decrease) with respect to the presence of oxidizing or reducing gases it is possible to classify the doping type of semiconducting materials [101]. In particular, according to a work of Han et al. [102], the doping character of a nanomaterial can be determined on the basis of the electrical response to humidity, by considering that water molecules display a reducing character. Materials that present a resistivity decrease are classified as n-type, while p-type materials are those showing a resistivity increase. Applying this simple method to our case, looking at the response to humidity, the pristine SWCNTs should be p-type, while the sample based on ITO-SWCNT blend shows an n-type behavior. We can then suggest that the effect of the ITO nanoparticles (known as n-type semiconductors) turns the device material from p-type into n-type. But the response to ammonia (Fig. 4.13), that is a reducing gas and is expected to transfer electrons to the sample surface, seems to be at odds with this argument, as the ITO-CNT material displays a p-type character when exposed to

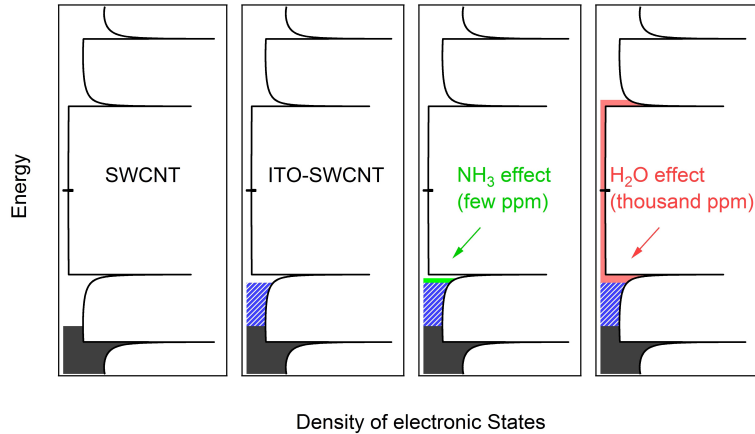


**Figure 4.21:** Schematic representation of the density of states (DOS) of p-type SWCNTs (a), ITO-SWCNT blend sample (b), NH<sub>3</sub> effect (few ppm of ammonia gas) during the interaction with ITO-SWCNT blend (c), and water vapor (thousand ppm of H<sub>2</sub>O molecules) effect during the interaction with ITO-SWCNTs (d).

NH<sub>3</sub>. Furthermore, Lin et al. [103] have shown that the effect of NH<sub>3</sub> on ITO thin films (n-type) alone is to decrease the resistance. Therefore we ascribe the resistance increase with NH<sub>3</sub> exposure observed in the ITO-SWCNT sample to the interaction of the ammonia molecules with the ITO nanoparticles that cover the bundle surface (Fig. ??), yielding a transfer of electrons towards the p-type SWCNTs, where transport to the electrodes occurs. The apparent contradiction we observed can be explained on the basis of the effects of the concentration range on the material electrical response. Indeed, it has been shown [104, 105] that by increasing the concentration of the reducing gas or vapor to which the nanotubes are exposed, the Fermi level may shift and the CNTs could turn from p-type into n-type materials. In particular, Zahab *et al.* demonstrated how a hole compensation effect takes place during the exposure of the p-type SWCNTs to water vapor [104]. On this basis we suggest that the role played by the ITO nanoparticles is to inject extra-electrons on the SWCNTs, reducing the hole density and shifting the Fermi level near the compensation value, as depicted in Fig. 4.21. This hypothesis could explain why the interaction with NH<sub>3</sub> (few ppm) still results in an increase of the resistance, while the in-

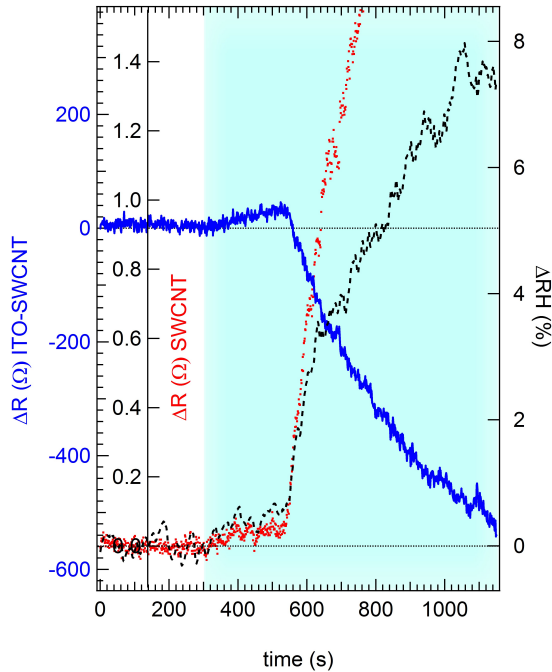


**Figure 4.22:** Resistance variation upon exposure to humidity of the sample based on ITO-SWCNT blend (blue solid line) and pristine SWCNTs (red dotted line). On the right axis the variation of the Relative Humidity ( $\Delta RH$ , black dashed line) is reported. The initial value of RH was  $(37.2 \pm 0.2)\%$  and the temperature during the measurements was  $(23.8 \pm 0.3)^\circ\text{C}$ .

teraction with  $\text{H}_2\text{O}$  molecules (thousand of ppm) bring the system above the compensation level and turn the ITO-functionalized sample into an extrinsic n-type semiconductor, with a negative resistance variation. This argument is also supported by the data of Fig. 4.22, where the resistance variation upon exposure to humidity of the sample based on ITO-SWCNT blend (blue solid line) and pristine SWCNTs (red dotted line) are shown. In fact, for a low concentration of water vapor (few ppm) the resistance of ITO-SWCNTs increases, as that of undoped SWCNTs. However, when the humidity concentration is of order of thousands of ppm, the compensation value is overcome and the ITO-SWCNT device turns into a n-type semiconductor, unlike the undoped one,

that maintain a p-type character. Finally, within the energy band scheme proposed in Fig. 4.21, the increase of sensitivity observed for the sample based on ITO-SWCNT blend can also be tentatively explained by considering the possibility that the doping effect of ITO brings the Fermi level close to a van Hove singularity in the DOS, therefore enhancing the resistivity of the SWCNTs to a larger extent with respect to a Fermi level shift in a region of lower DOS. In principle, the effects detected on the ITO-doped samples after exposure to humidity should be present upon exposure to high ammonia concentrations, as also this molecule displays a reducing behavior. This hypothesis is confirmed by the data of Fig. 4.23, where the behavior of the two sensors upon exposure to a continuously increasing ammonia concentration up to 3400 ppm is shown. Here the ammonia concentration was increased with the aim to observe the reversal of the electrical response (from p-type to n-type) in the ITO-SWCNT sample. At the beginning of the exposure the resistance increases ( $R > R_0$ ), but the expected reversal is observed to start at  $[\text{NH}_3] = 840$  ppm ( $t = 2$  min) to be finally set at  $[\text{NH}_3] = 2670$  ppm ( $t = 3$  min 58 s), where  $R < R_0$ . Here the ITO-SWCNT sample has switched from the p-type to n-type behavior, confirming the presence of a hole compensation effect at the basis of the picture proposed in Fig. 4.21.

### Space-charge in p-n junction modeling

Instead of considering the DOS of SWCNTs, we can explain the response to gases by taking into account the p-n nano-junction that is built up between the SWCNT bundle and the ITO nanoparticle (see Fig. 4.11 in Sect. 4.2.2), at the origin of the increase of the ITO-SWCNT sample resistance, because of the depletion region formed at the junction. In literature a considerable number of studies on gas sensing mechanism in n-type and p-type SMOX can be found [88–90, 96, 106], where the materials are also combined to form p-n junctions between n-type nanotube and p-type nanoparticles on top of it [107–110]. Recent works on hybrid SMOX-SWCNTs [79–85] have been published where p-n junction between p-type SWCNTs and n-type SMOX nanoparticles, or on hybrid CNT-metal nanoparticles junction [111, 112]. However, the researchers currently agree in thinking that a clear gas sensing mechanism is not fully understood [88]. In the following paragraph gas sensing mechanisms are discussed at the light of the results we obtained on the response of our systems (based on

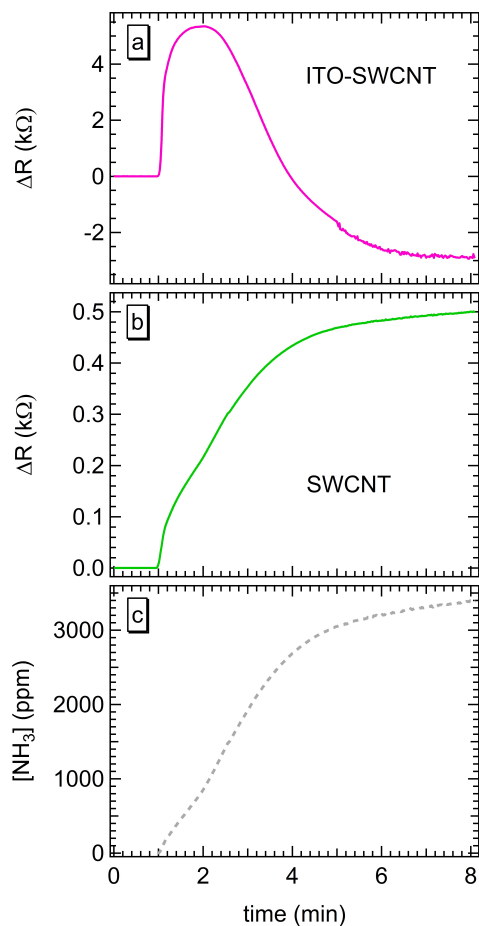


**Figure 4.23:** ITO-SWCNT (a) and SWCNT (b) sensor response to high (up to 3400 ppm) ammonia concentrations (c). Exposure starts at  $t = 1$  min.

SWCNT and hybrid ITO-SWCNT layers) to  $\text{NH}_3$ ,  $\text{H}_2\text{O}$  and  $\text{NO}_2$  gases. We will take into consideration the impact of donor surface states (effect of reducing molecules, like  $\text{NH}_3$  and  $\text{H}_2\text{O}$ , adsorbed on the surface, also at high concentrations) or acceptor surface states ( $\text{O}_2$  and  $\text{NO}_2$  effect) on the electronic band and

space-charge regions of a p-n nano-heterojunction. Combining the modeling of Sharma *et al.* [81] and Woo *et al.* [109], in Fig. 4.24 the ITO-SWCNT sample is sketched, on the basis of AFM (Fig. ?? b) and SEM images (Fig. 4.6 b), as composed by a SWCNT bundle with a diameter  $d \approx 30$  nm, covered by ITO nanoparticles with a diameter  $d \approx 50$  nm. Consistently with Sect. 4.2, the ITO-functionalized sample in air can be depicted as in Fig. 4.24 a. The oxygen molecules of the atmosphere (as acceptor surface states), adsorbed on the sample surface, originate a depletion layer (green area) at the n-type ITO nanoparticle surface, while at the p-type SWCNT bundle, where the hole current is supposed to flow (red arrows), an accumulation region (red area) is built-up. The blue area represents the depletion region due to p-n nano-junction.

Now, let's start to analyze the SWCNT and ITO-SWCNT sensors response to ammonia gas. The series of measurements in air and in the gas testing chamber show that both samples (SWCNT and ITO-SWCNT) increase their resistance when exposed to  $\text{NH}_3$ . In terms of band bending, it is well known that a reducing molecules such as  $\text{NH}_3$  (or  $\text{H}_2\text{O}$ ,  $\text{CO}$ , etc.) [96] acts lowering the band banding and, as a result, also the depletion region is reduced (as shown in Fig. 4.24 b). At the SWCNT bundle surface, the accumulation region is also reduced, yielding a decrease of the hole current (i.e. an increase of resistance), as we observed, for example, in Fig. 4.13 or Fig. 4.15.

Water vapor has the same effect of ammonia, but at high concentrations an inversion layer is established (see Fig. 4.10 and related discussion), the majority carriers turn from holes into electrons and a n-type response to  $\text{H}_2\text{O}$  (i.e. a decrease in the resistance) occurs, as observed in Fig. 4.17.

With the p-n junction sensing modeling, we can also justify the ITO-SWCNT response to  $\text{NO}_2$ , which otherwise would not have explanation, by considering only the SWCNT DOS. The  $\text{NO}_2$  effect is to expand the accumulation region in p-type SWCNT, resulting in an increase of holes. However, if that were the only effect to take into account during the gas-surface interaction, then an increase of current (i.e. a decrease in the sample resistance) would occur, in contrast with what we observed in Fig 4.18. The only possible reason is that in the case of  $\text{NO}_2$  the *junction effect* is dominant with respect to the *adsorbed molecule effect*. In fact, besides increasing holes in SWCNT bundle,  $\text{NO}_2$  causes the expansion of the depletion region in the n-type ITO nanoparticles (Fig. 4.24 c) that affects the p-n junction depletion region which may extend into the p-type

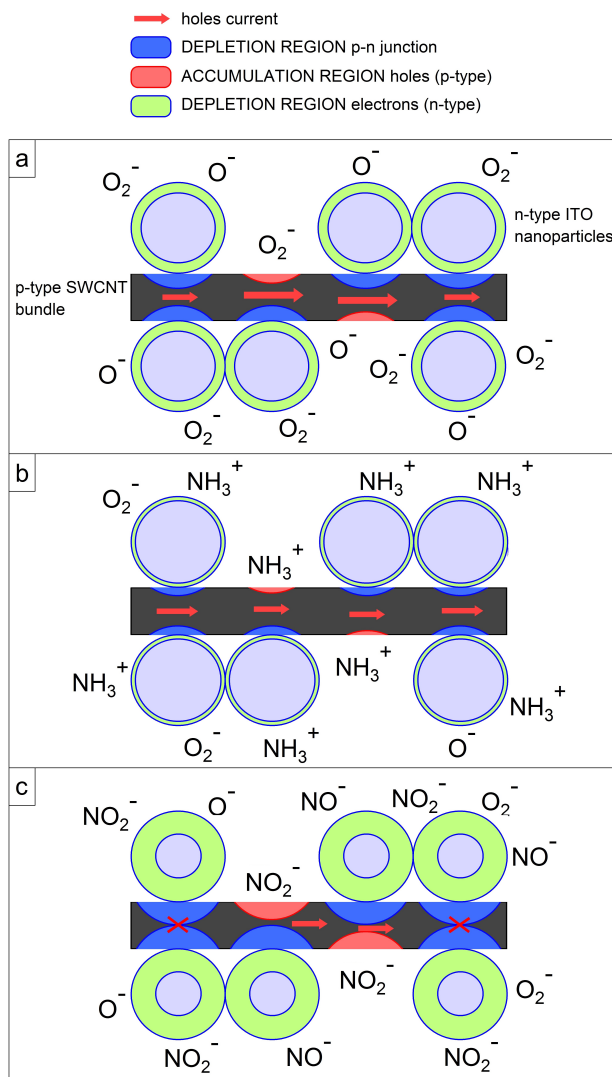


**Figure 4.24:** Sketch of the ITO-SWCNT sample (a) in air with oxygen molecules adsorbed on its surface; (b) reducing  $NH_3$  effect; (c) oxidizing  $NO_2$  effect.

bundle up to create a gate-like effect for the hole current.

## 4.4 Conclusions

Single-walled carbon nanotube pristine layers and functionalized with metal oxide nanoparticles, deposited on plastic substrates and operating at room temperature, have been used to detect ammonia gas in low-ppb concentrations, water vapor and nitrogen dioxide. A detection limit of 13 ppb for  $\text{NH}_3$  is demonstrated and an increase of sensitivity upon functionalization is achieved, at least for ammonia concentrations above 200 ppb. The role of functionalization with ITO nanoparticles becomes much more relevant in the detection of other interfering gases, as ITO-SWCNTs sample shows an opposite resistance variation, with respect to pristine SWCNTs sample, when exposed to  $\text{NO}_2$  and water vapor, disclosing the possibility to discriminate the effect of interfering gases signal in the ammonia detection. Gas sensing mechanism, based on hole compensation effects in SWCNT density of states and on space-charge in p-n junction, has been discussed. With respect to the pristine layer, the ITO-SWCNT blend also displays a shorter recovery time and higher selectivity (i.e. lower sensitivity) towards acetone and ethanol. In perspective, the present result makes the SWCNT-based chemiresistor gas sensor quite interesting to produce low cost, high sensitivity, chemiresistor gas sensors for environmental monitoring of sub-ppm ammonia concentrations. The low detection limit (i.e. less than 20 ppb) required for a realistic monitoring of ammonia environmental pollution is achieved, and the problem of the sensing layer poisoning upon exposure to low  $\text{NO}_2$  concentration is tackled by considering the effects of UV irradiation.



## Chapter 5

# Hybrid nanoarchitectures

Nanostructured materials constitute a very interesting class of systems with a large field of technological applications, e.g. batteries, fuel cells, super capacitors, etc.. They are also well known as suitable materials to be used as gas sensors, especially because of the high surface-to-volume ratio. These exceptional qualities could be improved when they are mixed in hybrid systems [113–119], produced by novel synthesis techniques which enable to control the architecture of many materials at the nanoscale level, in order to enhance the sensitivity, selectivity and stability of sensor devices. In fact, from an environmental monitoring point of view, the aim is to develop highly sensitive, selective, fast responsive, low cost and portable sensors with low power consumption. In this chapter we report on simple, scalable, template-based synthesis processes, which can be employed to produce hierarchical nanostructured hybrid architectures.

### 5.1 C nanostructured on aligned ZnO nanorods

We now present zinc oxide nanorods (ZnO NRs) and carbon nanostructures (CNs) grown by chemical vapor deposition (CVD) on ZnO NRs, which have been prepared, characterized and tested as chemiresistor gas sensors upon exposure to polluting gases, in particular, to ammonia gas. Actually, the growth of these materials is not yet well controlled and understood, and only few works are reported, mainly regarding ZnO grown on CNTs [72, 116–118]. Following

Ref. [120], recent papers have also used ZnO as template for the synthesis of carbon nanotubes and nanostructures [121, 122].

### 5.1.1 Catalyst-free CVD

The samples were prepared by P. Mbuyisa [120] controlling at different temperatures the  $C_2H_2$  CVD on vertically aligned ZnO NRs, which were synthesized starting from a ZnO film deposited by DC magnetron sputtering deposited on Si(110) substrate. The ZnO NRs were obtained by using a hydrothermal pro-

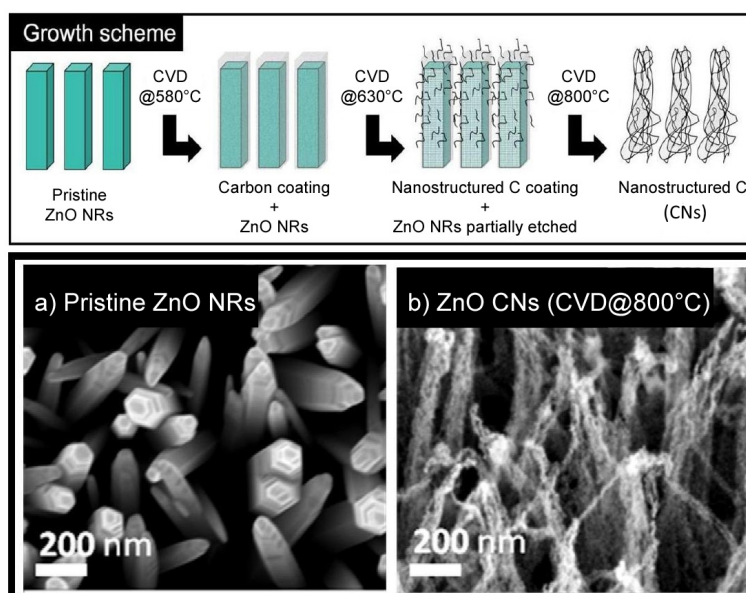
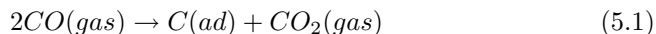


**Figure 5.1:** TOP PANEL: growth scheme at different CVD temperatures (the green pillars represent the pristine ZnO NRs, light grey represents C coating, which at high temperature organizes in carbon nanostructures (CNs)). BOTTOM PANEL: SEM images of (a) ZnO nanorods and (b) ZnO NRs after CVD@800°C. Samples prepared by P. Mbuyisa. Figure adapted from [120].

cess, which is a simple and inexpensive process yielding to have homogeneous samples [123]. All the CVD processes were carried out for 5 minutes using a 50 sccm flux of  $C_2H_2$ . The sample was positioned perpendicular to the acetylene

gas nozzle at a distance of 2 cm (see Ref. [120] for more details). The typical morphology of the NRs is shown in the SEM image of Fig. 5.1 a. The NRs are about 1  $\mu\text{m}$  in length and are preferentially vertically aligned on the substrate. They are characterized by a pointed hexagonal shape at the tips, and have a large diameter distribution in the 50-200 nm range. Fig. 5.1 (top panel) summarizes the growth mechanism induced by CVD at different temperatures: the carbon coating of the ZnO NRs after CVD at relatively low temperatures, i.e. 580°C, starts to organize in carbon nanostructures (CNs) as the CVD temperature grows up  $\approx 630^\circ\text{C}$ ; at higher temperatures, i.e. 800°C, most of the ZnO is etched and CNs remains on the sample surface. The carbon nanostructures synthesized at different temperatures are the competing results of different phenomena, i.e. carbon deposition, ZnO etching and sublimation of by-products through the CNs. The weight of these phenomena strongly depends on the process temperature, determining the final nanostructuration. Actually, at a certain temperature, the  $\text{C}_2\text{H}_2/\text{ZnO}$  NRs reaction products include two terms: those due to  $\text{C}_2\text{H}_2$  self decomposition and those due to the catalytic reaction occurring between  $\text{C}_2\text{H}_2$  and the ZnO NRs surface.  $\text{C}_2\text{H}_2$ , used in the process, decomposes to carbon and hydrogen above 700-800°C [124], but it dissociates on ZnO surfaces at 400-500°C, forming adsorbed carbon and decomposition products, which include CO,  $\text{CO}_2$ ,  $\text{H}_2\text{O}$  and Zn, as revealed by thermal desorption and XPS experiments [125]. During CVD these products are in the gas phase (Zn vapor pressure is larger than 1 mbar at 500°C); in addition, the presence of CO implies the formation of further adsorbed (ad)carbon through the following reaction [119]:



These observation explain the formation of the carbon coating and the etching of the ZnO NRs observed in XPS, SEM and Raman at temperature below 700°C. At higher temperature, the  $\text{C}_2\text{H}_2$  self decomposition becomes more important, leading to a massive deposition of amorphous carbon and to a more prominent etching of the ZnO NRs. The volatile by-products (Zn,  $\text{H}_2\text{O}$ , CO,  $\text{CO}_2$ ) desorb through the carbon coating defects and imply a further reorganization of the carbon close to the ZnO NRs shell, forming the short one-dimensional CNs observed on the NRs at temperatures from 740°C. At higher temperatures (800-830 °C) these phenomena are more evident and important.

Phase contrast HRTEM experiments were performed to reveal the fine details of

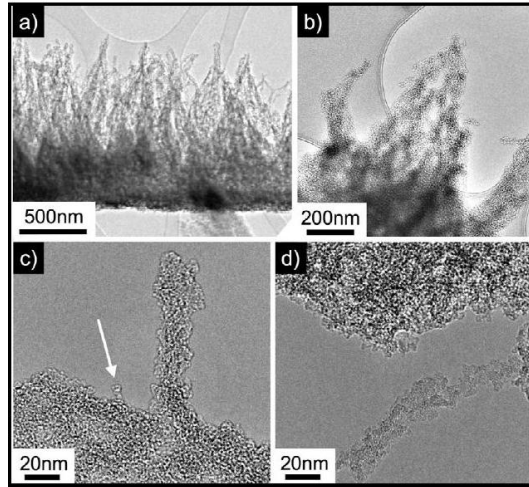


**Figure 5.2:** High Resolution Transmission Electron Microscopy images of the sample after CVD at  $800^{\circ}\text{C}$  show a high surface-to-volume ratio and a dendritic porous nature of the carbon nanostructures [120].

the CNs grown at high temperature. The grown material was gently scratched using a small blade and deposited onto a carbon-coated copper grid. This procedure did not change the main structure of the CNs, as shown in the low magnification image of Fig. 5.2, which is compatible and very similar to the SEM images acquired onto the same sample before scratching (see Ref. [120] for more details). HRTEM of Fig. 5.2 shows how the CVD process at  $800^{\circ}\text{C}$  induces the formation of CNs with a high surface-to-volume ratio as made of porous carbon from which start to elongate several thin carbon filaments. The porous carbon is located at the interface with the Si support, as shown in the low magnification image of Fig. 5.2 a, and its structure is very similar to a sponge (the elongated CNs have a dendritic porous nature).

The Raman spectrum of the as-grown ZnO nanorods (Fig. 5.3 left, bottom) clearly shows a peak at  $435\text{ cm}^{-1}$ , assigned to the  $E_2$  optical phonon mode, which is a characteristic Raman peak for the ZnO wurtzite hexagonal phase [126]. A weak peak in the Raman spectrum at  $\approx 579\text{ cm}^{-1}$ , attributed to the  $E_{1L}$  mode, is also observed, which indicates the presence of structural defects (oxygen va-

cancies, zinc interstitial and free carriers) and impurities [126]. The presence of the peak at  $435\text{ cm}^{-1}$  indicates that the ZnO core structure of the NRs is still preserved. It is also rather interesting to observe that in the region between the D and G bands, the spectral weight is not flat but a broad band is detectable, peaked at about  $1426\text{ cm}^{-1}$ . We tentatively ascribe this band either

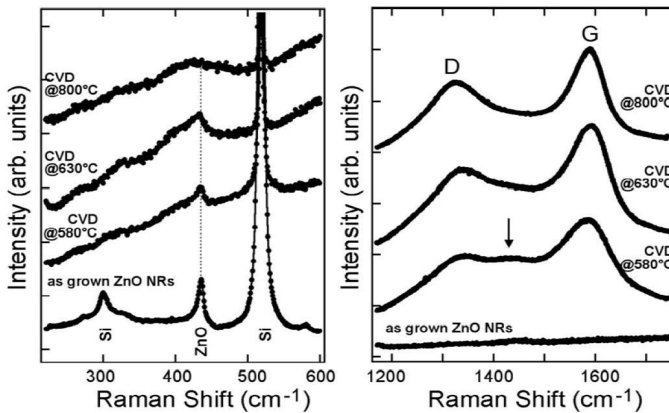


**Figure 5.3:** Raman spectra of the as grown ZnO NRs and after CVD carried out at different temperature in the  $200\text{--}600\text{ cm}^{-1}$  (left) and  $1150\text{--}1750\text{ cm}^{-1}$  (right) range. All spectra are normalized to the G-band maximum, except the as grown ZnO NRs [120].

to a contribution of a ZnCO phase at the ZnO NRs-carbon overlayer interface or to some residual carbon-based contaminations that are ultimately desorbed or decomposed after annealing at high temperatures. By increasing the CVD temperature to 630 and  $740^\circ\text{C}$ , the carbon intensity increases by a factor 2 and 4, respectively, and the ZnO etching process become more prominent. This is clearly seen in the SEM images of Fig. 5.1 b showing the growth of several one-dimensional CNs (with lengths  $< 100\text{ nm}$  and diameters  $< 5\text{ nm}$ ) on the ZnO NRs. At the same time the Raman D and G modes (Fig. 5.3, right) sharpen, implying a higher degree of order, which may be due to atoms reorganization as also seen in the SEM images. In addition the band at  $1426\text{ cm}^{-1}$  decreases in intensity, consolidating the hypothesis that it is due to carbon-based contaminations. We remark that in this temperature range the pristine ZnO NRs structure is preserved, as confirmed by the presence of the ZnO  $E_2$  Raman-active mode,

even if it is further decreased in intensity and broadened, indicating higher disorder. The etching and the chemical effect of the CVD process at these temperatures are easily and better revealed by XPS, which shows the appearance of the signals of the  $\text{SiO}_2$  substrate used as support for the ZnO NRs synthesis. In Fig. 5.4, XPS spectra of the O 1s, C 1s and Zn  $2p_{3/2}$  are shown. From bottom to top: ZnO NRs before and after annealing at 630 °C and after CVD at different temperatures (580, 630, 710, 800°C). In the O 1s spectra (Fig. 5.4 a): the asymmetry in the ZnO NRs is due to the peak at 530 eV (ZnO) and at 532.6 eV (C=O bound, reduced after annealing). After the CVD, a component at 533 eV appears ( $\text{SiO}_2$  from the substrate), showing an etching of the ZnO surface. The C 1s spectra (Fig. 5.4 b) show the peak at 284.5 eV (graphitic carbon) disappears after the annealing and it reappears after the CVD because of the interaction of ZnO with  $\text{C}_2\text{H}_2$  (the peak increases with the temperature). The asymmetry is due to a second peak at 286.6 eV (C=O bond) that decreases with temperature. Finally, in the Zn  $2p_{3/2}$  spectra (Fig. 5.4 c) the attenuation of the peak with increasing CVD temperature confirms a strong ZnO etching (no more Zn is detected after CVD at 800 °C). The strong ZnO etching is further confirmed by the observed strong attenuation of the Zn photoemission signal, as the temperature of the deposition process increases (more details in the XPS

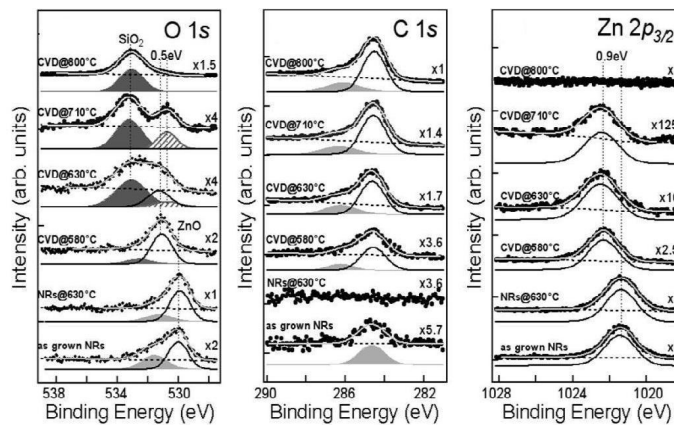


**Figure 5.4:** XPS spectra of the O 1s, C 1s and Zn  $2p_{3/2}$  are reported. From bottom to top: ZnO NRs before and after annealing at 630 C and after CVD at different temperatures [120].

analysis can be found in Ref. [120]). XPS, HRTEM and Raman measurements carried out after CVD at 800°C show that the resulting sample presents filamentous carbon on the pristine ZnO NRs, which are completely etched (Fig. 5.1b). In particular, the Raman spectrum taken on the samples treated at these temperatures (800°C), shows that the D and G modes became sharper, supporting the CNs reorganization with a higher degree of order.

### 5.1.2 Fe catalyst-assisted CVD

With a methodology similar to that described in the previous section, further samples were also prepared by iron catalyst-assisted CVD. The iron catalyzed growth was carried out by P. Mbuyisa [127] using a Fe film of about 0.7 nm to

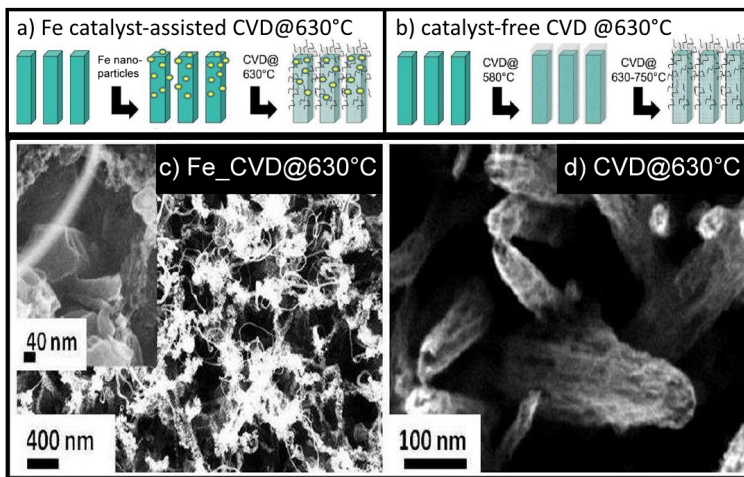


**Figure 5.5:** Growth scheme of Fe-assisted CVD@630°C (a) and catalyst-free CVD@630°C. SEM images of the two samples are reported, respectively in (c) and (d). Samples prepared by P. Mbuyisa [127].

act as the catalyst. The thin film of Fe was deposited using iron thermal evaporation on ZnO NRs.  $C_2H_2$  Chemical Vapor Deposition (CVD) carried out with and without iron catalyst allowed to synthesize different carbon nanostructures. From SEM images (Fig. 5.5, bottom panel) we can observe that in comparison with the CVD growth without catalyst (Fig. 5.5 d), which leads to a partial

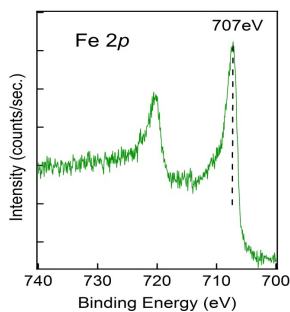


**Figure 5.6:** XPS spectra of the Fe 2p level of 0.7 nm Fe deposited on the ZnO NRs, showing the Fe in its metallic state which is its catalytically active state in the CNTs growth via CVD.

etching of the ZnO NRs after CVD at 630°C, the Fe catalyst assisted CVD at 630°C (Fig. 5.5 c) seems to produce more carbon nanostructures (similar to carbon nanotubes) on the nanorods. The in-situ XPS (Fig. 5.6), acquired

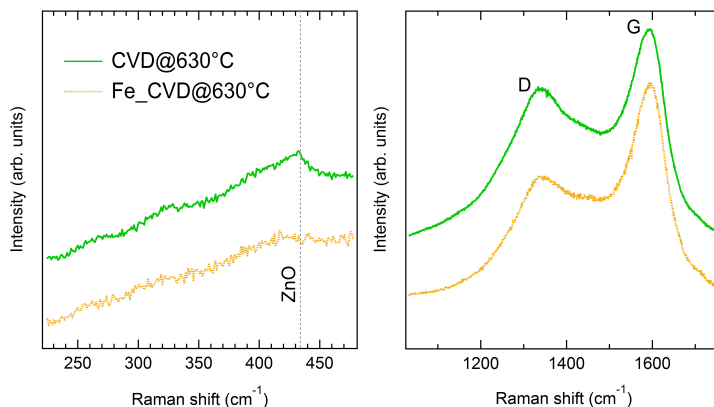


**Figure 5.7:** Raman spectra measured on the sample prepared at 630°C with catalyst-free CVD (solid green line) and Fe catalyst-assisted CVD (yellow dotted line). Left panel: low wavenumber region with the ZnO  $E_2$  mode at  $\approx 435$   $\text{cm}^{-1}$ . Right panel: high wavenumber region with carbon related D and G Raman bands (the spectra are normalized to the G-band maximum).

after Fe deposition and before CVD, showed that Fe-ZnO interaction is weak.



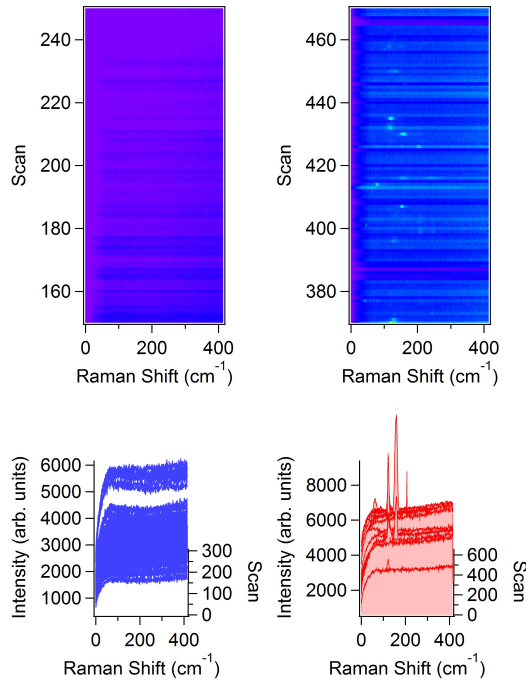


**Figure 5.8:** Micro-Raman sampling, where the RBM modes at low wavenumbers are detectable in the Fe.CVD@630 °C (right panel) sample but not in the CVD@630 °C sample (left panel). The sampling was carried out on a representative mesh of 676 points, spanning a surface of about  $20 \times 10 \mu\text{m}^2$ .

The Fe  $2p_{3/2}$  is found at  $\sim 707$  eV and the shape of the peak reveal Fe in its metallic state (no oxidation is detectable in Fe 2p XPS spectra [128]), which is its catalytically active state in the CNTs growth via CVD. In Fig. 5.7 the Raman spectra of the samples grown at  $630^\circ\text{C}$  with Fe catalyst (Fe.CVD@ $630^\circ\text{C}$ ) and after CVD with no catalyst at  $630^\circ\text{C}$  (CVD@ $630^\circ\text{C}$ ) are shown. In the low wavenumber region (Fig. 5.7, left panel) the peak at  $\approx 435 \text{ cm}^{-1}$  (characteristic for the ZnO wurtzite hexagonale phase) is observed for sample grown without catalyst (green solid curve), while it is almost totally reduced in the sample after Fe catalyst-assisted CVD at  $630^\circ\text{C}$  (yellow dotted curve). This suggests a better covering of the ZnO by the carbon nanostructures (unless ZnO has started

to disappear at high temperatures as we discussed in the previous section and in Ref. [120]). In the high wavenumber region, the typical D and G modes of carbon at  $1330\text{ cm}^{-1}$  and  $1595\text{ cm}^{-1}$  respectively are clearly detectable. According to the large bandwidth, disorder effects are not negligible but the  $I_D/I_G$  ratio suggests the presence of more ordered carbon nanostructures in the sample prepared with Fe catalyst assisted CVD at  $630^\circ\text{C}$ . Indeed, the  $I_D/I_G$  ratio is 0.57 and 0.72 for the sample grown with Fe catalyst and without catalyst, respectively, indicating more ordered structures in the former sample. In Fig. 5.8 a micro-Raman sampling, carried out on a representative mesh of 676 points and spanning a surface of about  $20 \times 10\ \mu\text{m}^2$ , is shown. The RBM modes at low wavenumbers are detectable in the Fe-CVD@ $630^\circ\text{C}$  sample but not in the CVD@ $630^\circ\text{C}$  sample.

### 5.1.3 Gas sensitivity

To investigate the potential application of the CNs/ZnO hybrid system, we analyzed the capability to detect ammonia and acetone in ambient conditions of one hybrid structure grown at  $800^\circ\text{C}$ , and we compared its response to that of the as-grown ZnO NRs. Fig. 5.9 compares the time dependent variation  $\Delta R$  of the resistivity of the pure ZnO NRs (blue) and of the CNs/ZnO hybrid grown at  $800^\circ\text{C}$  (green) while they are exposed to ammonia and acetone. The time exposure to gases is displayed at the bottom of Fig. 5.9. The samples were exposed to 2.3, 3.3 and 28.5 ppm of ammonia and to high concentration ( $>30$  ppm) of acetone (Fig. 5.9, from left to right) for three minutes. The response of the ZnO NRs to ammonia and acetone is consistent with results already present in literature [129, 130]. Actually the CNs-coated sample presents a much higher response to ammonia with respect to the uncoated nanorods. The response to ammonia, defined as  $\Delta R/R_0 = (R_s - R_0)/R_0$  ( $R_0$  is the resistivity prior to exposure,  $R_s$  upon to exposure), of the CNs/ZnO hybrid is increased by a factor 4.5 with respect to the ZnO NRs case (see Table 5.1). It should be noted that the recovery time after the exposure to ammonia is rather slow, but the measurements have been carried out at room temperature and a faster recovery is expected when this kind of structures are heated or exposed to ultra-violet light [13]. After exposure to acetone ( $>30$  ppm), the uncoated sample shows a negative resistivity variation, while the resistivity of the carbon-coated sample

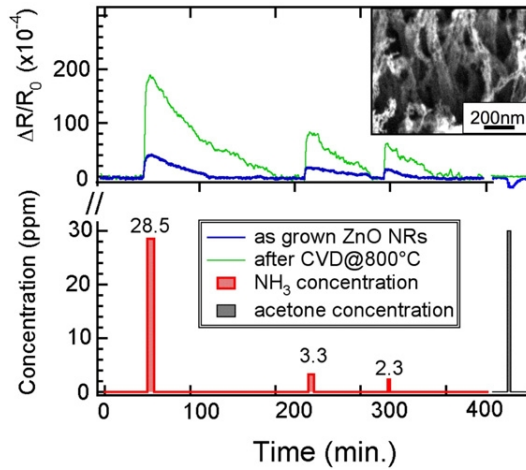


**Figure 5.9:** Response of the as grown ZnO (blue line) and of the sample grown at 800 °C (green line) upon exposure to 28.5, 3.3, 2.3 ppm of  $\text{NH}_3$  and >30 ppm of acetone. The inset (top right) shows SEM after CVD@800°C [120]. RH=31±1%, T=25±0.5°C during the measurements.

[ $\text{NH}_3$ ] (ppm)	A (ZnO response)	B (ZnO+CNs response)	ratio A/B
28.5	4	19	4.75
3.3	2	9	4.50
2.3	1.5	6.5	4.33

**Table 5.1:** A and B are the sensor responses at the 3 different ammonia concentrations reported in the first column: A=  $\Delta R/R_0 (\times 10^{-3})$  uncoated ZnO; B=  $\Delta R/R_0 (\times 10^{-3})$  ZnO+CNs; in the last column the ratio of the two response is reported: A/B =  $(\Delta R/R_0)_{\text{ZnO+CNs}} / (\Delta R/R_0)_{\text{ZnO}}$ . The  $\Delta R/R_0$  was measured at 25.5°C (0.5°C) with a relative humidity R.H. = 31% 1%. [120].

does not show detectable variations. Therefore, with respect to the uncoated nanorods, the carbon coating enhances both the sensitivity towards ammonia and the selectivity with respect to possible interfering gases such as acetone vapors. The system grown at 800°C, therefore, behaves mainly as a carbon based material, like for example CNTs, having a rather weak interaction with acetone and an enhanced sensitivity to  $\text{NH}_3$  [131].

In Fig. 5.10, the response curve ( $\Delta R/R_0$  versus ammonia concentration) of the

samples grown at 630°C with and without Fe catalyst (Fe\_CVD@630°C yellow diamonds, CVD@630°C green squares) is reported, compared with response of other two samples discussed also in the previous section: carbon nanostructures grown on ZnO nanorods at 800°C (CVD@800°C, red circles) and bare ZnO nanorods (ZnO NRs, blue triangles). The sample grown with Fe catalyst

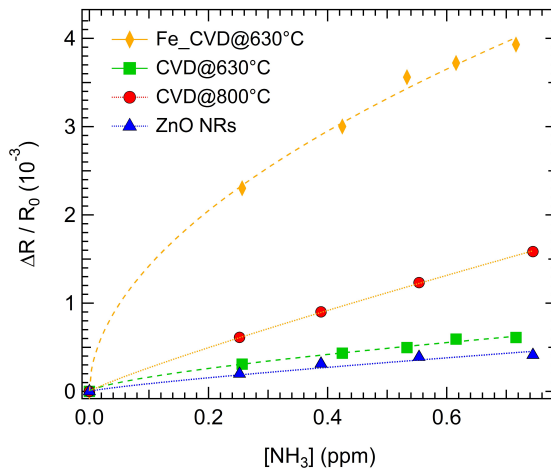


**Figure 5.10:** Response ( $\Delta R/R_0$ ) versus ammonia concentration of the four samples tested as  $\text{NH}_3$  gas sensors. The relative humidity and temperature values during the measurements were  $\text{RH}=32\%$  and  $T=26^\circ\text{C}$ .

at 630°C shows the higher response with respect to the other samples tested. However, by taking the signal noise and the parameters of the power-law fit in order to calculate the detection limit for this best-response sensor, we obtain a DL of 80 ppb. (The DL has been calculated with the formula  $\frac{5\sigma}{R_0} = A \cdot (DL)^p$ , as we discussed in chapter ??, with the following values:  $\sigma = 0.03 \Omega$ ,  $R_0 = 265 \Omega$ ,  $A = (2.17 \pm 0.05) \times 10^{-3}$ ,  $p = 0.53 \pm 0.04$ ). The DL below 100 ppb makes the present hybrid materials promising candidates to develop and engineer gas sensing devices for ammonia detection.

Raman results (Fig. 5.7) show that in the Fe\_CVD@630°C sample there are less defects, but this sample appears to be the most sensitive to ammonia gas (Fig. 5.10). This could be explained considering the presence of more CNT-like

structures as can be retrieved from SEM image of Fig. 5.5 c. This is confirmed by an extensive micro-Raman mapping (Fig. 5.8) on the Fe\_CVD@630°C and CVD@630°C samples where low wavenumber radial breathing modes (RBM) characteristic of SWCNT have been occasionally detected in the Fe\_CVD@630°C, but not in the CVD@630°C sample. In this frame, the higher sensitivity to ammonia is ascribed to a better charge transport provided by CNTs in the Fe\_CVD@630°C sample. The reactivity towards other gases (acetone, ethanol and nitrogen dioxide) was tested on the sample grown with iron catalyst at 630°C which is the most sensitive to ammonia gas. The results are shown in

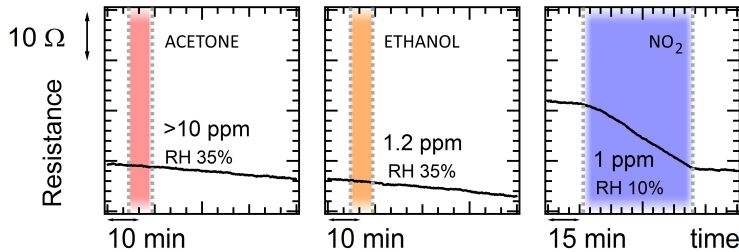


**Figure 5.11:** Fe\_CVD@630°C sensor response to acetone, ethanol (to which no response is recorded) and nitrogen dioxide (that induce a resistance decrease as expected from the interaction with an oxidizing gas). After NO<sub>2</sub> exposure no recovery was observed, suggesting a strong chemisorption.

Fig. 5.11. No sensitivity was observed to slightly reducing gases like acetone and ethanol (the present measurements were done in lab air conditions and the relative humidity and temperature values during the measurement were: RH=35%, T=27 °C). However, a response to 1 ppm of NO<sub>2</sub> was observed ( $\Delta R/R_0 = -0.012$ , resulting in a sensitivity  $(\Delta R/R_0)/[\text{NO}_2] = 0.012 \text{ ppm}^{-1}$ ). This latter exposure was carried out in the sealed testing chamber with RH=10% and T=28 °C.

## 5.2 Tubular Sn-filled carbon nanostructures on ITO

Indium tin oxide (ITO) is a conductive oxide, widely used as transparent electrode in many applications, e.g. photovoltaic applications in organic solar cells [132], liquid crystal display [133], antireflection coatings in organic light emitting diode [134] and radiation protection [135]. Little attention has been paid so far to ITO nanostructures as gas sensor material. In a recent paper, L. D’Arsié *et al.* show a new method to obtain nanostructured  $\text{SnO}_x$  on ITO using CVD with  $\text{C}_2\text{H}_2$  as reagent gas [136]. This constitutes a new promising procedure to develop energy generation and storage electrodes or chemical sensors with improved efficiency.

### 5.2.1 Sample preparation and characterization

The method to obtain nanostructured ITO, sketched in Fig. 5.12 a, consists in three steps: first, before the growth, the substrate of ITO on glass was heated at 940 K in a vacuum chamber ( $10^{-6}$  mbar) and then exposed to 1 mbar of  $\text{H}_2$  for 10 min; second, vertical nanostructures was obtained by exposing the ITO/glass

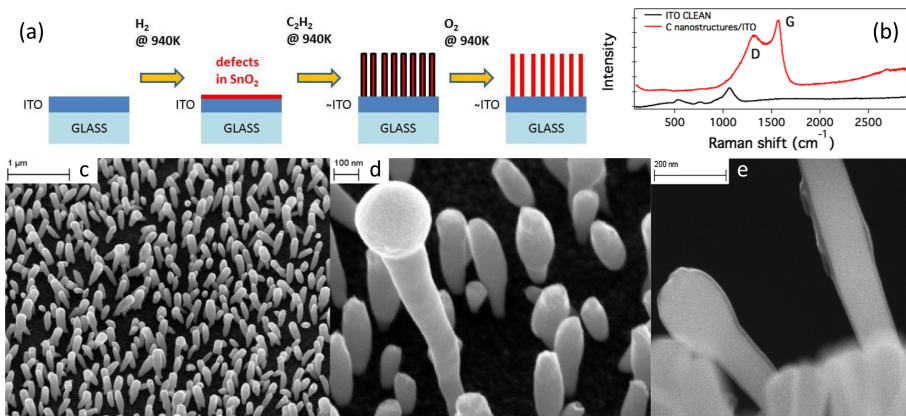


**Figure 5.12:** Growth scheme (a), Raman spectra (b) and high-resolution SEM images (c-e) of carbon nanostructures grown on ITO/glass at  $940 \pm 10$  K (“NS ITO” sample). Sample prepared by L. D’Arsié *et al.* Figure adapted from Ref. [136].

substrates heated at  $940 \pm 10$  K to acetylene gas  $C_2H_2$  at a pressure of 30 mbar for 5 min; and finally the sample was heated in  $O_2$  atmosphere at 940 K in order to burn the carbon coverage [136]. From XPS analysis, D’Arsié *et al.* showed that the hollow carbon structures vertically grown on ITO surface were filled by  $SnO_2$  (Fig. 5.12 e). Then, after the exposure to  $O_2$  atmosphere at 940 K, the carbon coverage is removed by pyrolysis and vertical nanopillars of tin oxide are left on the sample surface. We refer to this first sample of  $SnO_x$  nanostructures on ITO substrate as “NS ITO” sample.

Two other samples were prepared by the method described above, following the first two steps of the growth scheme of Fig. 5.12 a, i.e. the substrate of ITO on glass was heated at 940 K in a vacuum chamber, then exposed to 1 mbar of  $H_2$  for 10 min and to  $C_2H_2$  gas at  $P = 30$  mbar for 5 min. At a later stage, the samples have been annealed in a oven at 940 K for 15 minutes at atmospheric pressure. SEM images of these two samples, which we call “NS ITO a” and “NS ITO b”, are shown in Fig. 5.13. As can be observed from

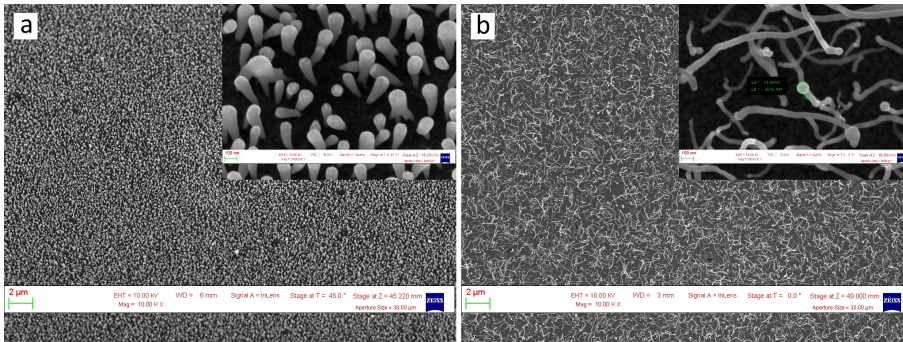


**Figure 5.13:** SEM images of (a) “NS ITO a” and (b) “NS ITO b” samples, prepared following the first two steps of the growth scheme of Fig. 5.12 a and then annealed in an oven at 940 K for 15 minutes at atmospheric pressure. SEM images have been taken before the annealing.

SEM images, tubular vertical nanopillars cover the “NS ITO a” sample surface, while in the “NS ITO b” sample nanostructures are stretched out on the surface. In Fig. 5.14 Raman spectra of “NS ITO a” and “NS ITO b” samples, before and after the annealing, are shown. The D and G modes, typical of carbon materials, disappear after the annealing, confirming the pyrolysis of the carbon that covered the  $SnO_x$  nanostructures. The large band width of the peaks in

Fig. 5.14 (left panel) show that the tin nanopillars, before the annealing, are covered by an amorphous carbon skin.

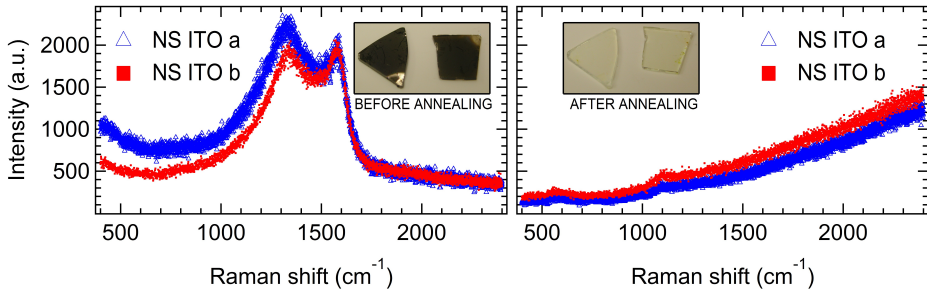


**Figure 5.14:** Raman spectra of “NS ITO a” (blue empty triangles) and “NS ITO b” (red filled squares) samples before (left panel) and after (right panel) the annealing in an oven at 940 K for 15 minutes at atmospheric pressure. In the insets, pictures of the samples before and after the annealing are reported: “NS ITO a” sample are on the left and “NS ITO b” sample on the right of each picture.

## 5.2.2 Gas sensitivity and response time

The samples based on carbon/tin oxide nanostructures on ITO substrate have been tested as chemiresistor gas sensors with the set-up for gas sensing measurements reported in chapter 2. For the electrical contacts two metal clips fixed on the sample surface have been used (in a second moment we put two stripes of Ag paste on the edges of the sample, but this did not improve the sensitivity to gases). In order to compare the response between the NS ITO sample and the commercial CGS Figaro2602, the resistance variation upon exposure to 30 ppm ammonia for 3 minutes is reported in Fig. 5.15 (top panel). The  $R_0$  of the NS ITO is around 286 k $\Omega$  before gas exposure. The signal during the recovery time has been fitted with a double exponential curve, obtaining the following decay time:  $\tau_1=(51.8\pm 0.6)$  s,  $\tau_2=(403\pm 2)$  s for the commercial CGS Figaro2602, and  $\tau_1=(3.5\pm 0.2)$  s,  $\tau_2=(57\pm 2)$  s for the NS ITO sensor. The fluctuations on the top of the curve during exposure and the signal noise are reported respectively in the inset (a) and (b) of Fig. 5.15 (top panel). In particular, the signal noise results  $\sigma \approx 36 \Omega$ . In the inset (c) of Fig. 5.15 (top panel)



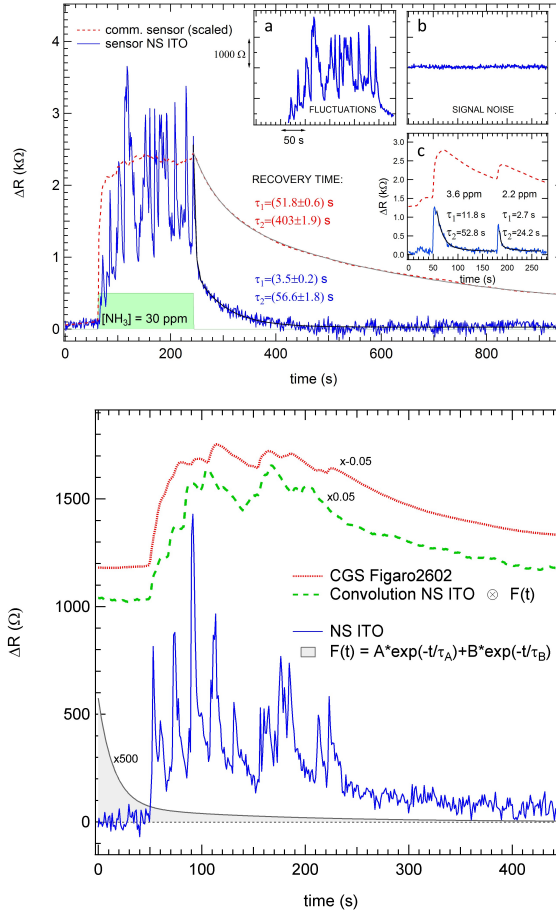


**Figure 5.15:** TOP PANEL: nanostructured tin oxide on ITO (NS ITO) sample response (blue solid curve) to 30 ppm ammonia exposure, compared to the response of the commercial CGS Figaro2602 (red dashed curve). Fluctuations on the top of the curve during gas exposure are reported (inset a), compared to noise (inset b). In the inset (c) a couple of peaks after ammonia concentration variations of 3.6 and 2.2 ppm are reported. BOTTOM PANEL: commercial metal oxide CGS Figaro2602 resistance (red dotted line) compared with the convolution (green dashed line) of the signal from NS ITO based sensor (blue line) with  $F(t) = A \exp(-t/\tau_A) + B \exp(-t/\tau_B)$  (grey-filled to zero line).

a couple of peaks after exposure to ammonia concentration of 3.6 and 2.2 ppm are shown. The fast recovery of NS ITO allows to have two distinct peaks, while the commercial CGS did not fully recover before the second ammonia exposure. We highlight the fact that the commercial CGS Figaro2602 is heated at 150°C, while the NS ITO operates at room temperature.

In order to evaluate the different response times between the two sensors, we performed a convolution of the NS ITO signal with a double exponential function ( $y = A e^{-\frac{t}{\tau_A}} + B e^{-\frac{t}{\tau_B}}$ ), reported in Fig. 5.15 (bottom panel). The fit parameters are:  $A = 1$ ,  $\tau_A = 15$  s,  $B = 0.15$ ,  $\tau_B = 150$  s. The peculiarity of “NS ITO” sensor is the very fast recovery time after the interaction with ammonia gas. As observed and discussed in chapter ??, the signal fluctuations on top of

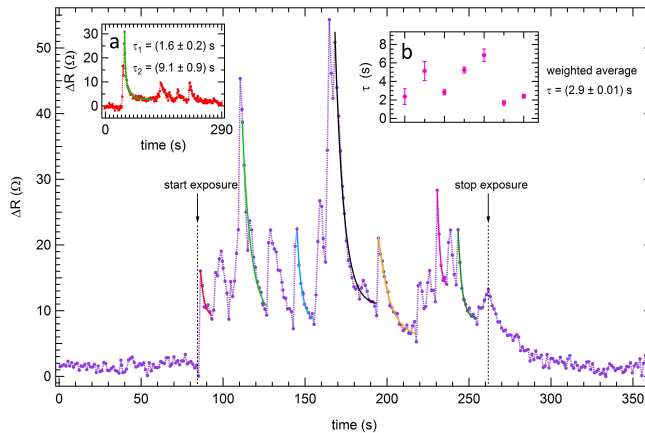


**Figure 5.16:** Examples of fitting with exponential curve to obtain the decay time of signal fluctuations on top of the curve during gas exposure. Inset a: example of isolated peak with decay fitted with double exponential curve. Inset b: decay time values and weighted average ( $2.90 \pm 0.01$  s).

the curve during gas exposure have their own characteristic time for signal rise and decay (we observed a step-rise time and a recovery time of few seconds for this sample). The decay time of some fluctuations has been evaluated by single exponential fitting (Fig. 5.16), obtaining an average decay time of  $2.90 \pm 0.01$  seconds.

The sensor response to ammonia gas of the samples “NS ITO a” and “NS ITO b”

before and after the annealing in an oven at 940 K at atmospheric pressure have also been tested and are shown in Fig. 5.17. The resistance value of the “NS ITO a” sample is around 235  $\Omega$  and 1630  $\Omega$ , before and after the annealing respectively; while the “NS ITO b” resistance is higher before the annealing, around 3200  $\Omega$  (maybe due to the contacts between the tubular structures stretched on the surface), and it increases after the annealing, around 4790  $\Omega$ . Before the

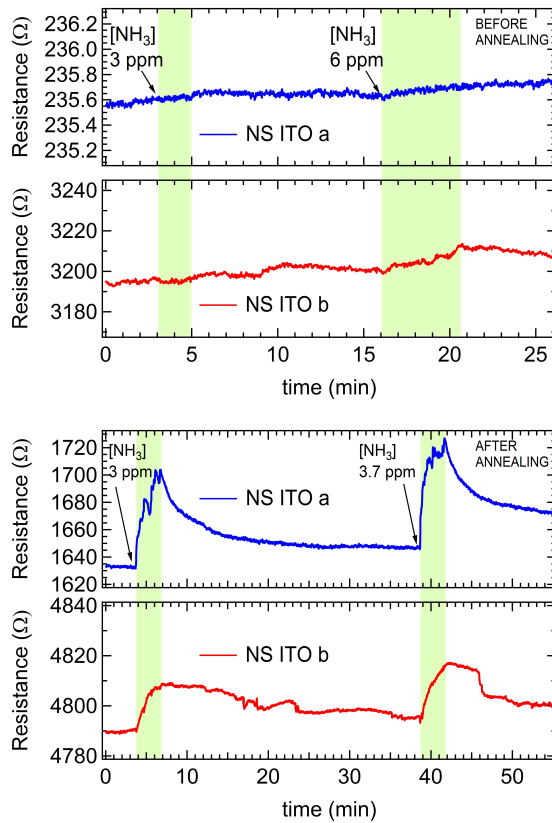


**Figure 5.17:** “NS ITO a” (blue curve on top of each panel) and “NS ITO b” (red curve on bottom of each panel) sensor response before (top panel) and after (bottom panel) the annealing.

annealing the sensors do not respond to ammonia gas because of the amorphous carbon that cover the tin nanopillars, while a good response ( $\Delta R/R_0 \approx 0.04$  with  $[\text{NH}_3] \approx 3$  ppm, leading to a sensitivity  $(\Delta R/R_0)/[\text{NH}_3] \approx 0.01$ ) is recorded for the “NS ITO a” sensor after the annealing. The “NS ITO b” sensor respond to the same concentration of ammonia with  $\Delta R/R_0 \approx 0.004$ , i.e. a sensitivity  $(\Delta R/R_0)/[\text{NH}_3] \approx 0.001$ , after the annealing treatment. Although the annealing and the consequent carbon pyrolysis allow the sensor to be sensitive to ammonia gas, contrary to the situation before the annealing treatment, when no response is detected (Fig. 5.17 top panel), the temporal evolution of the resistance during ammonia exposure (Fig. 5.17 bottom panel) is quite different compared to that of “NS ITO” sample (Fig. 5.15), in particular considering “NS ITO” and “NS ITO a” which present a similar morphology on the sample surface (Fig. 5.12 c-e and Fig. 5.13 a). This could be attributed to the different parameters of the post-growth annealing processes, namely  $1 \times 10^{-6}$  mbar  $\text{O}_2$ , 10 minutes for the “NS ITO” sample and ambient air for 15 minutes for “NS ITO a” and “NS ITO b” samples. We leave this as an open question, but these effects certainly require more investigations.

### 5.2.3 Response curve and Detection Limit

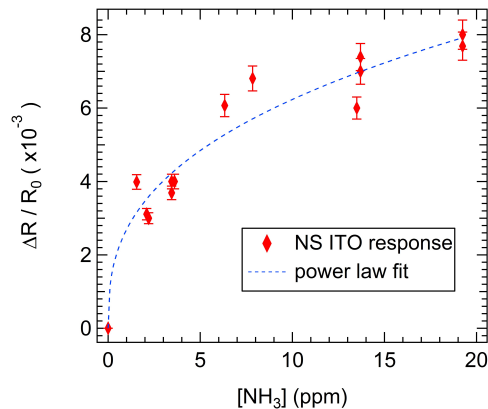


**Figure 5.18:** Response curve of the sensor NS ITO, drawn after a sequence of ammonia exposures as those reported in Fig. 5.15.

After a sequence of ammonia exposures, as those reported in Fig. 5.15, by evaluating the  $\Delta R/R_0$  we are able to plot the response curve for the NS ITO sensor (Fig. 5.18). By fitting the data with a power law  $\Delta R/R_0 = A [\text{NH}_3]^p$ , we obtained the following parameters:  $A = (2.7 \pm 0.3) \times 10^{-3}$ ,  $p = 0.36 \pm 0.04$ . Finally, considering the signal noise  $\sigma = 35.8 \Omega$  and  $5\sigma \approx 180 \Omega$ , a DL of 17 ppb has been estimate by the formula  $5\sigma/R_0 = A (\text{DL})^p$ .

### 5.3 Conclusions

In this chapter possible hybrid architectures to be used in chemical gas sensing have been proposed. In the first section we have shown how CVD on ZnO nanorods allows to synthesize different carbon nanostructures, whose morphology can be tuned with CVD growth parameters. CVD assisted with Fe catalyst results in more ordered CNs and in a better coverage of the ZnO NRs substrate. As a consequence, the sample response as gas sensor, the main objective of this work, is enhanced. Although external environmental conditions affect the sensitivity and the sensor recovery time, these sensors can detect low ppm of ammonia, exhibiting selectivity with respect to other tested gases (acetone, ethanol, nitrogen dioxide). In the second section of this chapter, the original preparation, by D'Arsié *et al.* using catalyst-free  $\text{C}_2\text{H}_2$  CVD on ITO substrates, of ordered and possibly vertically aligned arrays of carbon covered tin nanowires or  $\text{SnO}_x$  nanopillars on ITO substrates, has been described. These hybrid nanomaterials has been tested as ammonia gas sensor in air at room temperature, showing a good sensitivity and a very efficient recovery time.



# Appendices





# Appendix A

## SWCNT-based $\text{NH}_3$ sensor in chemFET configuration

The SWCNTs response to ammonia gas has been tested also in chemFET configuration (see Fig. 1.14 in chapter 1.14). In order to prepare a SWCNT-based chemFET, a p-doped silicon substrate (thickness  $500 \pm 25 \mu\text{m}$ ), covered with  $150 \text{ nm} \pm 10\%$   $\text{SiO}_2$  layer (Siltronix SAS) have been used as gate electrode. The source and drain electrodes consist of Ag paste stripes and SWCNTs (deposited by drop casting) are the sensitive layer. Fig. A.1 (a-c) (taken from a

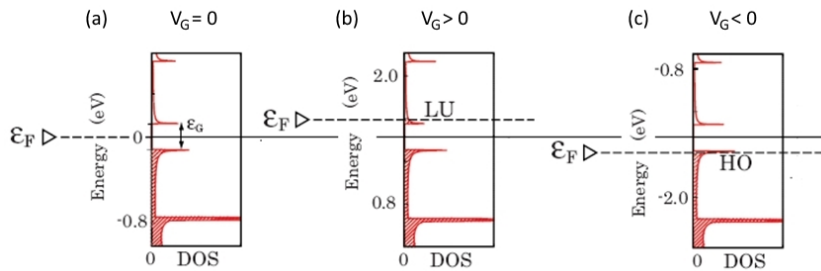


**Figure A.1:** Density of states structure of a semiconducting (7,0) CNT under the gate-bias voltage of (a)  $V_G = 0$ , (b)  $V_G = 1.59 \text{ V}$  and (c)  $V_G = -1.56 \text{ V}$  (Figure adapted from Ref. [137]).

first-principles study carried out by K. Uchida *et al.* [137]), shows the DOS spectrum of a semiconducting (7,0) CNT together with the Fermi level  $\varepsilon_F$  of the CNT under the gate-bias voltage of  $V_G = 0$ ,  $V_G = 1.59$  V and  $V_G = -1.56$  V, respectively. We remember that in the p-type or “hole” conduction, a negative gate voltage reduces the number of electrons in the channel, i.e. increases the number of holes, so that the channel become more conductive [138].

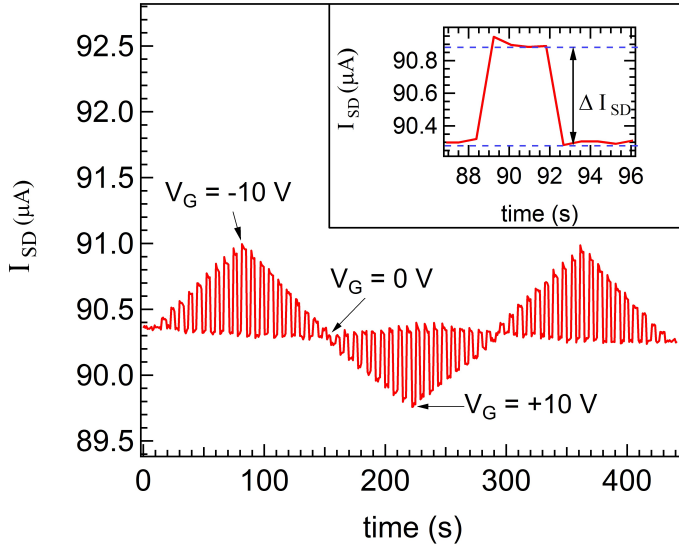


**Figure A.2:** Current flowing through SWCNTs between source and drain electrodes, varying the gate potential  $V_g$  from -10 V to +10 V (step 1 V). For each gate voltage value, the current variation  $\Delta I_{SD}$  has been measured (inset).

In Fig.A.2 a typical measurement of the current  $I_{SD}$  flowing through SWCNTs between source and drain electrodes, varying the gate potential  $V_G$  from -10 V to +10 V with step of 1 V, is shown. When a negative gate voltage is applied, an increase of current has been detected, confirming the p-type character of the SWCNT-based device [138].

Measurements as that shown in Fig. A.2 has been carried out also in presence of ammonia gas ( $[\text{NH}_3] = 5$  ppm). For each gate voltage value  $V_G$ , the current variation  $\Delta I_{SD}$  has been measured and the modulus of  $\Delta I_{SD}$  has been

plotted versus  $V_G$  (Fig. A.3 a). In Fig. A.3 b the difference between the modulus of  $\Delta I_{SD}$  in dry air (without ammonia gas) and in dry air with 5 ppm  $[\text{NH}_3]$  is shown. The ammonia effect is evident for negative  $V_G$ , in accordance with higher hole density on the nanotube surface, which promotes the  $\text{NH}_3$  interaction. The negative  $V_G$  shifts downward the Fermi level, increasing the conduction in the p-type SWCNT, but the presence of  $\text{NH}_3$  which injects extra-electrons on the CNT surface, make the jump  $\Delta I_{SD}$  lower.

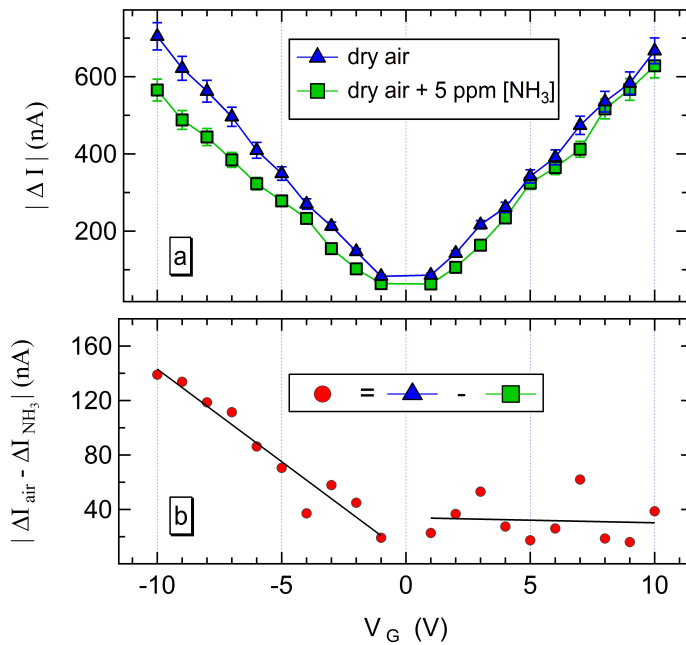


**Figure A.3:** (a) Current variation  $\Delta I_{SD}$  versus gate voltage  $V_G$  in dry air (blue triangles curve) and in 5 ppm  $\text{NH}_3$  (green squares curve) atmosphere. The measurements have been carried out at room temperature ( $T \approx 25^\circ\text{C}$ ) and  $\text{RH} \approx 10\%$ . (b) Difference (red dots) between the two curves plotted in (a) and fit (black lines) for negative and positive  $V_G$ .

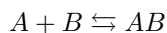


# Appendix B

## Adsorption isotherms

Among all the adsorption isotherms the Langmuir model (1916) is one of the most popular, also nowadays. About 100 years ago Irving Langmuir was developing his theory of adsorption of gas on solid surfaces [139], [140], verified by a large number of experiments (cite Langmuir 1915). He believed that *“when gas molecules impinge against any solid or liquid surface they do not in general rebound elastically, but condense on the surface, being held by the field of forces of the surface atoms. These molecules may subsequently evaporate from the surface. The length of time that elapses between the condensation of a molecule and its subsequent evaporation depends on the intensity of the surface forces. Adsorption is the direct result of this time lag. If the surface forces are relatively intense, evaporation will take place at only a negligible rate”* [140]. Langmuir emphasized the chemical nature of the forces involved in the adsorption process. But he also highlighted that his chemical theory of adsorption was different from previous theories which “believed that *definite* chemical compounds were formed on the surface”. He suggested that “the adsorbed atoms are chemically combined to the surface atoms of the solid *but these in turn are chemically combined to those below them, and so on throughout the whole mass of the solid*”. He also proved that the true adsorbed films do not exceed one molecule in thickness.

The idea is to consider a chemical reaction between A and B:



where the reagent A is the gas molecule  $M_{(g)}$  that strikes the solid surface and the reagent B is the vacant surface site  $S^*$  available for the adsorption. Then the product will be the the molecule adsorbed on the surface  $S-M$  and we can write the “adsorption reaction”:



We can derive Langmuir isotherm, in the case of simple adsorption, from equilibrium consideration [140] From Langmuir isotherm

$$\theta = \frac{bC}{1 + bC} \quad (\text{B.2})$$

where  $\theta$  is the surface coverage,  $b$  is the adsorption coefficient and  $C$  is the sorbate concentration, and assuming the distribution function of adsorption sites to be in exponential form [141, 142]

$$b = b_0 \exp(Q/RT) \quad (\text{B.3})$$

whit  $b_0$  a constant,  $Q$  the adsorption energy,  $R$  the universal gas constant and  $T$  the temperature, it is possible to derive the Freundlich isotherm in the modified form (posso mettere i passaggi in appendice?):

$$\theta_F = \frac{(b_0 C)^m}{\sin(m\pi)/(m\pi)} \quad (\text{B.4})$$

where  $\theta_F$  is the coverage,  $m$  and  $b_0$  are constant and  $C$  is the concentration. Eq. B.4 is valid for small values of concentration  $C$ . Furthermore, for small values of  $m$ ,  $\sin(m\pi)/(m\pi) \approx 1$  and the original Freundlich’s expression is obtained:

$$\theta_F = KC^m \quad (\text{B.5})$$

where  $K = b_0^m$ . Sometimes we find  $\theta_F$  in function of pressure  $p$ , instead of concentration  $C$ , but assuming a direct proportionality between  $p$  and  $C$  (something like Henry’s law), there is no substantial differences. Eq. B.5 is often use in surface science and in environmental science to obtain the surface coverage vs. the gas concentration (or the amount of gas vs. the gas pressure).

---

## Why choosing Freundlich equation and relation with gas response curve

Now we want to compare Freundlich isotherm, that relates surface coverage  $\theta_F$  and the gas concentration (or pressure), with our power fit of the response curve, where  $\Delta R/R_0$  is plotted vs. ammonia concentration

$$\frac{\Delta R}{R_0} = A[NH_3]^p \quad (\text{B.6})$$

The hypothesis of small concentration (or small pressure) is respected because we are considering few ppm of ammonia gas, and also the power exponent is small ( $p = 0.56$ ). Assuming, as Peng *et al.* did [143], that the change of conductance  $\Delta G$  (or the change of resistance  $\Delta R$ ) is proportional to the gas coverage  $\theta$ , we can directly compare the terms in Eq. B.6 with the terms in Eq. B.5. In particular we can consider  $\frac{\Delta R}{R_0}(C)$  as  $\theta(C)$ , the fraction of surface covered by  $NH_3$  molecules (or the  $NH_3$  molecules adsorbed by SWCNT layer). This is in accordance with many works in literature that use power laws for semiconductor gas sensors [96, 144].





# Appendix C

## Conversion of R.H. into ppm of water

The relative humidity (R.H.) of an air-water mixture is defined as the ratio of the partial pressure  $e$  of water vapor in the mixture to the saturated vapor pressure of water  $e^*$  at a given temperature. R.H. is normally expressed as a percentage and is calculated by using the following equation C.1 [145]:

$$R.H. = \left(\frac{e}{e^*} \times 100\%\right) \quad (C.1)$$

The conversion from R.H. to ppm of water is based on the following equations. First, the dew point temperature  $T_d$  is evaluated according to the formula:

$$T_d = \left(\frac{R.H.}{100}\right)^{1/8}(112 + 0.9T) + 0.1T - 112 \quad (C.2)$$

Then one has to consider the dependence of vapor pressure  $e$  on both pressure  $P$  (mbar) and temperature  $T$  ( $^{\circ}\text{C}$ )

$$e(P, T) = (1.0007 + 3.46 \cdot 10^{-6}P) \cdot 6.1121 \cdot \exp\left(\frac{17.502T}{240.9 + T}\right) \quad (C.3)$$

The coefficients appearing in eq.C.2 and eq.C.3 are subjected to continuous refinement, as addressed in Refs. [146, 147]. These equations allow one to calculate

$e(T_d)$  and therefore obtain either the moisture concentration  $\text{ppm}_v$  (parts per million by volume) as:

$$\text{ppm}_v = \frac{10^6 \cdot e(T_d)}{P - e(T_d)} \quad (\text{C.4})$$

or the moisture concentration  $\text{ppm}_w$  (parts per million by weight) as:

$$\text{ppm}_w = 0.622 \cdot \text{ppm}_v \quad (\text{C.5})$$

# Bibliography

- [1] A.H. W. Beusen, A.F. Bouwman, P.S.C. Heuberger, G. Van Drecht, and K.W. Van Der Hoek. *Atmos. Environ.*, 42:6067, 2008.
- [2] V.P. Aneja, W.H. Schlesinger, and J.W. Erisman. *Nat. Geosci.*, 1:409, 2008.
- [3] M.A. Sutton, J.W. Erisman, F. Dentener, and D. Moeller. *Environ. Pollut.*, 156:583, 2008.
- [4] J.W. Erisman, A. Bleeker, J. Galloway, and M.A. Sutton. *Environ. Pollut.*, 150:140, 2007.
- [5] B.H. Baek, V.P. Aneja, and Q. Tong. *Environ. Pollut.*, 129:89, 2004.
- [6] G.M. Marcazzan, S. Vaccaro, G. Valli, and R. Vecchi. *Atmos. Environ.*, 35:4639, 2001.
- [7] G.M. Marcazzan, M. Ceriani, G. Valli, and R. Vecchi. *Sci. Total Environ.*, 317:137, 2003.
- [8] A. Charron, R.M. Harrison, and P. Quincey. *Atmos. Environ.*, 41:1960, 2007.
- [9] M. Chiesa, F. Rigoni, M. Paderno, P. Borghetti, G. Gagliotti, M. Bertoni, A. Ballarin Denti, L. Schiavina, A. Goldoni, and L. Sangaletti. *J. Environ. Monit.*, 14:1565, 2012.
- [10] S. Iijima. *Nature*, 354:56–58, 1991.

- 
- [11] T. Someya, J. Small, P. Kim, C. Nuckolls, and J.T. Yardley. *Nano Lett.*, 3:877, 2003.
- [12] T. Zhang, S. Mubeen, N.V. Myung, and M.A. Deshusses. *Nanotechnology*, 19:332001, 2008.
- [13] A. Goldoni, L. Petaccia, S. Lizzit, and R. Larciprete. *J. Phys.: Condens. Matter*, 22:013001, 2010.
- [14] G. Jimenez-Cadena, J. Riu, and F.-X. Rius. *Analyst*, 132:1083, 2007.
- [15] A. Goldoni, L. Petaccia, L. Gregoratti, B. Kaulich, A. Barinov, S. Lizzit, A. Laurita, L. Sangaletti, and R. Larciprete. *Carbon*, 42:2099, 2004.
- [16] S. Chopra, K. McGuire, N. Gothard, A.M. Rao, and A. Pham. *Appl. Phys. Lett.*, 83:2280, 2003.
- [17] J. Li, Y.J. Lu, Q. Ye, M. Cinke, J. Han, and M. Meyyappan. *Nano Lett.*, 3:929, 2003.
- [18] J.P. Novak, E.S. Snow, E.J. Houser, D. Park, J.L. Stepnowski, and R.A. McGill. *Appl. Phys. Lett.*, 83:4026, 2003.
- [19] F. Picaud, C. Girardet, and A.M. Rao. *J. Appl. Phys.*, 105:014315, 2009.
- [20] P. Vichchulada, P.Q. Zhang, and M.D. Lay. *Analyst*, 132:719, 2007.
- [21] D.R. Kauffman and A. Star. *Angew. Chem.*, 47:6550, 2008.
- [22] M. Penza, R. Rossi, M. Alvisi, M.A. Signore, and E. Serra. *J. Phys. D: Appl. Phys.*, 42:072002, 2009.
- [23] M. Penza, R. Rossi, M. Alvisi, and E. Serra. *Nanotechnology*, 21:105501, 2010.
- [24] G. Chen, T.M. Paronyan, E.M. Pigas, and A.R. Harutyunyan. *Sci. Rep.*, 2:343, 2012.
- [25] M. Monthieux and V.L. Kuznetsov. *Carbon*, 44:1621, 2006.
- [26] A. Oberlin, M. Endo, and T. Koyama. *J. Cryst. Growth*, 32:335, 1976.

- [27] S. Reich, C. Thomsen, and J. Maultzsch. *Carbon Nanotubes: Basic Concepts and Physical Properties*. Wiley, London, 2004.
- [28] P.J.F. Harris. *Carbon nanotube science: synthesis, properties and applications*. Cambridge University Press, New York, 2009.
- [29] N. Hamada, S.I. Sawada, and A. Oshiyama. *Phys. Rev. Lett.*, 68:1579, 1992.
- [30] R. Saito, M. Fujita, G. Dresselhaus, and M.S. Dresselhaus. *Phys. Rev. B*, 46:1804, 1992.
- [31] G. Bertoni and L. Calmels. *Micron*, 37:486, 2006.
- [32] M.S. Dresselhaus, G. Dresselhaus, and P. Avouris. *Carbon Nanotubes: Synthesis, Structure, Properties and Application*. Springer, Berlin, 2000.
- [33] Y. Miyata, Y. Maniwa, and H. Kataura. *J. Phys. Chem. B*, 110:25, 2006.
- [34] T.W. Odom, J.-L. Huang, P. Kim, and C.M. Lieber. *J. Phys. Chem. B*, 104:2794, 2000.
- [35] P. Kim, T.W. Odom, J.-L. Huang, and C.M. Lieber. *Phys. Rev. Lett.*, 82:1225–1228, 1999.
- [36] M. Ouyang, J.-L. Huang, C.L. Cheung, and C.M. Lieber. *Science*, 292:702, 2001.
- [37] A. Kasuya, M. Sugano, T. Maeda, Y. Saito, K. Tohji, H. Takahashi, Y. Sasaki, M. Fukushima, Y. Nishina, and C. Horie. *Phys. Rev. B*, 57:4999, 1998.
- [38] M.A. Pimenta, A. Marucci, S.A. Empedocles, M.G. Bawendi, E.B. Hanlon, A.M. Rao, P.C. Eklund, R.E. Smalley, G. Dresselhaus, and M.S. Dresselhaus. *Phys. Rev. B*, 58, 1998.
- [39] A. Jorio, A.G. Souza Filho, G. Dresselhaus, M.S. Dresselhaus A.K. Swan, M.S. Ünlü, B.B. Goldberg, M.A. Pimenta, J.H. Hafner, C.M. Lieber, and R. Saito. *Phys. Rev. B*, 65:155412, 2002.

- [40] C. Fantini, A. Jorio, M. Souza, M.S. Strano, and M.S. Dresselhaus and M.A. Pimenta. *Phys. Rev. Lett.*, 93:147406, 2004.
- [41] R. Martel, T. Schmidt, H.R. Shea, T. Hertel, and P. Avouris. *Appl. Phys. Lett.*, 73:2447, 1998.
- [42] T. Dürkop, S.A. Getty, E. Cobas, and M.S. Fuhrer. *Nano Lett.*, 4:35, 2004.
- [43] J. Kong, N.R. Franklin, C. Zhou, M.G. Chapline, S. Peng, k. Cho, and H. Dai. *Science*, 287:622, 2000.
- [44] P.G. Collins, K. Bradley, M. Ishigami, and A. Zettl. *Science*, 287:1801, 2000.
- [45] G.U. Sumanasekera, C.K.W. Adu, S. Fang, and P.C. Eklund. *Phys. Rev. Lett.*, 85:1096, 2000.
- [46] X.P. Tang, A. Kleinhammes, H. Shimoda, L. Fleming, K.Y. Bennoune, S. Sinha, C. Bower, O. Zhou, and Y. Wu. *Science*, 288:492, 2000.
- [47] A. Goldoni, R. Larciprete, L. Petaccia, and S. Lizzit. *J. Am. Chem. Soc.*, 125:11329, 2003.
- [48] J. Zhao, A. Buldum, J. Han, and J.P. Lu. Gas molecule adsorption in carbon nanotubes and nanotube bundles. 13:195, 2002.
- [49] H. Chang, J.D. Lee, S.M. Lee, and Y.H. Lee. *Appl. Phys. Lett.*, 79:3863, 2001.
- [50] B.B. Shirvani, J. Beheshtian, G. Parsafar, and N.L. Hadipour. *Computational Materials Science*, 48:655, 2010.
- [51] A. Javey and J. Kong. *Carbon nanotube Electronics*. Springer, USA, 2009.
- [52] H.-S.P. Wong and D. Akinwande. *Carbon nanotube and graphene device physics*. Cambridge University Press, New York, 2011.
- [53] A. Goldoni, L. Petaccia, S. Lizzit, and R. Larciprete. *J. Phys.: Condens. Matter*, 22:8, 2009.

- [54] L. Valentini, C. Cantalini, I. Armentano, J.M. Kenny, L. Lozzi, and S. Santucci. 21:1996, 2003.
- [55] C.Y. Lee S. Baik, J.Q. Zhang, R.I. Masel, and M.S. Strano. *J. Phys. Chem. B*, 110:11055, 2006.
- [56] J. Suehiro and G.B. Zhou M. Hara. *J. Phys. D: Appl. Phys.*, 36:109, 2003.
- [57] E.S. Snow, F.K. Perkins, E.J. Houser, S.C. Badescu, and T.L. Reinecke. *Science*, 307:1942, 2005.
- [58] S. Chopra, A. Pham, J. Gaillard, A. Parker, and A.M. Rao. *Appl. Phys. Lett.*, 80:4632, 2002.
- [59] A. Modi, N. Koratkar, E. Lass, B.Q. Wei, and P.M. Ajayan. *Nature*, 424:171, 2003.
- [60] Christopher Brett. Other types of sensors: Impedance-based sensors, fet sensors, acoustic sensors. In L.M. Moretto and K. Kalcher, editors, *Environmental Analysis by Electrochemical Sensors and Biosensors*, Nanos-structure Science and Technology, pages 351–370. Springer New York, 2014.
- [61] Q. Cao, H. Kim, N. Pimparkar, J.P. Kulkarni, C. Wang, M. Shim, M.A. Alam K. Roy, and J.A. Rogers. *Nature*, 454–500:495, 2008.
- [62] D. Sun, M.Y. Timmermans, Y. Tian, A.G. Nasibulin, E.I. Kauppinen, S. Kishimoto, T. Mizutani, and Y. Ohno. *Nature Nanotechnology*, 6:156, 2011.
- [63] F. Rigoni, G. Drera, S. Tognolini, P. Borghetti, S. Pagliara, A. Goldoni, and L. Sangaletti. *Elettra Highlights*, 1:78–79, 2014.
- [64] Figaro an ISO9001/14001 company. *GENERAL INFORMATION FOR TGS SENSORS*, 3 2005.
- [65] Enfis Ltd. *ENFIS UNO Air Cooled Light Engine*, 7 2008.
- [66] F. Rigoni, S. Tognolini, P. Borghetti, G. Drera, S. Pagliara, A. Goldoni, and L. Sangaletti. *Analyst*, 138:7392, 2013.

- 
- [67] M.S. Dresselhaus, G. Dresselhaus, R. Saito, and A. Jorio. *Phys. Rep.*, 409:47, 2005.
- [68] M. Milnera, J. Kurti, M. Hulman, and H. Kuzmany. *Phys. Rev. Lett.*, 84:1324, 2000.
- [69] R. Krupke, F. Hennrich, H.V. Lohneysen, and M.M. Kappes. *Science*, 301:344, 2003.
- [70] M. Lucci, P. Regoliosi, A. Reale, A. Di Carlo, S. Orlanducci, E. Tamburri, M.L. Terranova, P. Lugli, C. Di Natale, A. D'Amico, and R. Paolesse. *Sens. Actuators, B*, 111:181, 2005.
- [71] M.L. Terranova, M. Lucci, S. Orlanducci, E. Tamburri, V. Sessa, A. Reale, and A. Di Carlo. *J. Phys.: Condens. Matter*, 19:22504, 2007.
- [72] T. Zhang, M.B. Nix, B.Y. Yoo, M.A. Deshusses, and N.V. Myung. *Electroanalysis*, 18:1153, 2006.
- [73] M. Penza, R. Rossi, M. Alvisi, G. Cassano, M.A. Signore, E. Serra, and R. Giorgi. *Sens. Actuators, B*, 135:289, 2008.
- [74] H. Guerin, H. Le Poche, R. Pohle, L.S. Bernard, E. Buitrago, R. Ramos, J. Dijon, and A.M. Ionescu. *Carbon*, 78:326, 2014.
- [75] F. Rigoni, S. Tognolini, P. Borghetti, G. Drera, S. Pagliara, A. Goldoni, and L. Sangaletti. *Procedia Engineering*, 87:716, 2014.
- [76] J. Samitier, J.M. López-Villegas, S. Marco, L. Cámara, A. Pardo, and O. Ruiz J.R. Morante. *Sens. Actuators, B*, 18:308, 1994.
- [77] S. Marco, J. Palacín, and J. Samitier. *IEEE Transactions on Instrumentation and Measurement*, 50:774, 2001.
- [78] C.Y. Lee and M.S. Strano. *Langmuir*, 21:5192, 2005.
- [79] B.-Y. Wei, M.-C. Hsu P.-G. Su, H.-M. Lin, R.-J. Wu, and H.-J. Lai. *Sens. Actuators, B*, 101:81, 2004.
- [80] N.D. Hoa, N.V. Quy, and D. Kim. *Sens. Actuators, B*, 142:253, 2009.



- [81] A. Sharma, M. Tomar, and V. Gupta. *J. Mater. Chem.*, 22:23608, 2012.
- [82] S. Mubeen, M. Lai, T. Zhang, J.-H. Lim, A. Mulchandani, M.A. Deshusses, and N.V. Myung. *Electrochimica Acta*, 92:484, 2013.
- [83] J. Yoon, K.W. Min, J. Kim, G.T. Kim, and J.S. Ha. *Nanotechnology*, 23:265301, 2012.
- [84] H.C. Su, M. Zhang, W. Bosze, and N.V. Myung. *J. of The Electrochemical Society*, 161:283, 2014.
- [85] S. Suzuki. *Syntheses and Applications of Carbon Nanotubes and Their Composites*. InTech, 2013.
- [86] F. Rigoni, G. Drera, S. Pagliara, A. Goldoni, and L. Sangaletti. *Carbon*, 80:356, 2014.
- [87] G. Drera, G. Salvinelli, J. hlund, P.G. Karlsson, B. Wannberg, E. Magnano, S. Nappini, and L. Sangaletti. *J. Electr. Spectr. and Rel. Phen.*, 195:109, 2014.
- [88] N. Barsan, J. Rebholz, and U. Weimar. *Sens. Actuators, B*, 207:455, 2015.
- [89] N. Barsan, M. Hubner, and U. Weimar. *Sens. Actuators, B*, 157:510, 2011.
- [90] M. Hubner, C.E. Simion, A. Tomescu-Stanoiu, S. Pokhrel, N. Barsan, and U. Weimar. *Sens. Actuators, B*, 153:347, 2011.
- [91] Hans Lüth. *Solid Surfaces, Interfaces and Thin Films (Fifth Edition)*. Springer, 2010.
- [92] G. Heiland. *Z. Phys.*, 138:459, 1954.
- [93] T. Seiyama, A. Kato, K. Fujiishi, and M. Nagatani. *Anal. Chem.*, 34:5, 1962.
- [94] S.A. Hodge, M.K. Bayazit, K.S. Colemanb, and M.S.P. Shaffer. *Chem. Soc. Rev.*, 41:4409, 2012.
- [95] R. Sarhaddi, N. Shahtahmasebi, M.R. Rokn-Abadi, and M.M. Bagheri-Mohagheghi. *Physica E*, 43:452, 2010.

- [96] N. Barsan and U. Weimar. *Journal of Electroceramics*, 7:143, 2001.
- [97] R.W.J. Scott, S.M. Yang, G. Chabanis, N. Coombs, D.E. Williams, and G.A. Ozin. *Adv. Mater.*, 13:1468, 2001.
- [98] C.L. Cao, C.G. Hu, L. Fang, S.X. Wang, Y.S. Tian, and C.Y. Pan. *Nanomater.*, 2011:707303, 2010.
- [99] E. Steven, W.R. Saleh, V. Lebedev, S.F.A. Acquah, V. Laukhin, R.G. Alamo, and J.S. Brooks. *Nature Communication*, 4:2435, 2013.
- [100] L. Liu, X. Ye, K. Wu, Z. Zhou, and D. Lee T. Cui. *IEEE Sensors Journal*, 9:1308, 2009.
- [101] G.F. Fine, L.M. Cavanagh, A. Afonja, and R. Binions. *Sensors*, 10:5469, 2010.
- [102] J.W. Han, B. Kim, N.P. Kobayashi, J. Li, and M. Mayyappan. *Appl. Phys. Lett.*, 101:142110, 2012.
- [103] C.-W. Lin, H.-I. Chen, T.-Y. Chen, C.-C. Huang, C.-S. Hsu, and W.-C. Liu. *IEEE Trans. Electron Devices*, 58:4407, 2011.
- [104] A. Zahab, L. Spina, P. Poncharal, and C. Marliere. *Phys. Rev. B*, 62:1000, 2000.
- [105] K. Bradley, J.C.P. Gabriel, M. Briman, A. Star, and G. Gruner. *Phys. Rev. Lett.*, 91:218301, 2003.
- [106] N. Barsan, C. Simion, T. Heine, S. Pokhrel, and U. Weimar. *Journal of Electroceramics*, 25:11, 2010.
- [107] J. Liu, X. Huang, G. Ye, W. Liu, Z. Jiao, W. Chao, Z. Zhou, and Z. Yu. *Sensors*, 3:110, 2003.
- [108] X. Xue, L. Xing, Y. Chen, S. Shi, Y. Wang, and T. Wang. *J. Phys. Chem. C*, 112:12157, 2008.
- [109] H.-S. Woo, C.W. Na, I.D. Kim, and J.-H. Lee. *Nanotechnology*, 23:245501, 2012.

- [110] J. Deng, L. Wang, Z. Lou, and T. Zhang. *J. Mater. Chem. A*, 2:9030, 2014.
- [111] G.-J. Sun, S.-W. Choi, S.-H. Jung, A. Katoch, and S.S. Kim. *Nanotechnology*, 24:025504, 2013.
- [112] J.-H. Yun, J. Kim, Y.C. Park, J.-W. Song, D.-H. Shin, and C.-S. Han. *Nanotechnology*, 20:055503, 2009.
- [113] D. Eder. *Chem. Rev.*, 110:1348, 2010.
- [114] C. Sanchez and P. Gomez-Romero. *Functional hybrid materials*. Wiley-VCH Verlag GmbH and Co. KGaA, Weinheim, Germany, 2004.
- [115] G. Kickelbick. *Hybrid materials: synthesis, characterization and application*. Wiley-VCH Verlag GmbH and Co. KGaA, Weinheim, Germany, 2007.
- [116] S.H. Jo, D. Banerjee, and Z.F. Ren. *Appl. Phys. Lett.*, 85:1407, 2004.
- [117] S.Y. Bae, H.W. Seo, H.C. Choi, and J. Park. *J. Phys. Chem. B*, 108:12318, 2004.
- [118] C. Li, G. Fang, L. Yuan, N. Liu, L. Ai, and Q. Xiang. *Nanotechnology*, 18:155702, 2007.
- [119] R.-C. Wang, C.-C. Hsu, and S.-J. Chen. *Nanotechnology*, 22:035704, 2011.
- [120] P. Mbuyisa, S. P. Bhardwaj, F. Rigoni, E. Carlino, S. Pagliara, L. Sangaletti, A. Goldoni, M. Ndwandwe, and C. Cepek. *Carbon*, 50:5472, 2012.
- [121] P. Strubel, S. Thieme, T. Biemelt, A. Helmer, M. Oschatz, J. Brckner, H. Althues, and S. Kaskel. *Adv. Funct. Mater.*, 25:287–297, 2015.
- [122] W. Gong, W. Chen, J. He, Y. Tong, C. Liu, L. Su, B. Gao, H. Yang, Y. Zhang, and X. Zhang. *Carbon*, 83:275, 2015.
- [123] L.Z. Wang. *Mater. Sci. Eng.*, 64:33, 2009.
- [124] G.J. Minkoff. *Can. J. Chem.*, 36:131, 1985.
- [125] J.M. Vohs and M.A. Barteau. *J. Phys. Chem.*, 91:4766, 1987.

- [126] C. Klingshirn. *Phys. Stat. Sol. (b)*, 244:3027, 2007.
- [127] P. Mbuyisa. *Growth and characterization of carbon nanostructures on zinc oxide nanostructures*. PhD thesis, University of Zululand, Faculty of Science and Agriculture, Department of Physics and Engineering, 2012.
- [128] L. Sangaletti, M.C. Mozzati, G. Drera, P. Galinetto, C.B. Azzoni, A. Speghini, and M. Bettinelli. *Phys. Rev. B*, 78:075210, 2008.
- [129] M.Z. Yang, C.L. Dai, and C.C. Wu. 11:11112, 2011.
- [130] Y. Zeng, T. Zhang, M. Yuan, M. Kang, G. Lu, and R. Wang. *Sens. Actuators, B*, 143:93, 2009.
- [131] D. Kazachkin, Y. Nishimura, S. Irle, E. Borguet, R. Vidic, and K. Morokuma. *Langmuir*, 24:7848, 2008.
- [132] N.S. Sariciftci, L. Smilowitz, A.J. Heeger, and F. Wudl. *Science*, 258:1474, 1992.
- [133] M. Sawada, M. Higuchi, S. Kondo, and H. Saka. *Jpn. J. Appl. Phys.*, 40:3332, 2001.
- [134] H. Kim, J.S. Horwitz, W.K. Kim, Z.H. Kafafi, and D.B. Chrisey. *J. Appl. Phys.*, 91:5371, 2002.
- [135] R.A. Synowicki, J.S. Hale, N.J. Ianno, J.A. Woollam, and P.D. Ham-bourger. *Surf. Coat. Technol.*, 62:499, 1993.
- [136] L. D'Arsié, M. Fanetti, C. Cepek, L. Casalis, P. Parisse, L. Gregoratti, M. Amati, G. Di Santo, E. Capria, A. Fraleoni-Morgera, E. Nicolini, and A. Goldoni. *Carbon*, 65:13, 2013.
- [137] K. Uchida and S. Okada. *Phys. Rev. B*, 79:085402, 2009.
- [138] S. Datta. *Quantum Transport: Atom to Transistor*. Cambridge University Press, New York, 2005.
- [139] I. Langmuir. *Phys. Rev.*, 8:149, 1916.
- [140] I. Langmuir. *J. Am. Chem. Soc.*, 40:1361, 1918.

- 
- [141] C. Sheindorf, M. Rebhun, and M. Sheintuch. *Journal of Colloid and Interface Science*, 79:136, 1981.
- [142] M.S. Da Rocha, K. Iha, A.C. Faleiros, E.J. Corat, and M.E.V. Suárez-Iha. *Journal of Colloid and Interface Science*, 185:493, 1997.
- [143] S. Peng, K. Cho, P. Qi, and H. Dai. *Chem. Phys. Lett.*, 387:271, 2004.
- [144] N. Yamazoe and K. Shimano. *Sens. Actuators, B*, 128:566, 2008.
- [145] M. Wanielista, R. Kersten, and R. Eaglin. *Hydrology water quantity and quality control. 2nd ed.* Wiley, New York, 1997.
- [146] A. Wexler and L. Greenspan. *Journal of Research of the National Bureau of Standards A*, 80A:775, 1976.
- [147] B. Hardy. *Papers and Abstracts, 3rd International Symposium on Humidity and Moisture, NPL London*, page 214, 1998.



# List of publications & presentations

## Publications

### Publications related to the thesis

- M. Chiesa, **F. Rigoni**, M. Paderno, P. Borghetti, G. Gagliotti, M. Bertoni, A. Ballarin Denti, L. Schiavina, A. Goldoni, L. Sangaletti: “*Development of a low-cost ammonia gas sensors and data analysis algorithms to implement a monitoring grid of urban environmental pollutants*”, Journal of Environmental Monitoring, **14**, 1565-1575 (2012)
- P. Mbuyisa, S. P. Bhardwaj, **F. Rigoni**, E. Carlino, S. Pagliara, L. Sangaletti, A. Goldoni, M. Ndwandwe, C. Cepek: “*Controlled synthesis of carbon nanostructures using aligned ZnO nanorods as templates*”, Carbon, **50**, 5472-5480 (2012)
- **F. Rigoni**, S. Tognolini, P. Borghetti, G. Drera, S. Pagliara, A. Goldoni, L. Sangaletti: “*Enhancing the sensitivity of chemiresistor gas sensors based on pristine carbon nanotubes to detect low-ppb ammonia concentrations in the environment*”, Analyst, **138**, 7392-7399 (2013)
- **F. Rigoni**, G. Drera, S. Pagliara, A. Goldoni, L. Sangaletti: “*High sensitivity, moisture selective, ammonia gas sensors based on single-walled carbon nanotubes functionalized with indium tin oxide nanoparticles*”, Carbon, **80**, 356-363 (2014)

- **F. Rigoni**, S. Tognolini, P. Borghetti, G. Drera, S. Pagliara, A. Goldoni, L. Sangaletti: “*Environmental monitoring of low-ppb ammonia concentrations based on single-wall carbon nanotube chemiresistor gas sensors: detection limits, response dynamics, and moisture effects*”, *Procedia Engineering*, **87**, 716-719 (2014)
- **F. Rigoni**, G. Drera, S. Tognolini, P. Borghetti, S. Pagliara, A. Goldoni, L. Sangaletti: “*Gas sensitive single-walled carbon nanotubes layers for environmental monitoring of ammonia in the ppb range: from surface physics to devices*”, *Elettra Highlights 2014*, 78-79 (2014)

### Other publications during the PhD period

- P. Pallavicini, G. Dacarro, P. Grisoli, C. Mangano, M. Patrini, **F. Rigoni**, L. Sangaletti, A. Taglietti: “*Coordination chemistry for antibacterial materials: a monolayer of a Cu 2+ 2,2'-bipyridine complex grafted on a glass surface*”, *Dalton Transactions*, **42**, 4552-4560 (2013)

### Publication submitted and in preparation

- **F. Rigoni**, G. Drera, S. Pagliara, E. Pergem, C. Pintossi, A. Goldoni, L. Sangaletti: “*Enhanced response to NH<sub>3</sub> and NO<sub>2</sub> of single-walled carbon nanotubes sensing layers functionalized with oxide nanoparticles: sub-ppm sensitivity and effects of UV curing*”, *Sensors and Actuators B: Chemical*, submitted paper
- P. N. Mbuyisa, **F. Rigoni**, L. Sangaletti, S. Bhardwaj, M. Ndwandwe and C. Cepek *et al.*: “*Growth of carbon nanostructures on iron decorated ZnO nanorods*”, manuscript in preparation
- **F. Rigoni**, A. Goldoni, L. Sangaletti *et al.*: “*Fast recovery ammonia gas sensors based on vertically oriented tin nanopillars on ITO*”, manuscript in preparation



## Presentations at conferences

### Oral presentations

- **F. Rigoni**, S. Tognolini, P. Borghetti, G. Drera, S. Pagliara, A. Goldoni, L. Sangaletti  
*“Environmental monitoring of low-ppb ammonia concentrations based on single-wall carbon nanotube chemiresistor gas sensors: detection limits, response dynamics, and moisture effects”*  
EUROSENSORS 2014, September 8-10, 2014, Brescia, Italy
- **F. Rigoni**, S. Tognolini, P. Borghetti, G. Drera, S. Pagliara, L. Sangaletti, A. Goldoni  
*“Environmental monitoring of low-ppb ammonia concentrations based on single-wall carbon nanotube chemiresistor gas sensors: detection limits, dynamics of the response, and control over interfering-gas effects.”*  
100° Congresso Nazionale - Società Italiana di Fisica, September 22-26, 2014, Pisa, Italy
- **F. Rigoni**  
*“Towards the ppt detection limit of ammonia gas concentrations in the environment by pristine carbon nanotubes chemiresistor gas sensors”*  
International Workshop “From carbon nanotube to graphene: the key material of the future?” Brescia, September 30 - October 1, 2013

### Poster presentations

- **F. Rigoni**, S. Tognolini, P. Borghetti, M. Bertoni, G. Drera, A. Goldoni, L. Sangaletti  
*“Single-wall carbon nanotube chemiresistor gas sensors to detect ammonia concentrations in the environment: towards ppt detection limit of [NH<sub>3</sub>] and water selectivity”*  
eMRS Spring Meeting 2014, May 26-30, 2014, Lille, France
- **F. Rigoni**, P. Mbuyisa, M. Ndwandwe, S. Pagliara, L. Sangaletti, A. Goldoni, S. Bhardwaj, C. Cepek

*“Exploring novel functionalities in Zinc Oxide-Carbon nanostructured architectures”*

FisMat 2013, September 9-13, 2013, Milano, Italy

- **F. Rigoni**, P. Mbuyisa, M. Ndwandwe, S. Pagliara, L. Sangaletti, A. Goldoni, S. Bhardwaj, C. Cepek

*“Detection of ammonia gas by hierarchical ZnO - CNT hybrid architectures”*

International Conference on Diamond and Carbon Materials, September 2-5, 2013, Riva del Garda, Italy

- **F. Rigoni**, S. Tognolini, P. Borghetti, M. Bertoni, G. Drera, L. Sangaletti, A. Goldoni

*“Enhancing the sensitivity of carbon nanotube arrays for the detection of sub-ppm concentrations of ammonia in urban environments”*

NANOSEA 2012, June 25-29, 2012, S. Margherita di Pula (CA), Italy

- P. Mbuyisa, M. Ndwandwe, **F. Rigoni**, S. Pagliara, L. Sangaletti, A. Goldoni, S.P. Bhardwaj, C. Cepek

*“Synthesis and applications of hierarchical ZnO - CNT hybrid architectures”*

NANOSEA 2012, June 25-29, 2012, S. Margherita di Pula (CA), Italy

- P. Borghetti, **F. Rigoni**, M. Chiesa, M. Paderno, A. Goldoni, L. Sangaletti

*“Carbon nanotubes for ammonia detection: from surface properties to devices”*

NanotechItaly 2010, October 20-22, 2010, Venice, Italy

# Acknowledgements

I would like to acknowledge, first of all, my supervisor Luigi Sangaletti, who gave me the possibility to do research, to meet many clever people in labs and at conferences. He taught me a lot and he gave me the chance to search for my way and do what I like most.

I would like to acknowledge Cinzia Cepek, Andrea Goldoni and Puleng Mbuyisa for the SEM measurements and the very helpful discussions we had in Trieste. Thanks to Giovanni Drera for helping me in the DFT calculations with the *abinit* code. I would like to thank J.-M. Suisse, M. Bouvet and the COST ACTION for the collaboration at ICMUB (Dijon), which increased my experience and knowledge in gas sensors research.

Ora, vorrei ringraziare Maurizio Bertoni, per l'aiuto in laboratorio e per avermi insegnato molto, e i miei tesisti (Silvia, Giorgio, Matteo, Daniele ed Enrico) per aver condiviso gioie e dolori del lavoro in lab. Ringrazio Giovanni, Emanuele e la Patti perchè da voi ho imparato tanto! Grazie a tutti i miei compagni di università e dottorato: Luca, Raimondo, Giulio, Giovanni A., Alessandra, Isa, Davide, Paolo, Gabri, Alessio, Simone, Nicola, ... Grazie a Stefania, Ernesto, Marco e Gianluca per avermi fatto capire il valore della didattica della fisica. In ultimo, ma non per importanza, ringrazio Chiara, Silvia e Stefano (le spice+1) perchè è stato bello lavorare con voi, discutere di fisica ma anche (e soprattutto) condividere momenti di divertimento (non sto ad elencarli tutti, son davvero tanti, mi limito a dire "ognuno fissa un cazzo di niente ed è subito sera" (cit. Stefano Ponzoni), sporty 30 e viva le deadlines, orsetti di tequila e viva le poster sessions)! Mi ritengo molto fortunata ad aver incontrato e conosciuto ognuno di voi!

Voglio ringraziare tutti i miei amici che hanno condiviso questi 3 anni di percorso: i miei housemates (Alberto, sarai sempre il coinqui del mio cuore) e roommate (grazie alla Leo per avermi sempre aiutato, spronato e anche sopportato!); le mie compagne di calcio e i misters (in particolare l'aiuto grafico della Gasp!); tutto il gruppo TIR (grazie Silvia per avermi coinvolto nello staff). Grazie a PBM, Fede L., Ali, Ele, Fede F., Ery e Mary, Paola BP, Claudia... grazie al mio fratellino Fabio! Grazie davvero, non vi elenco tutti, ma voi sapete chi siete e spero sappiate che l'importanza avete avuto e avete per me.

Infine, un grazie speciale alla mia famiglia ed in particolare ai miei genitori. Grazie per tutto quello che avete fatto e per avermi lasciato libera di cercare la mia strada.

Dover pensare, voler pensare. Spinge la mia mente, a volte zoppicante, a voler guarire, rialzarsi e correre ancora più veloce. Perché correre mi fa sentire libera. E capire l'importanza di essere critici. Non è che se una cosa la dicono in tanti allora diventa vera. Ma cercare prove, evidenze, dimostrazioni per riuscire nello scopo principale: convincere la propria testa.

Every single pixel  
of that picture we made together  
It tells something of us  
whispering me moments (snapshot)  
It reveals enclosed memories  
which I will cherish forever.  
Thank you!

Ogni singolo pixel  
di quel quadro composto insieme  
racconta qualcosa di noi  
mi sussurra momenti (istantanee)  
apre ricordi racchiusi  
che custodirò per sempre.  
Grazie!

Federica

# Curriculum Vitae

Federica Rigoni was born on January 16<sup>th</sup> in Chiari (BS), Italy. In 2003, after obtaining the Diploma at “Grazio Cossali” Liceo Scientifico in Orzinuovi (BS), she started her study in Physics at the “Università Cattolica del Sacro Cuore” of Brescia resulting in Bachelor’s degree in 2008 (bachelor thesis title: “Deposizione e proprietà fisiche di strati sottili di eumelanina sintetica.”) and Master’s degree in Physics in 2011 (master thesis title: “Interazione di nanotubi di carbonio con molecole di ammoniaca. Dalla fisica delle superfici ai dispositivi.”), under the supervision of prof. L. Sangaletti. From June to September 2010 she worked as collaborator in the project “RESENT” on nanostructured gas sensors at Università Cattolica. From 2011 onwards she continued her research activity on the topic of the interaction between polluting gas molecules and carbon nanotubes, as PhD student at “Doctorate School in Physics, Astrophysics and Applied Physics” at Università degli Studi di Milano joint with Physics Department of Università Cattolica, under the supervision of prof. L. Sangaletti. Most of the results of this research are described in this thesis, were published in scientific journals and were presented at international conferences.

During this time she also supervised four Master students and one Bachelor student in Physics, she worked as Laboratory Assistant in Physics Education at Università Cattolica (academic years: 2012-13 and 2013-14) and as Laboratory Assistant in the “Progetto Lauree Scientifiche” for high-school students.

Finally, she has got the opportunity for Beam Times at Elettra Synchrotron of Trieste (BACH beam line) and for a 2 weeks internship (September 14-27, 2014) in a “Short Time Scientific Mission” at Institut de Chimie Moléculaire de l’Université de Bourgogne (ICMUB) in Dijon (France), the latter funded by the COST Action TD1105 - EuNetAir.

